Development of Nanostructured ZnO Films as Electron-Transporting Layer for Perovskite Solar Cell Applications

(ペロブスカイト太陽電池の電子輸送層への応用に向けたナノ構造酸化亜鉛薄膜の開発)

Christian Mark Pelicano

July 2019

Graduate School of Materials Science
Nara Institute of Science and Technology

Abstract

The recent rise of perovskite solar cells (PSCs) brought a new era to the photovoltaic industry owing to the exceptional improvement of their efficiencies, surpassing 24% within a decade of comprehensive research. This outcome places them as a frontrunner to replace expensive Si solar cells. Most state-of-the-art PSCs utilize an electron-transporting layer (ETL) to ensure selective extraction of electrons and to suppress charge recombination. Mesoporous TiO_2 is largely used as ETL in high performance PSCs, however, a high-temperature annealing at 500-550 °C is generally required to prepare TiO_2 layers, which drastically limited the application of PSCs in flexible devices. Among metal oxides, ZnO is the most promising due to its high electron mobility, high transparency and abundant nanostructures (NSs). However, existing ZnO growth methods involve toxic chemical reagents, sophisticated process, expensive equipment, and high temperature systems. Thus, the challenge now is to develop a low cost, green and energy efficient technique to produce novel ZnO NSs that is compatible for sustainable commercialization of PSCs. Herein, we employ two low-temperature methods ($T < 100°C$) to produce ZnO NSs. We first explored electrodeposition, which has the capability to obtain high-quality ZnO NSs at a faster rate. Then, we developed a highly novel, facile, low temperature technique called H_2O oxidation, which simply involves the immersion of Zn thin films in pure H_2O. Detailed growth mechanisms for the synthesized NSs are discussed and their application as ETL for PSCs is examined through comprehensive structural, chemical composition, surface chemistry, optical and electronic characterizations.

A brief introduction about the history of PSCs, as well as their device architecture and operating principle, is introduced in the first chapter. The significant role of ETL, especially the advantages of nanostructured ZnO, for efficient charge extraction is discussed.

Then, a short review of ZnO growth techniques is given to establish the importance and goals of this research. Chapter 2 examined the synergistic effect of high-quality electrodeposited ZnO nanorods (NRs) and rubrene interlayer to improve the performance of PSCs. The effects of NR length and the presence of an interlayer were investigated. A solar cell device optimized with ZnO NRs and rubrene:P3HT bilayer showed a PCE_{max} of 4.9% and reduced hysteresis behavior. The formation of nanostructured ZnO films via low-temperature H_2O oxidation is presented in chapter 3. The first subchapter explored the influence of growth time and temperature on ZnO-based PSCs. A PCE_{max} of 6% was achieved with PSCs based on pointed NRs. In the second part, the effect of pH on ZnO-based Pb-free PSCs is investigated. PSCs based on ZnO NPs generated in an acidic H_2O attained a competitive PCE_{max} of 0.083% with good stability.

Chapter 4 described the transformation of H_2O-oxidized ZnO NRs into Al-doped ZnO nanotubes (AZO NTs) via simultaneous etching and Al doping. The AZO NTs showed superior charge transport properties compared with ZnO NRs. Chapter 5 presented the integration of microwave technology with H_2O oxidation to generate novel nanostructured ZnO films at a significantly reduced time duration. High-quality ZnO NRs were successfully fabricated even only after 30 min of microwave-assisted H_2O oxidation. The as-synthesized NSs were also effective ETL for solar cells as seen on the quenching of perovskite emission from their steady-state PL spectra.

In summary, effective low-temperature strategies were presented to form novel ZnO NSs as ETL for PSCs. H_2O-oxidized ZnO is proven to be a better ETL compared with electrodeposited ZnO. The results highlight the potential of H_2O-oxidized ZnO not only for future photovoltaics, but also in other ZnO-based electronic devices. Lastly, there are still lots of unexplored area in this study, thus, this is very interesting to continue and to extend for possible commercialization plans.

Table of Contents

Chapter 1

General Introduction

1.1 Solar Cell Technology

The expected rise in global energy consumption and growing worldwide concern about climate change has shifted research interests on renewable energy sources, among which solar energy is the leading example[1, 2]. Solar energy is broadly considered to be one of the primary alternatives to the fossil fuels, which have caused climate and pollution problems. Through the use of photovoltaics (PVs), solar energy can be utilized by directly converting sunlight to electricity. However, PVs supply just a small (<2%) portion of world energy consumption despite its immense potential and remarkable development[3]. Higher energy costs in comparison with the conventional generation methods prevented the extensive deployment of PV. So far, PV technologies can be divided into three generations. The first generation solar cells include monocrystalline and polycrystalline Si solar cells. About 90% of the PV industry is controlled by Si PVs due to its high performance (about 15-20%) and excellent stability[4]. Conversely, Si PVs have naturally expensive manufacturing and installation costs[5]. The second generation solar cells are thin-film solar cells including cadmium telluride (CdTe), copper indium gallium selenide (CIGS), copper indium diselinide (CIS), amorphous Si solar cells (a:Si) and cadmium sulphide (CdS). These devices have reduced semiconducting layer thickness, hence, lower production costs. However, a slight decline in efficiency (10-15%) is also expected due to the limited crystalline quality of these thin films. In addition, their production requires the utilization of rare earth materials[6]. Lastly, novel PV technologies that are recognized as the third generation solar cells include solution-processed dye sensitized solar cells (DSSCs), organic solar cells (OSCs), quantum dot sensitized solar cells (QDSCs), and perovskite solar cells (PSCs) [7].

1.2 Perovskite Solar Cells

The development of thin-film solar cells utilizing an organic-inorganic perovskite compound as light absorber has recently generated enormous attention in the PV research field due to their remarkable efficiencies[8-12]. As shown in Figure 1.1, organic-inorganic perovskite has a 3D cubic structure with a general formula of ABX_3, where A is a cation $(CH_3NH_3{}^+, NH = CHNH_3{}^+, Cs^+)$[13-15], B is an inorganic divalent or trivalent cation $(Pb^{2+}, Sn^{2+}, Bi^{3+}, Sb^{3+})$[15-18] and X are negatively charged halides (I^-, Br^-, Cl^-)[19-22].

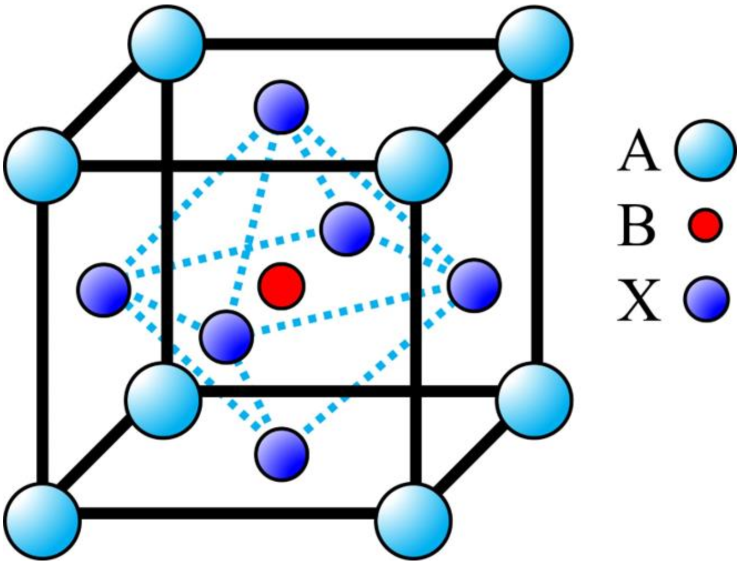

Figure 1.1 Cubic crystal structure of organic-inorganic halide perovskite.

The rapid efficiency enhancement can be associated to the superb photovoltaic properties of lead halide perovskite, such as strong absorption in a broad range of the visible spectrum[23, 24], small excitonic binding energy of around ~ 2 meV[25, 26], long charge diffusion length of 100-1000 nm[27, 28], high charge-carrier mobilities[29, 30], and tunable band gap over the range of 1.1-2.3 eV[31, 32]. This PV technology integrates individual advantages of previously established solar cells: high efficiency (crystalline Si), lightweight and flexible (GaAs and CIGS inorganic thin-film PVs), and scalable low-temperature solution processability and color tunability (DSSCs, QDSCs and OSCs) [33]. Figure 1.2 presents the brief evolution of PSC efficiency over the span of almost a decade. The first perovskite-sensitized solar cells were reported by Kojima et al. in 2009, wherein $CH_3NH_3PbI_3$ and $CH_3NH_3PbBr_3$ were used as sensitizers achieving a *PCE* of 3.81% and 3.13%, respectively[34].

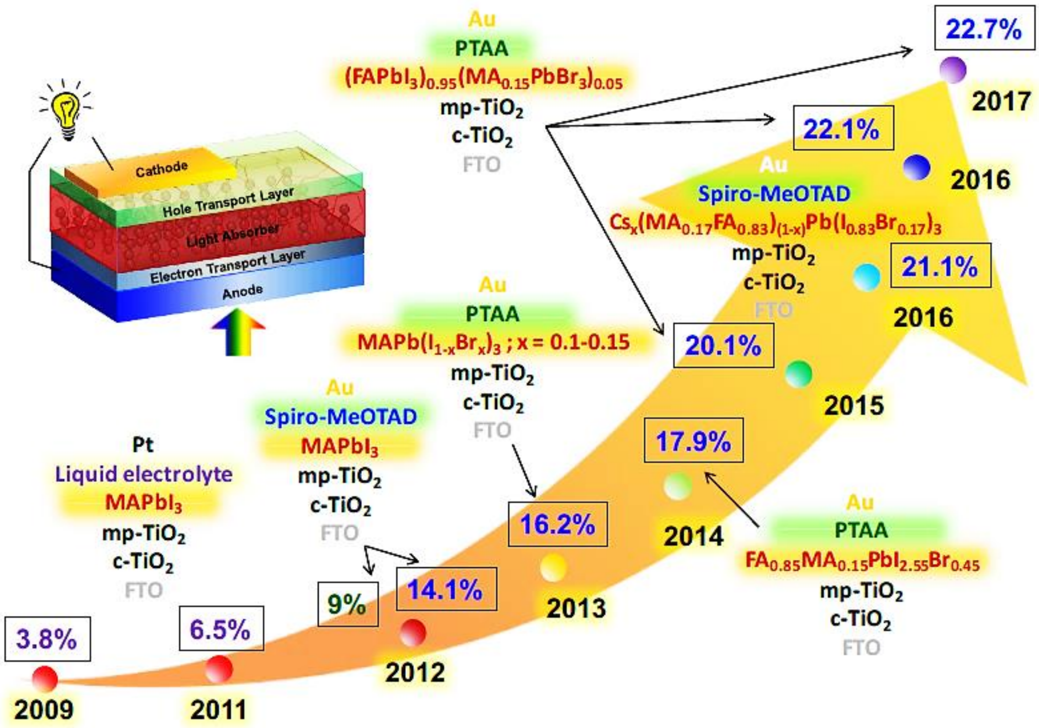

Figure 1.2 PSC efficiency evolutions over the years. The certified efficiencies by NREL are represented by blue-colored numbers. Reproduced with permission[35]. Copyright 2018, IOP Publishing Ltd.

In 2011, Park et al. reported an improved *PCE* of 6.5% from a $CH_3NH_3PbI_3$ quantum dot (QD)-sensitized solar cell. However, their solar cell displayed poor stability (about 10 min) under continued irradiation due to the reaction of the perovskite with the redox electrolyte[36]. A solid-state DSSC with superior stability was finally fabricated in mid-2012 with a *PCE* of 9.7% with Spiro-OMeTAD as a solid hole-transporting layer (HTL) and $CH_3NH_3PbI_3$ as the absorber[37]. Afterwards, comprehensive research efforts on materials optimization, innovative device architectural design, morphological engineering, interfacial engineering, and improved fabrication conditions have pushed the efficiency of PSCs at an incredible rate[38-40]. These great advancements played a major role in promoting widespread research interests in PV community which resulted in an impressive rise in the number of publications in the last few years. To date, the certified efficiency of PSCs has skyrocketed to 24.2% rivalling those of commercial solar cells based on monocrystalline Si films[41].

1.2.1 Working Principle and Device Architecture

Light absorption, charge generation, charge transport, and charge collection are general solar cell operating processes which also take place in PSCs, as shown in Figure 1.3[42]. A number of researches on the charge transport dynamics in PSC proposed that after photon absorption, an electron-hole pair is instantaneously created in perovskite absorber. Then, this electron-hole pair will dissociate into free-charge carriers in less than 2 ps by the built-in electric field triggered by the difference in the work function between the cathode and the anode[11, 30, 43]. Several groups also confirmed this phenomenon by reporting a small excitonic binding energy (< 0.05 eV) for perovskite absorber demonstrating that basically the photon absorption leads to free-carrier generation[44-46]. In excitonic solar cells, substantial losses in energy happens via exciton migration and dissociation[47], hence, this one-step and efficient generation of free charge carriers is a huge advantage for PSCs.

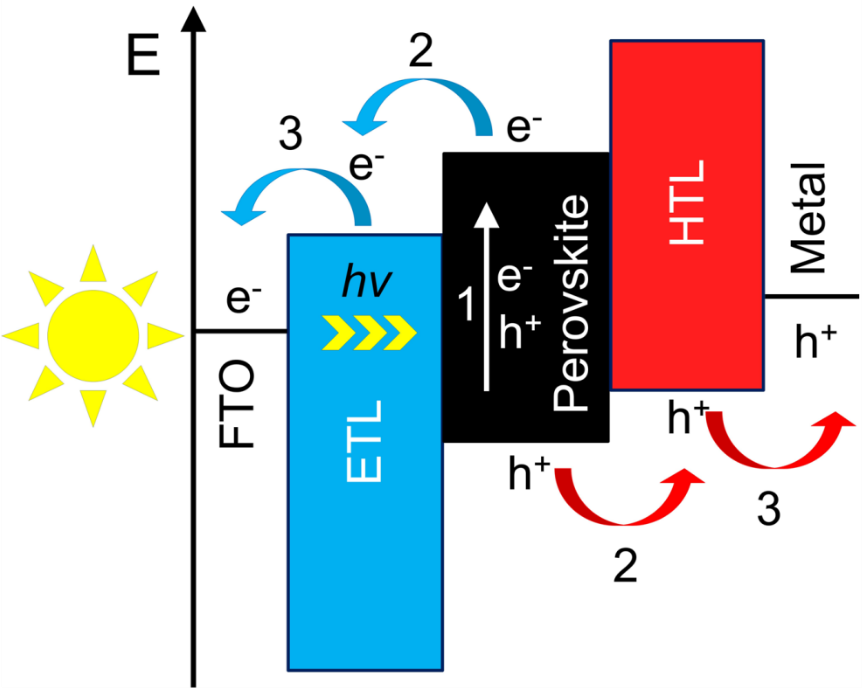

Figure 1.3 Band diagram and main processes in PSC: (1) Absorption of photon and free charge carrier generation; (2) Charge transport; and (3) Charge extraction.

Figure 1.4 presents the two well-known device configurations for PSCs which are mesoporous- and planar-PSC structures. The charge transport channels in PSC are commonly examined based on these two device architectures. In mesoporous structure, several voids within the ETL layer are present allowing the infiltration of perovskite layer (Figure 1.4(a)). Herein, the central roles of mesoporous ETL are to receive the photoexcited electrons from the perovskite and transport them to the FTO substrate. It also performs as a frame to support the growth of perovskite layer[48]. The main advantage of this type of device configuration is it can offer a better electronic contact between the ETL and active layer enabling faster charge transfer[49]. Additionally, mesoporous or nanostructured layers are known to improve the stability of the overall device compared to planar heterojunction-based devices[50].

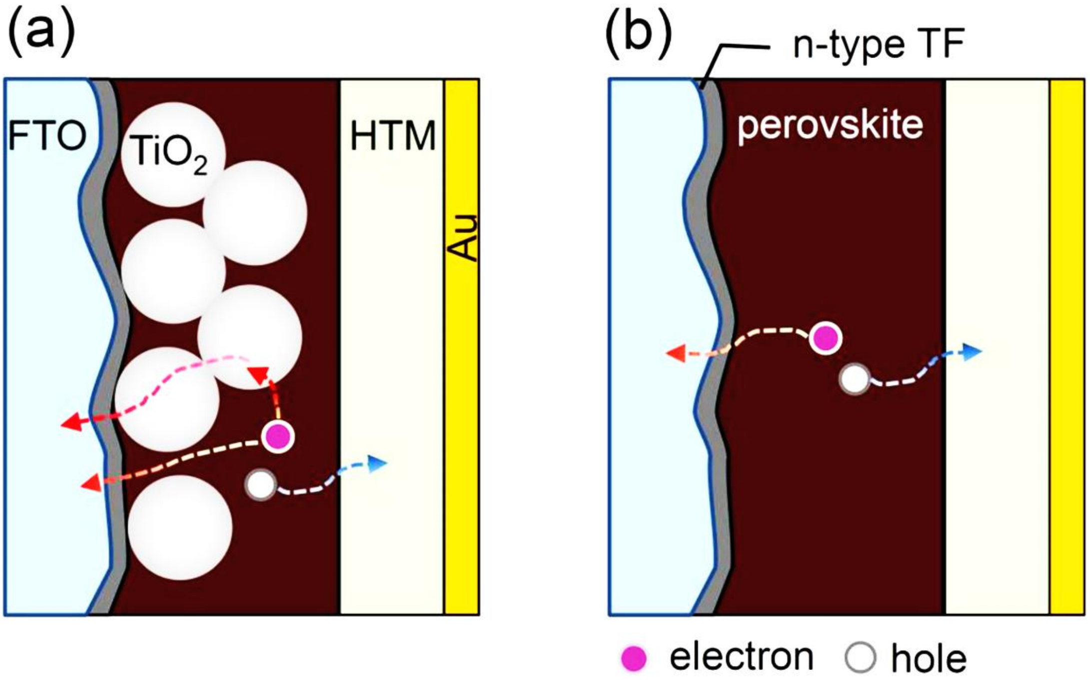

Figure 1.4 (a) Mesoscopic PSC with mesoporous TiO_2 layer and (b) planar structure without a mesoporous TiO_2 layer. Thin film (TF) on fluorine-doped tin oxide (FTO) substrate is an n-type semiconductor. Reproduced with permission[42]. Copyright 2014, Wiley-VCH.

On the other hand, a compact ETL is usually employed in the case of planar heterojunction PSC, as illustrated in Figure 1.4(b). The main functions of the compact ETL are to ensure the delivery of photoexcited electron from the absorber layer to the external circuit and operate as a hole-blocking layer (HBL) to impede the diffusion of photogenerated holes from the perovskite to the FTO side[51]. Simultaneously, the compact ETL should prevent the reverse transport of electrons from the FTO to the absorber[52]. Hence, it is very important for the ETL to be uniform, continuous and ultrathin. These properties also guarantee that the FTO substrate will not have a direct contact with the perovskite or HTL to avoid severe charge recombination and lower device performance[53, 54].

1.3 Nanostructured ZnO Films as Electron-Transporting Layer for Perovskite Solar Cells

For highly efficient PSCs, ETL materials should have the following ideal characteristics: (1) high electron mobility; (2) excellent optical transmittance in the visible range, which lessens the optical loss; (3) their energy levels should complement that of perovskite, which could increase the electron-transport efficiency; and (4) high quality ETL should be easily fabricated[55, 56]. Accordingly, proper design of ETL is crucial for solar cell operation. Most state-of-the-art PSCs utilize the compact or mesoporous TiO_2 as ETL[57, 58]. The conduction band level of TiO_2 is highly compatible with that of perovskite in such a way that fast electron injection from the active layer is possible. However, its low electron mobility (0.1−4 $cm^2\ V\ s^{-1}$) leads to high electron recombination and unbalanced charge transport[59, 60]. High temperature sintering ($T > 400$ °C) is also normally required to attain the conducting phase of TiO_2[61]. These reasons hinder the application of TiO_2 in flexible photovoltaic devices through roll-to-roll processing. Hence, replacement materials for TiO_2 need to be explored in order to realize stable, efficient and flexible solar cell devices.

A promising alternative is ZnO, which is another n-type semiconductor that has equally excellent optoelectronic features, as shown in Table 1.1. It has a wide band gap of 3.37 eV and high electron mobility ranging from 200−300 $cm^2\ V\ s^{-1}$ for bulk material and about 1000 $cm^2\ V\ s^{-1}$ for single crystalline nanowires, which are several orders of magnitude higher than that of TiO_2[62, 63]. It also has a spontaneous piezoelectric polarization due to the stacking of alternating and planes along the *c*-axis of its hexagonal wurtzite structure (Figure 1.5)[64]. ZnO has very high transmittance in the visible region and has almost identical energy band position and physical properties to TiO_2. High temperature annealing is also not a requirement for fabricating high-quality nanostructured ZnO resulting in lower production cost and possible application in flexible devices. These properties make ZnO a viable ETL for PSCs. Hence, researches on ZnO-based ETL would further help in developing high performance PSCs.

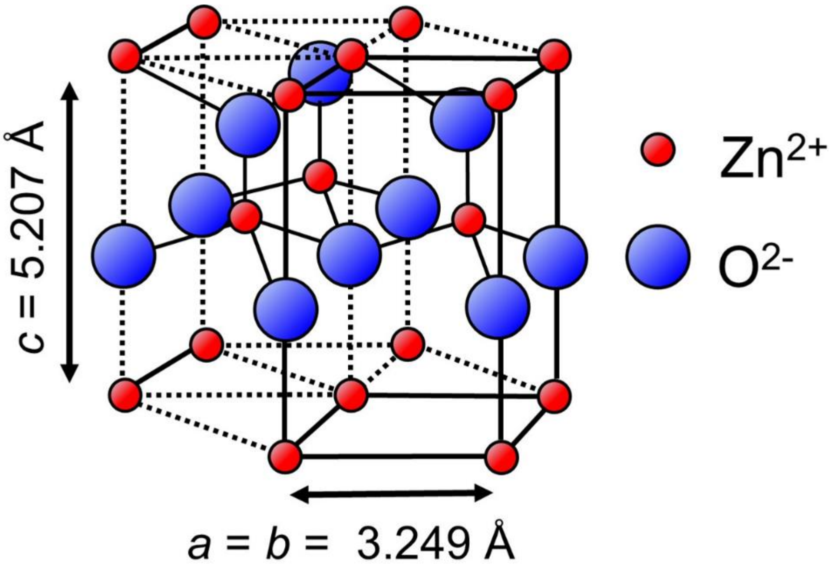

Figure 1.5 Hexagonal wurtzite crystal structure of ZnO.

Table 1.1 Comparison of the structural and physical properties of ZnO and TiO_2[64].

	ZnO	TiO_2
Crystal Structure	Wurtzite (hexagonal)	Anatase (tetragonal)
Space Group	P63mc	141/amd
Band Gap Energy (eV)	3.4	3.2-3.3
Electron Mobility ($cm^2\ V\ s^{-1}$)	Bulk: 205-300 Single NW: 1000	0.1-4
Refractive Index	2.0	2.5
Electron Effective Mass (m_e)	0.26	9
Relative Dielectic Constant	8.5	170
Electron Diffusion Coefficient ($cm^2\ s^{-1}$)	Bulk: 5.2 Nanoparticle Film: 1.7 x 10^{-4}	Bulk: 0.5 Nanoparticle Film: 10^{-8} – 10^{-4}

1.3.1 Fabrication Techniques for Nanostructured ZnO Films

High-quality ZnO films can be fabricated by different growth techniques to form various surface nanostructures (NSs) including, but not limited to rods, tubes, belts, wires, rings, and tetrapods[65-67]. These NSs have higher surface area than normal thin films which is advantageous as ETL. The intrinsic properties of these nanostructured ZnO can be further modified by controlling their orientation, dopant content, and structural composition[68-70]. Therefore, a wide range of physical and chemical methodologies have been adopted to synthesize ZnO NSs such as RF magnetron sputtering, atomic layer deposition (ALD), chemical vapor deposition (CVD), electrochemical deposition (ECD), hydrothermal method, sol-gel process, chemical bath deposition (CBD) and electrospraying method[71-80]. Table 1.2 summarizes the performance and structure of some nanostructured ZnO-based PSCs.

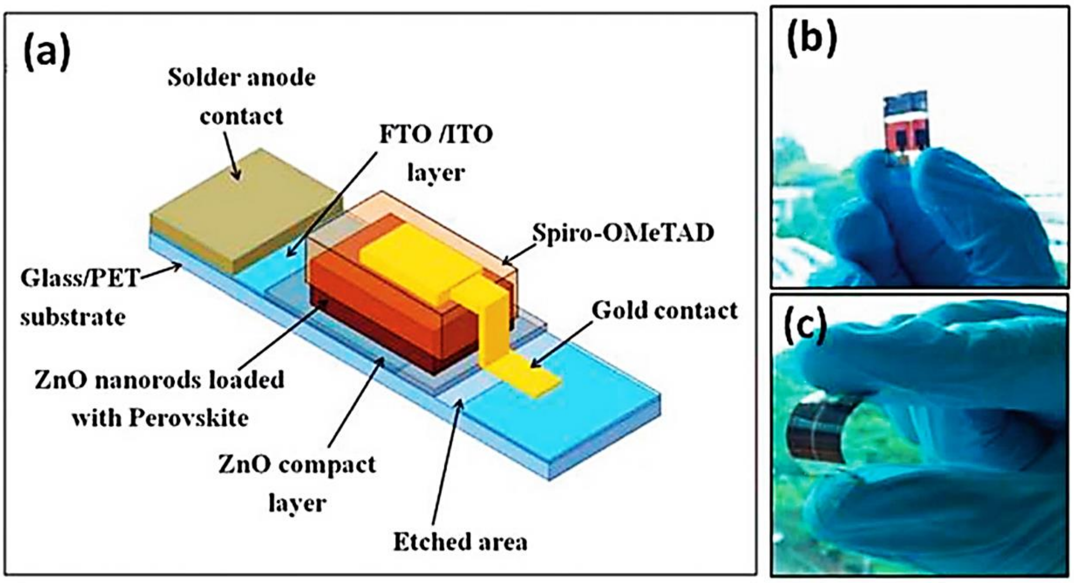

Figure 1.6 (a) Schematic illustration of the architecture for the perovskite devices, (b) device on the FTO substrate, and (c) device on the flexible PET/ITO substrate. Reproduced with permission[75]. Copyright 2013, The Royal Society of Chemistry.

Table 1.2 Photovoltaic parameters of different nanostructured ZnO-based PSCs

Morphology of ZnO	Method	Structure	*PCE* [%]	*Ref.*
Compact layer	RF sputtering	AZO/$MAPbI_3$/spiro-OMeTAD/Au	12.6	(71)
Nanoparticles (NPs)	ALD	ITO/ZnO/$MAPbI_3$/spiro-OMeTAD/Ag	7.0	(72)
Nanocolumns	CVD	FTO/ZnO/$MAPbI_3$/spiro-OMeTAD/Au	4.8	(73)
Nanorods (NRs)	ECD	FTO/ZnO/$MAPbI_3$/spiro-OMeTAD/Au	10.3	(74)
NPs + NRs	ECD + CBD	FTO/ZnO/$MAPbI_3$/spiro-OMeTAD/Au	8.9	(75)
Nanowalls	CBD	ITO/ZnO/$MAPbI_3$/spiro-OMeTAD/Ag	13.6	(76)
NPs	Sol-gel	FTO/ZnO/$MAPbI_3$/spiro-OMeTAD/Au	5.4	(77)
NRs	Hydrothermal	FTO/ZnO/PEI/$MAPbI_3$/spiro-OMeTAD/Au	13.4	(78)
NRs	Hydrothermal	FTO/N-ZnO/PEI/$MAPbI_3$/spiro-OMeTAD/Au	16.1	(78)
Quantum Dots (QDs)	Hydrothermal	FTO/ZnO/$MAPbI_3$/spiro-OMeTAD/Au	7.5	(79)
QDs	Hydrothermal	FTO/ZnO/Graphene/$MAPbI_3$/spiro-OMeTAD/Au	15.2	(79)
NPs	Electrospraying	FTO/ZnO/$MAPbI_3$/spiro-OMeTAD/Ag	10.8	(80
NPs	Electrospraying	FTO/Al-ZnO/$MAPbI_3$/spiro-OMeTAD/Ag	12	(80)

The earliest reported solid-state PSC, which is based on ZnO NRs grown by CBD, showed a *PCE* below 3% on PET/ITO substrate and up to 9% on FTO/glass substrate (Figure 1.6)[75]. Nanostructured ZnO grown by ECD was also used for PSCs with a *PCE* of 10.28%[74]. Mahmood et al. have obtained an efficient PSC based on hydrothermally grown high aspect ratio N-doped ZnO NRs with a *PCE* of 16.1%[78]. Based on Table 1.2, the fabrication methods and the resulting ZnO morphologies are not the only major factors for achieving highly-efficient PSCs. Clearly, doping and interfacial modification of ZnO can also effectively boost the device performance. Nevertheless, some issues are yet to be addressed, thus, further optimization and improvement of ZnO-based PSCs have to be carried on.

1.4 Objectives and Research Outline

Developing a reliable and sustainable protocol to form NSs is of significant interest due to the emergence of ZnO-based applications such as solar cells. However, the majority of the conventional ZnO growth techniques listed above suffer from some drawbacks, such as the requirement of high temperature, surfactants, expensive and sophisticated equipment, and large volume of harmful chemicals. In addition, contaminations in the final products are likely to occur when templates and catalysts are utilized in the reaction system. Likewise, these traditional protocols involve multi-step preparation methods to achieve high yields delaying the commercialization of multidimensional ZnO nanomaterials. Thus, the main objective of this study is to develop a simple, low temperature, surfactant-free and environmental-friendly route for fabricating nanostructured ZnO films that is compatible for sustainable large-scale production of PSCs.

This research proposes two low temperature growth techniques for developing nanostructured ZnO films that can be used for PSCs. The first method is electrochemical deposition using chloride medium. This process allows fast deposition rate at low temperatures in large surface areas. But it still uses a complex set-up so we developed a highly novel, facile, low temperature technique called H_2O oxidation. This process involves the immersion of Zn films in pure H_2O to produce diverse ZnO NSs. Then, the ZnO NSs obtained from the two methods will be applied as ETL for PSCs.

The general outline of this research is as follows:

Chapter 1 provides a brief introduction about the rapid development, device architecture and working principle of PSCs. The essential role of ETL in PSCs and the need for substitute ETL materials, such as nanostructured ZnO, are examined. Then a short review of existing ZnO growth methods is presented to set-up the significance of this research.

Chapter 2 discusses the growth of ZnO NRs by electrochemical deposition using a chloride medium. Additionally, the effect of rubrene as an interlayer between the perovskite and P3HT is explored.

Chapter 3 introduces the novel low temperature H_2O oxidation technique for fabricating nanostructured ZnO films. First, the influence of growth time and temperature on the performance of ZnO-based PSCs is investigated. Then, the effect of solution pH on H_2O-oxidized ZnO and its application as ETL for Bi-based Pb-free PSCs is evaluated.

Chapter 4 aims to further improve the charge-transport properties of H_2O-oxidzed ZnO, hence, an innovative approach of simultaneous etching and Al doping of ZnO NRs is developed. The resulting Al-doped ZnO nanotubes (AZO NTs) are systematically characterized to establish its potential as ETL for PSCs.

Chapter 5 establishes the integration of microwave technology with H_2O oxidation to speed up the growth of nanostructured ZnO films. Likewise, comprehensive characterizations of the resulting nanostructured films are done to uncover their underlying properties as ETL for PSCs.

Chapter 6 gives an overall summary of the research and provides recommendations for future studies.

References

(1) R. Rachchh, M. Kumar and B. Tripathi, *Energy Convers. Manag.*, 2016, **115**, 244–252.

(2) J. Khan and M. H. Arsalan, *Renew. Sustain. Energy Rev.*, 2016, **55**, 414–425.

(3) M. Anaya, G. Lozano, M. E. Calvo and H. Míguez, *Joule*, 2017, **1**, 769.

(4) A. Jäger-Waldau, *Eur Union*, 2012, **28**, 26-27.

(5) J. Jean, P. R. Brown, R. L. Jaffe, T. Buonassisi and V. Bulovic´, *Energy Environ. Sci.*, 2015, **8**, 1200.

(6) L. El Chaar and N. El Zein, *Renew. Sustain. Energy Rev.*, 2011, **15**, 2165-2175.

(7) M. F. M. Noh, C. H. Teh, R. Daik, E. L. Lim, C. Y. Chi, M. A. Ibrahim, N. A. Ludin, A. R. B. M. Yusoff, J. Jin and M. A. M. Teridi, *J. Mater. Chem. C*, 2018, **6**, 682-712.

(8) B. J. Kim , D. H. Kim, Y.-Y. Lee , H.-W. Shin, G. S. Han, J. S. Hong, K. Mahmood, T. K. Ahn, Y.-C. Joo, K. S. Hong, N.-G. Park, S. Lee and H. S. Jung, *Energy Environ. Sci.*, 2015, **8**, 916-921.

(9) J. H. Noh, S. H. Im, J. H. Heo, T. N. Mandal and S. I. Seok, *Nano Letters*, 2013, **13**, 1764-1769.

(10) M. Liu, M. B. Johnston and H. J. Snaith, *Nature*, 2013, **501**, 395-398.

(11) N. G. Park, *J. Phys. Chem. Lett.*, 2013, **4**, 2423-2429.

(12) J. Burschka, N. Pellet, S. J. Moon, R. Humphry-Baker, P. Gao, M. K. Nazeeruddin and M. Gratzel, *Nature*, 2013, **499**, 316-319.

(13) X. Chen, S. Yang, Y. C. Zheng, Y. Chen, Y. Hou, X. H. Yan and H. G. Yang, *Advanced Science*, 2015, **2**, 1500105.

(14) C. Mu, J. Pan, S. Feng, Q. Li and D. Xu, *Adv. Energy Mater.*, 2017, **7**, 1601297.

(15) C.-Y. Chen, H. Y. Lin, K.-M. Chiang, W. L. Tsai, Y.-C. Huang, C. S. Tsao and H. W. Lin, *Adv. Mater.*, 2017, **29**, 1605290.

(16) G. Gou, J. Young, X. Liu and J. Rondinelli, *Inorg. Chem.*, 2017, **56**, 26-32.

(17) M. Pazoki, M. Johansson, H. Zhu, P. Broqvist, T. Edvinsson, G. Boschloo and E. Johansson, *J. Phys. Chem. C*, 2016, **120**, 29039-29046.

(18) J. C. Hebig, I. Kühn, J. Flohre and T. Kirchartz, *ACS Energy Lett.*, 2016, **1**, 309-314.

(19) W-T. Wang, S. Das and Y. Tai, *ACS Appl. Mater. Interfaces*, 2017, **9**, 10743-10751.

(20) N. Arora, M. I. Dar, M. Abdi-Jalebi, F. Giordano, N. Pellet, G. Jacopin, R. Friend, G. M. Zakeeruddin and M. Grätzel, *Nano Letters*, 2016, **15**, 7155-7160.

(21) N. D. Pham, V. T. Tiong, P. Chen, L. Wang, G. Wilson, J. Bella and H. Wang, *J. Mater. Chem. A*, 2017, **5**, 5195-5203.

(22) M. A. Green, A. Ho‐Baillie and H. J. Snaith, *Nat. Photon.*, 2014, **8**, 506.

(23) S. A. Bretscheider, J. Weickert, J. A. Dorman and L. Schmidt-Mende, *APL Materials*, 2014, **2**, 040701.

(24) T. Baikie, Y. Fang, J. M. Kadro, M. Schreyer, F. Wei, S. G. Mhaisalkar, M. Gratzel, T. J. White, *J. Mater. Chem. A*, 2013, **1**, 5628-5641.

(25) Y. Yamada, T. Nakamura, M. Endo, A. Wakamiya and Y. Kanemitsu, *IEEE J. Photovolt.*, 2015, **5**, 401-405.

(26) Q. Lin, A. Armin, R. C. R. Nagiri, P. L. Burn and P. Meredith, *Nature Photonics*, 2014, **9**, 106-112.

(27) G. Xing, N. Mathews, S. Sun, S. S. Lim, Y. M. Lam, M. Grätzel, S. Mhaisalkar and T. C. Sum, *Science*, 2013, **342**, 344-347.

(28) S. D. Stranks, G. E. Eperon, G. Grancini, C. Menelaou, M. J. P. Alcocer, T. Leijtens, L. M. Herz, A. Petrozza and H. J. Snaith, *Science*, 2013, **347**, 519-522.

(29) D. B. Mitzi, C. A. Feild, Z. Schesinger and R. B. Laibowitz, *J. Solid State Chem.*, 1995, **114**, 159-163.

(30) C. S. Ponseca Jr., T. J. Savenjie, M. Abdellah, K. Zheng, A. Yartsev, T. Pascher, T. Harlang, P. Chabera, T. Pullerits and A. Stepanov, *J. Am. Chem. Soc.*, 2014, **136**, 5189-5192.

(31) M. Saliba, T. Matsui, J.-Y. Seo, K. Domanski, J.-P. Correa-Baena, M. K. Nazeeruddin, S. M. Zakeeruddin, W. Tress, A. Abate, A. Hagfeldt and M. Gratzel, *Energy Environ. Sci.*, 2016, **9**, 1989-1997.

(32) C. C. Stoumpos, C. D. Malliakas and M. G. Kanatzidis, *Inorg. Chem.*, 2013, **52**, 9019-9038.

(33) A. Rajagopal, K. Yao and A. K. Y. Jen, *Adv. Mater.*, 2018, **30**, 1800455.

(34) A. Kojima, K. Teshima, Y. Shirai and T. Miyasaka, *J. Am. Chem. Soc.*, 2009, **131**, 6050–6051.

(35) L. K. Ono and Y. Qi, *J. Phys. D: Appl. Phys.*, 2018, **51**, 093001.

(36) J. H. Im, C. R. Lee, J. W. Lee, S. W. Park and N. G. Park, *Nanoscale*, 2011, **3**, 4088.

(37) H. S. Kim, C. R. Lee, J. H. Im, K. B. Lee, T. Moehl, A. Marchioro, S. J. Moon, R. Humphry - Baker, J. H. Yum, J. E. Moser, M. Gratzel and N. G. Park, *Sci. Rep.*, 2012, **2**, 591.

(38) N. J. Jeon, J. H. Noh, Y. C. Kim, W. S. Yang, S. Ryu and S. I. Seok, *Nat. Mater.*, 2014, **13**, 897-903.

(39) H. Zhou, Q. Chen, G. Li, G. Luo, T.-b. Song, H.-S. Duan, Z. Hong, J. You, Y. Liu and Y. Yang, *Science*, 2013, **345**, 542-546.

(40) N. J. Jeon, J. H. Noh, W. S. Yang, Y. C. Kim, S. Ryu, J. Seo and S. I. Seok, *Nature*, 2015, **517**, 476–480.

(41) NREL Best Research-Cell Photovoltaic Efficiency Chart.

(42) H.S. Jung and N.G. Park, *Small*, 2015, **11**, 10-25.

(43) H. J. Snaith, A. Abate, J. M. Ball, G. E. Eperon, T. Leijtens, N. K. Noel, S. D. Stranks, J. T.-W. Wang, K. Wojciechowski and W. Zhang, *J. Phys. Chem. Lett.*, 2014, **5**, 1511-1515.

(44) C. Wehrenfennig, G.E. Eperon, M.B. Johnston, H.J. Snaith and L.M. Herz, *Adv. Mater.*, 2014, **26**, 1584-1589.

(45) A. Miyata, A. Mitioglu, P. Plochocka, O. Portugall, J.T.-W. Wang, S.D. Stranks, H.J. Snaith and R.J. Nicholas, *Nat. Phys.*, 2015, **11**, 582-587.

(46) E. Edri, S. Kirmayer, S. Mukhopadhyay, K. Gartsman, G. Hodes and D. Cahen, *Nat. Commun.*, 2014, **5**, 3461.

(47) S. Collavini, S.F. Völker and J.L. Delgado, *Angew. Chem.*, 2015, **54**, 9757-9759.

(48) Y. Li, J. Zhu, Y. Huang, F. Liu, M. Lv, S. H. Chen, L. H. Hu, J. W. Tang, J. X. Yao and S. Y. Dai, *RSC Adv.*, 2015, **5**, 28424–28429.

(49) G. J. Meyer, *ACS Nano*, 2010, **4**, 4337–4343.

(50) A. Fakharuddin, F. Di Giacomo, I. Ahmed, Q. Wali, T. M. Brown and R. Jose, *J. Power Sources*, 2015, **283**, 61–67.

(51) R. Wu, B. Yang, J. Xiong, C. Cao, Y. Huang, F. Wu, J. Sun, C. Zhou, H. Huang and J. Yang, *J. Renew. Sustain. Energy*, 2015, **7**, 43105.

(52) X. Yin, Y. Guo, Z. Xue, P. Xu, M. He and B. Liu, *Nano Res.*, 2015, **8**, 1997–2003.

(53) H. Lu, Y. Ma, B. Gu, W. Tian and L. Li, *J. Mater. Chem. A*, 2015, **3**, 16445–16452.

(54) N. G. Park, *Mater. Today*, 2015, **18**, 65–72.

(55) M. Gratzel, *Nat. Mater.*, 2014, **13**, 838.

(56) G. Li, R. Zhu and Y. Yang, *Nat. Photonics*, 2012, **6**, 153.

(57) C. Lianga, Z. Wu, P. Li, J. Fan, Y. Zhanga and G. Shao, *Appl. Surf. Sci.*, 2017, **391**, 337-345.

(58) A. Huang, J. Zhu, J. Zheng, Y. Yu, Y. Liu, S. Yang, S. Bao, L. Lei and P. Jin, Nanotechnology, 2017, **28**, 055403.

(59) B.-S. Jeong, D. P. Norton, and J. D. Budai, *Solid State Electron.*, 2003, **47**, 2275-2278.

(60) J. H. Heo, D. H. Song, H. J. Han, S. Y. Kim, J. H. Kim, D. Kim, H. W. Shin, T. K. Ahn, C. Wolf, T.-W. Lee and S. H. Im, *Adv. Mater.*, 2015, **27**, 3424-3430.

(61) T. Leijtens, G. E. Eperon, S. Pathak, A. Abate, M. M. Lee and H. J. Snaith, *Nat. Commun.*, 2013, **4**, 2885.

(62) H. S. Bae, M. H. Yoon, J. H. Kim and S. Im, *Appl. Phys. Lett.*, 2003, **83**, 5313-5315.

(63) A. K. Chandiran, M. Abdi-Jalebi, M. K. Nazeeruddin and M. Gratzel, *ACS Nano*, 2014, **8**, 2261-2268.

(64) P. Zhang, J. Wu, T. Zhang, Y. Wang, D. Liu, H. Chen, L. Ji, C. Liu, W. Ahmad, Z. D. Chen and S. Li, *Adv. Mater.*, 2018, **30**, 1703737.

(65) C. Ottone, V. F. Rivera, M. Fontana, K. Bejtka, B. Onida and V. Cauda, *J. Mater. Res. Technol*, 2014, **30**, 1167-1173.

(66) Y. Li, G. W. Meng, L. D. Zhang and F. Phillipp, *Appl. Phys. Lett.*, 2000, **76**, 2011-2013.

(67) C. Ottone, K. Bejtka, A. Chiodoni, V. Farias, I. Roppolo, G. Canavese, S. Stassi and V. Cauda, *New J. Chem.*, 2014, **38**, 2058-2065.

(68) Z. Zhao, N. Wang, H. Nan, L. Shen, C. Durkan and X. He, *J. Mater. Chem. C*, 2016, **4**, 5814-5821.

(69) Z. Kayani, R. Ishaque, B. Zulfiqar, S. Riaz and S. Naseem, *Opt. Quant. Electron.*, 2017, **49**, 223.

(70) TH. Chen and BL. Jian, *Opt. Quant. Electron.*, 2016, **48**, 77.

(71) X. Zhao, H. Shen, Y. Zhang, X. Li, X. Zhao, M. Tai, J. Li, J. Li, X. Li and H. Lin, *ACS Appl. Mater. Interfaces*, 2016, **8**, 7826.

(72) K.M. Lee, S.H. Chang, K.H. Wang, C.M. Chang, H.M. Cheng, C.C. Kei, Z.L. Tseng and C.G. Wu, *Sol. Energy*, 2015, **120**, 117-122.

(73) F.J. Ramos, M.C. López-Santos, E. Guillén, M.K. Nazeeruddin, M. Grätzel, A.R. Gonzalez-Elipe and S. Ahmad, *ChemPhysChem*, 2014, **15**, 1148-1153.

(74) J. Zhang, P. Barboux and T. Pauport, *Adv. Energy Mater.*, 2014, **4**, 1400932.

(75) M.H. Kumar, N. Yantara, S. Dharani, M. Gräetzel, S. Mhaisalkar, P.P. Boix and N. Mathews, *Chem. Commun.*, 2013, **49**, 11089-11091.

(76) J.F. Tang, Z.L. Tseng, L.C. Chen and S.Y. Chu, *Sol. Energy Mater. Sol. Cells*, 2016, **154**, 18-22.

(77) Y. Cheng, Q. D. Yang, J. Xiao, Q. Xue, H. W. Li, Z. Guan, H. L. Yip and S. W. Tsang, *ACS Appl. Mater. Interfaces*, 2015, **7**, 19986.

(78) K. Mahmood, B. S. Swain and A. Amassian, *Adv. Energy Mater.*, 2015, **5**, 1500568.

(79) M. M. Tavakoli, R. Tavakoli, Z. Nourbakhsh, A. Waleed, U. S. Virk, Z. Fan, *Adv. Mater. Interfaces*, 2016, **3**, 1500790.

(80) K. Mahmood, B. S. Swain, H. S. Jung, *Nanoscale*, 2014, **6**, 9127.

Chapter 2

Electrochemical Deposition of ZnO Nanorods for Perovskite Solar Cells with Rubrene:P3HT as Hole-Transporting Layer

2.1 Introduction

ZnO nanostructures (NSs) exhibit a remarkable set of physical and chemical properties which makes them attractive in various applications such as light emitting diodes (LEDs) and solar cells[1, 2]. Most importantly, their properties primarily depend on their orientation, morphology, size, and structure density[3, 4]. Thus, designing ZnO NSs with controlled dimensions is crucial to modify their properties and enhance photovoltaic device performance. Among the low temperature routes existing, electrochemical deposition technique offers a lot of advantages including fast and large scale deposition. Likewise, deposition on substrates with different shapes and dimensions is feasible. The morphology and size of NSs can also be manipulated through variation of deposition parameters. Finally, excellent electronic contact between the substrate and NSs can be achieved[5]. A number of studies have demonstrated different electrochemical deposition routes to assemble well-ordered nanostructured ZnO. Lin et al. synthesized vertically aligned ZnO nanorods (NRs) using galvanostatic process. They found out that higher precursor concentration and longer deposition time led to larger ZnO NRs[6]. Another group reported the employment of potentiostatic deposition of nanostructured ZnO with controllable morphology[7]. The surface coverage ratios and the diameters of nanostructured ZnO have increased in higher $Zn(NO_3)_2$ concentration precursor. Zhang et al. described the fast electrochemical growth of fully-covering ZnO layers using $Zn(NO_3)_2$ as precursor and the first group to utilize these electrodeposited film as electron-transporting layer (ETL) for perovskite solar cells (PSCs)[8]. They confirmed that the deposited ZnO layers have high optical and structural quality. After device fabrication, they discovered that the optimized ETL deposition time is only 2 min.

On the other hand, several materials have been designed as candidates for hole-transporting layer (HTL) in PSCs such as NiO, CuSCN[9, 10], polymers (P3HT, PEDOT:PSS)[11, 12], and small molecules (Spiro-MeOTAD, TPB)[13, 14]. Most efficient PSCs are based on Spiro-MeOTAD owing to its matched energy level alignment with perovskite interface, minimizing the energy loss from charge carrier recombination[15, 16]. However, the complex and costly production of Spiro-MeOTAD, as well as, its instability in the presence of additives have driven researchers to explore more stable, cheaper but viable hole-transporting materials[17].

Herein, high-quality ZnO NRs were grown by electrochemical deposition in a chloride medium. Moreover, we introduced rubrene in a regular type PSC as an interlayer between $CH_3NH_3PbI_3$ and P3HT films. Rubrene is a classical p-type organic semiconductor with high hole mobility (10-40 $cm^2\ V^{-1}\ s^{-1}$) and chemical stability. The origin of high carrier mobility in rubrene crystals is due to molecular vibrations mediated carrier transport[18]. Moreover, Krellner et al. measured the density of states in a single rubrene crystal. A density of deep trap states of around $\sim 10^{15}\ cm^{-3}$ was measured in the purest crystals, and exponentially varying shallow trap density near the band edge were identified[19]. These properties significantly affect the electrical performance of rubrene in practical devices.

It also has a moderately low electron affinity and an ionization energy (IE) of about 5.3 eV, which is smaller than that of $CH_3NH_3PbI_3$ (5.7–6.4 eV) [20, 21]. These suggest that rubrene could be appropriate as HTL for PSCs. In this study, we adopted the rubrene interlayer for the first time in a PSC based on electrodeposited ZnO NRs. By optimizing experimental parameters, we achieved a respectable PCE_{max} of 4.87% for a PSC based on rubrene:P3HT bilayer and electrodeposited ZnO NRs with neglible hysteresis[22].

2.2 Experimental

2.2.1 Electrochemical Deposition of ZnO NRs

The indium tin oxide (ITO)-coated glass substrates (15 Ω sq^{-1}, Luminescence tech. Corp.) were cleaned through sequential ultrasonic treatments with detergent, ultrapure H_2O, acetone and methanol for 15 min each. Prior to electrodeposition, a 0.25 M zinc acetate ($Zn(CH_3COO)_2$, Wako) in methanol:water (10:1) solution was spin-coated onto UV-O_3-treated ITO-glass substrate at 1500 rpm for 30 s. After drying at 100 °C for 15 min, the films were then annealed at 350 °C for 20 min to form ZnO compact layer[23].

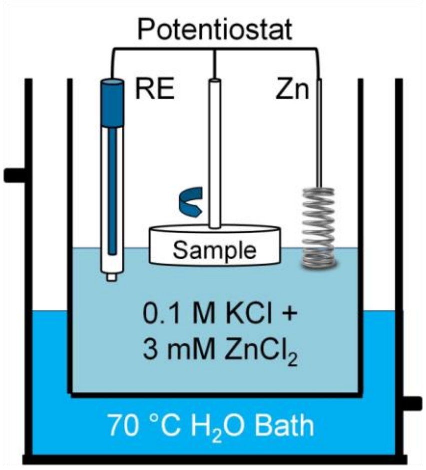

Figure 2.1 Illustration of the electrochemical deposition set-up.

A three-electrode electrochemical configuration was employed for the synthesis of ZnO NRs, as shown in Figure 2.1[24]. The seeded ITO-glass substrate acted as the working electrode, a Zn wire operated as the counter electrode, and saturated calomel electrode (SCE) worked as the reference electrode. The substrates were fixed to a rotating electrode with a constant rotation speed of 100 rotations per minute (rpm). The deposition bath was maintained at 70 °C containing 0.05 M KCl (99.5%, Nacalai Tesque) and 5 mM $ZnCl_2$ (98%, Nacalai Tesque). The electrolyte was saturated with pure O_2 by bubbling through a glass frit before and during the growth process. The effective area of the electrodeposited surface was about 1.54 cm^2. Electrodeposition was performed at a constant applied voltage of −1.0 V/SCE for 10−20 min using a Hokuto Denko HSV-110 potentiostat. After deposition, the samples were immediately rinsed with deionized water and annealed in air at 350 °C for 1 h. Finally, the samples were transferred to a nitrogen-filled glove box for perovskite deposition.

2.2.2 Solar Cell Assembly

The $CH_3NH_3PbI_3$ layer was deposited on top of ZnO NRs using fast deposition crystallization as reported in the literature[25]. The perovskite precursor solution (45 wt%) was prepared by mixing 1:1 mole ratio of PbI_2 (99.999%, Wako) and CH_3NH_3I (98.0%, Wako), respectively, in 1 mL of anhydrous N,N-dimethylformamide (DMF, Wako). Then, a 60 µL of this perovskite precursor solution was spin coated on top of electrodeposited ZnO NRs for 30 s. The substrates were spun at 5000 rpm and after 8 s, 50 µL of toluene was quickly dropped onto the center of the substrate and followed by thermal annealing at 70 °C for 10 min. After cooling at room temperature, 60 µL of rubrene in toluene solution (5 mg/mL) was spin-coated on top of the perovskite layer and the films were placed in a vacuum chamber for 15 min. Subsequently, P3HT (Sigma Aldrich) in chlorobenzene solution (15 mg/mL, Wako) was spin-coated at 1500 rpm for 120 s. For complete drying of P3HT layer, the samples were then stored in nitrogen-filled glove box for 12 h in dark. Finally, 50 nm Ag electrodes were deposited by thermal evaporation under a base pressure of 2×10^{-4} Pa. The active area of the devices is 0.09 cm^2. The solar cell devices were completed by putting silver paste in the electrode areas and stored again in vacuum to dry up before measurements (Figure 2.2).

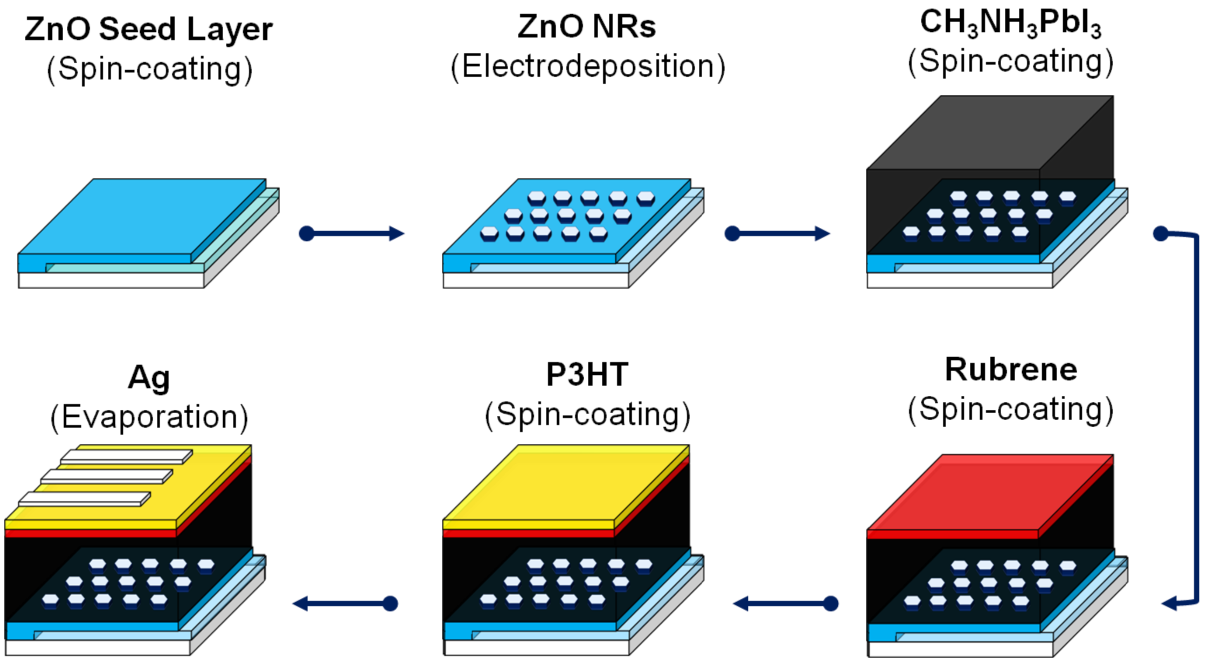

Figure 2.2 Systematic fabrication process of electrodeposited ZnO NRs-based PSC.

2.2.3 Device and Materials Characterization

The top-view and cross-sectional images were taken by a low-vacuum scanning electron microscope (SEM, Hitachi SU6600). The focused ion beam-assisted (Hitachi FB2200) cross-sectional SEM image and elemental EDX mapping analysis were obtained through ultra-high-resolution field emission scanning electron microscope (UHR FE-SEM, Hitachi SU9900). Atomic force microscopy (AFM) images were taken using a scanning probe microscope (Seiko SPA-400). Raman scattering measurement was performed at room temperature using a JASCO NRS-4100 Raman Spectrometer. The XRD patterns were characterized by a Rigaku X-ray diffractometer (RINT-TTR III) with CuK_α radiation (λ= 1.542 Å). The optical transmission and absorption spectra of the films were obtained on a UV-Vis spectrophotometer (JASCO V-530). Photoluminescence spectra were measured under ultraviolet excitation (λ_{ex} = 365 nm) using a high-pressure mercury-vapour light source (Olympus BH2-RFL-T3) coupled with a microscope (Olympus BX51) and a CCD spectrometer (Hamamatsu PMA-12). Current-voltage (J-V) curves were recorded from a Keithley 2611B System Source Meter unit under AM 1.5G illumination (100 mW cm^{-2}, Bunko-keiki, CEP-2000RP). The external quantum efficiency (EQE) spectra were obtained under illumination of monochromatic light using the same system at an intensity of 1.25 mW cm^{-2}.

2.3 Results and Discussion

2.3.1 Morphological, Structural and Optical Properties of Electrodeposited ZnO

First, a methanolic solution of $Zn(CH_3COO)_2$ was spin-coated on top of cleaned ITO/glass substrates to form a compact layer of ZnO nanocrystals (NCs) with an average thickness of 30 nm. These NCs operate as a compact hole-blocking layer and as nucleation sites for NR growth simultaneously. The ZnO NRs for electron extraction were grown on the seeded substrates by electrochemical deposition for 10−20 min using 0.05 M KCl and 5 mM $ZnCl_2$ with an applied potential of −1.0 V vs. SCE at a temperature of 70 °C. Through application of a cathodic potential, OH^- ions (eqn 1) are electrochemically generated which increases the local pH near the seed layer-ITO electrode surface. At the same time, these OH^- ions react with Zn^{2+} ions, which eventually result in the precipitation of ZnO crystals, as shown in Eq. (2):

$$O_{2(g)} + 2H_2O_{(l)} + 4e^- \rightarrow 4OH^- \qquad (1)$$

$$Zn^{2+}_{(aq)} + 2OH^-_{(aq)} \rightarrow ZnO + H_2O \qquad (2)$$

Figure 2.3 illustrates the variation of current density with time of the electrodeposited ZnO NRs. The curves have similar features observed from the electrodeposition of ZnO using nitrate and chloride media[26, 27]. The measured current is due to the reduction reaction of molecular O_2 in the electrolyte. The application of the negative potential to the system initiated a sudden increase in current.

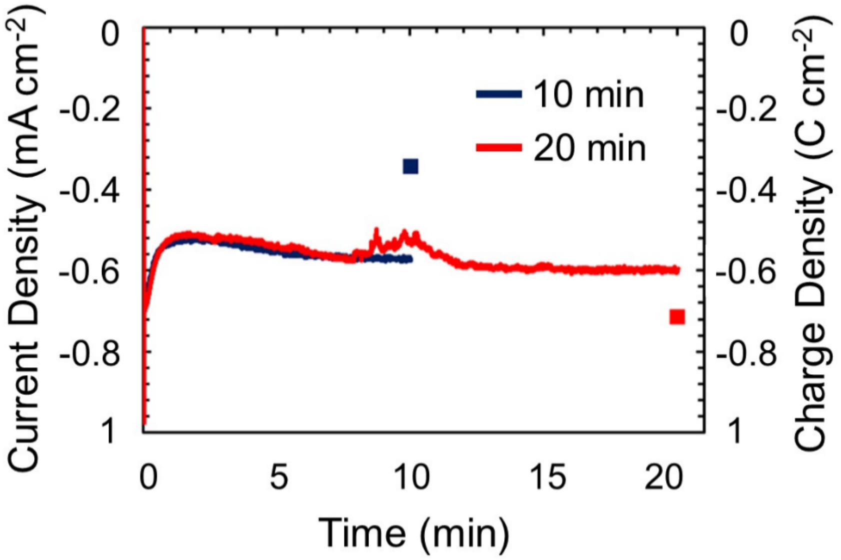

Figure 2.3 Variation of current density (lines) as a function of electrochemical deposition time and total electrical charge density exchanged (square dots) for two deposition potentials.

At this instant, nucleation immediately starts and the active surface area rapidly increases due to the three-dimensional growth of each newly formed ZnO crystal[28]. Additionally, the current density reached a maximum value of 0.95 mA cm^{-2} at around 1.5 s, which can be linked with the coalescence of nuclei. After 1 min, the deposition current reached a plateau at the range of 0.55–0.60 mA cm^{-2} specifying that the electrodeposited ZnO film now completely covers the existing seed layer. The total electrical charge density exchanged at the end of deposition process for each sample is also plotted in Figure 2.3.

Table 2.1 Electrochemically deposited ZnO NRs parameters as a function of deposition time.

Deposition time (min)	J (mA cm^{-2})	Q (C cm^{-2})	Calculated thickness (nm)	Measured thickness (nm)	Diameter (nm)	E_g (eV)
10	0.572	0.3432	258	260	52	3.24
20	0.596	0.7152	538	580	90	3.22

Consequently, the theoretical thickness of the electrodeposited ZnO film was estimated from the total electrical charge density exchanged using eqn. (3)[26]:

$$T = (Q.M_{\mathrm{W}})/(nF.\rho) \quad (3)$$

where, T is the thickness, Q is the total electrical charge density exchanged, M_{W} is the molecular weight of ZnO (81.41 g mol^{-1}), n is the number of electrons consumed in the electrochemical reactions eqns. (1) and (2), F is the Faraday's constant (96, 495 C mol^{-1}), and ρ is the density of ZnO (5.61 g cm^{-3}). The calculated thicknesses are then compared with actual measured thicknesses based on SEM images (Figure 2.4). As shown in Table 2.1, the actual values are slightly higher than the calculated ones and their difference increases with deposition time. Figure 2.4 shows the surface morphologies of the deposited ZnO films. Images (Figure 2.4(b) and (d)) are their corresponding cross-sectional images with perovskite film on top of each sample. Hexagonal ZnO NRs with a mean diameter of about 52 nm and thickness of ~ 260 nm were obtained, after 10 min deposition (Figure 2.4(a)). Increasing the deposition time to 20 min initiated the evolution of clustered flat-topped ZnO NRs, possibly through Ostwald ripening. These NRs have larger mean diameter of ~ 90 nm and thickness of ~ 580 nm, as seen in Figure 2.4(c). Large spaces can be seen between the clustered NRs due to their high aspect ratio. These regions are critical for better penetration of perovskite since it could lead to higher light absorption. A close inspection of the cross-sectional view of the 20 min-sample reveals the presence of some voids along the NRs length. These bulk surface defects caused the underestimation of the calculated thicknesses when compared to the measured values.

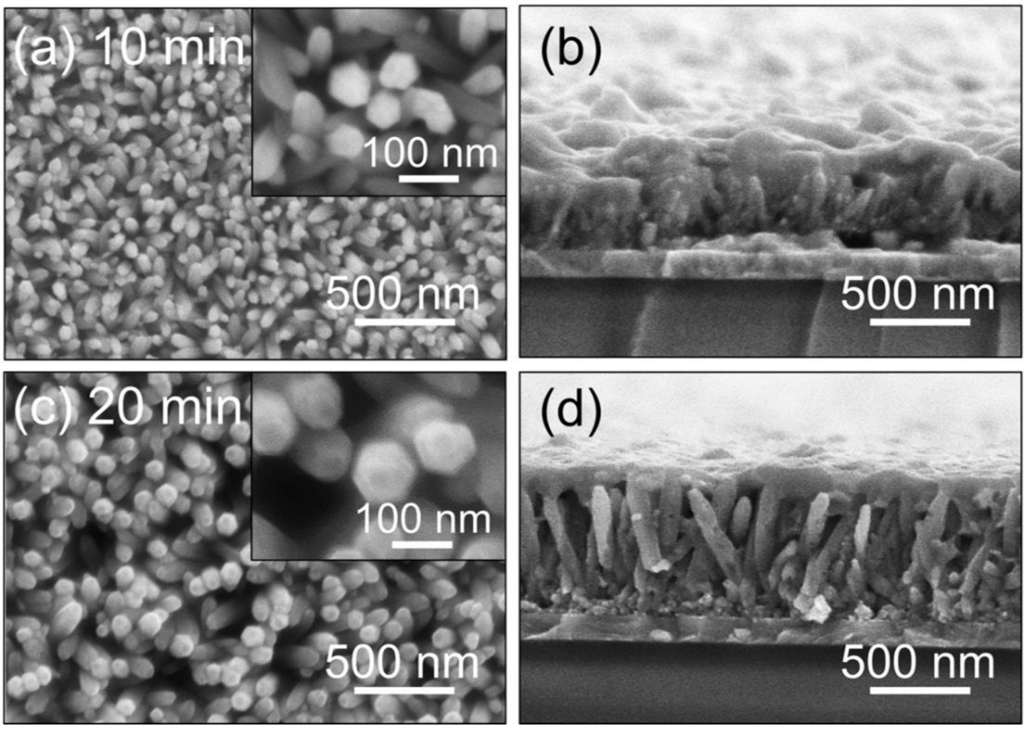

Figure 2.4 SEM images of electrochemically deposited ZnO NRs for (a) 10 min and (c) 20 min. Images (b) and (d) are their corresponding cross-sectional views with perovskite film on top of each sample.

Figure 2.5(a) shows the Raman spectra of the electrodeposited ZnO NRs under excitation of a 532 nm laser line. The dominant peaks at 99 cm^{-1} and 438 cm^{-1} are attributed to the E_2 (low) and E_2 (high) modes of non-polar optical phonons, respectively. In addition, the small peak at around 333 cm^{-1} can be related to the E_2 (high)-E_2 (low) multiphonon mode. The A_1 (low) phonon mode at 569 cm^{-1} is characteristically induced by defects such as oxygen vacancies and zinc interstitials[29]. The high crystallinity of electrodeposited ZnO NRs was verified by the existence of intense peaks and narrow line widths of the E_2-mode peaks. It should be noted that ZnO peaks on Raman patterns have intensified at longer reaction time signifying the increase in ZnO concentration on the surface of the substrate.

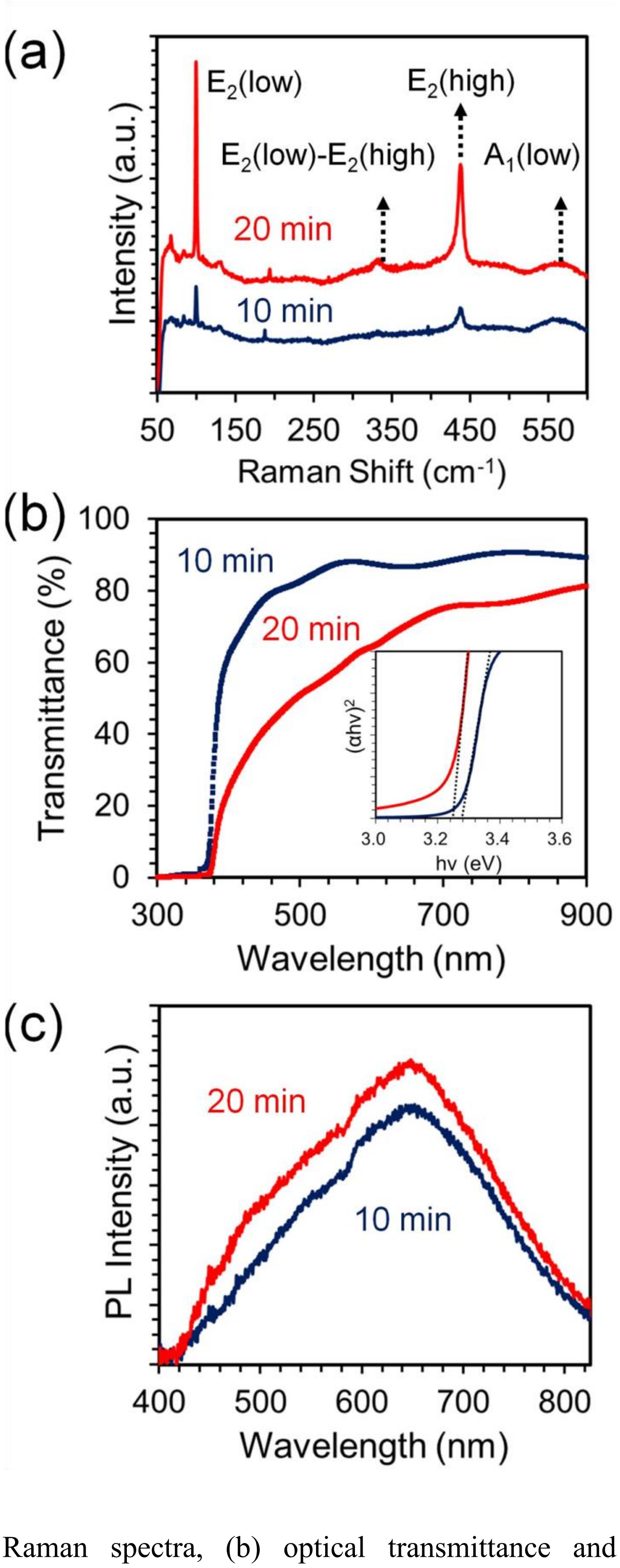

Figure 2.5 (a) Raman spectra, (b) optical transmittance and (c) room temperature photoluminescence spectra of electrochemically deposited ZnO NRs for 10 and 20 min.

The optical transmission spectra of electrodeposited ZnO NRs are presented in Figure 2.5(b). The 10-min-ZnO sample displayed a higher transmittance of 86% at 600 nm compared with 64% of the 20-min-ZnO sample. The lower transmittance of the 20 min-ZnO sample can be correlated to its higher thickness and moderately tilted orientation of NRs which resulted in the Rayleigh scattering of light[30]. The ZnO band gap was also estimated using the absorption edge of each sample and tabulated in Table 2.1. The 20-min-ZnO sample has a lower band gap due to its larger dimensions. Figure 2.5(c) shows room temperature photoluminescence spectra of ZnO NRs. Under excitation wavelength of 365 nm, both samples exhibited a major orange-red emission peak centered at 650 nm (1.90 eV) which originated from deep level oxygen interstitials (O_i) [31].

2.3.2 Charge Transfer Characteristics

The focused ion beam (FIB)-assisted cross-sectional SEM image and the energy level diagram of the PSC utilized in this study are shown in Figure 2.6(a) and (c), respectively. The device has a configuration of glass/ITO/ZnO seed layer/20-min-ZnO NRs/$CH_3NH_3PbI_3$/rubrene:P3HT/Ag, where the nanostructured ZnO and rubrene:P3HT bilayer function as the ETL and HTL, respectively. Figure 2.6(b) illustrates the molecular structure of rubrene. It can be noted that rubrene has the same HOMO level (−5.4 eV) with $CH_3NH_3PbI_3$ and lower HOMO level (−5.0 eV) than P3HT. This band alignment suggests that holes can be transferred more easily at the rubrene/$CH_3NH_3PbI_3$ interface than the P3HT/$CH_3NH_3PbI_3$ interface.

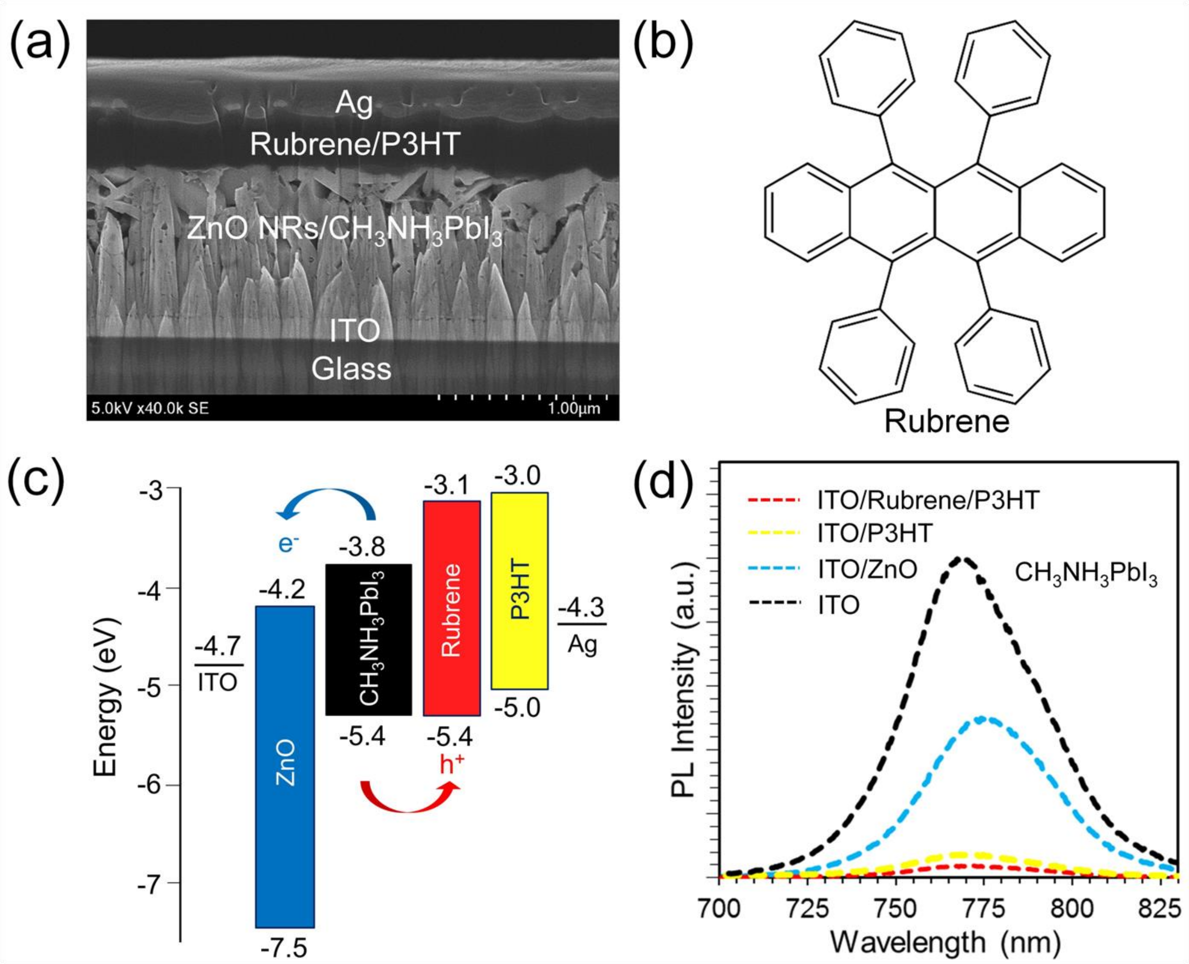

Figure 2.6 (a) FIB-assisted cross-sectional SEM image of PSC based on electrochemically deposited ZnO and rubrene:P3HT bilayer. (b) Molecular structure of a rubrene molecule. (c) Energy band diagram and (d) steady-state photoluminescence spectra of perovskite films: glass/ITO/$CH_3NH_3PbI_3$ (black), glass/ITO/ZnO NRs/$CH_3NH_3PbI_3$ (blue), glass/ITO/$CH_3NH_3PbI_3$/P3HT (yellow), and glass/ITO/$CH_3NH_3PbI_3$/rubrene/P3HT (red).

To confirm the synergistic effect of electrodeposited ZnO NRs and rubrene:P3HT bilayer on the charge transfer process of PSCs, we performed steady-state photoluminescence of glass/ITO/perovskite, glass/ITO/ZnO NRs/perovskite, glass/ITO/perovskite/P3HT, and glass/ITO/perovskite/rubrene:P3HT, as shown in Figure 2.6(d). The strong photoluminescence peak at 770 nm reveals that the perovskite film formed using one-step solution process has a high structural quality. Furthermore, about ~45% PL quenching was observed when perovskite was deposited on top of ZnO NRs, which validates the electron extraction capability of electrodeposited ZnO. On the other hand, $CH_3NH_3PbI_3$ emission peak was quenched by almost 90% upon contact with P3HT which is in agreement with the literature[32]. Interestingly, the PL intensity was further reduced up to 97% when rubrene was deposited between perovskite and P3HT. This signifies that a more efficient hole-transport process occurs between $CH_3NH_3PbI_3$ and P3HT with rubrene as interlayer.

The cross-sectional elemental mapping acquired by energy dispersive X-ray (EDX) analysis is presented in Figure 2.7. The Zn signal matches well with the seed layer and NR morphology of ZnO layer. The I and Pb signals indicate that the perovskite film is uniformly distributed and has infiltrated the voids between each NR. Furthermore, the strong S and C signals follow the shape of the P3HT layer. Some C signals below the P3HT layer could be linked with the perovskite material and rubrene interlayer. Finally, the Ag signal corresponds with the silver electrode. These results demonstrate that there is no evidence of layer-by-layer mixing and all the elemental mappings are in good agreement with the device structure as shown in Figure 2.6(a).

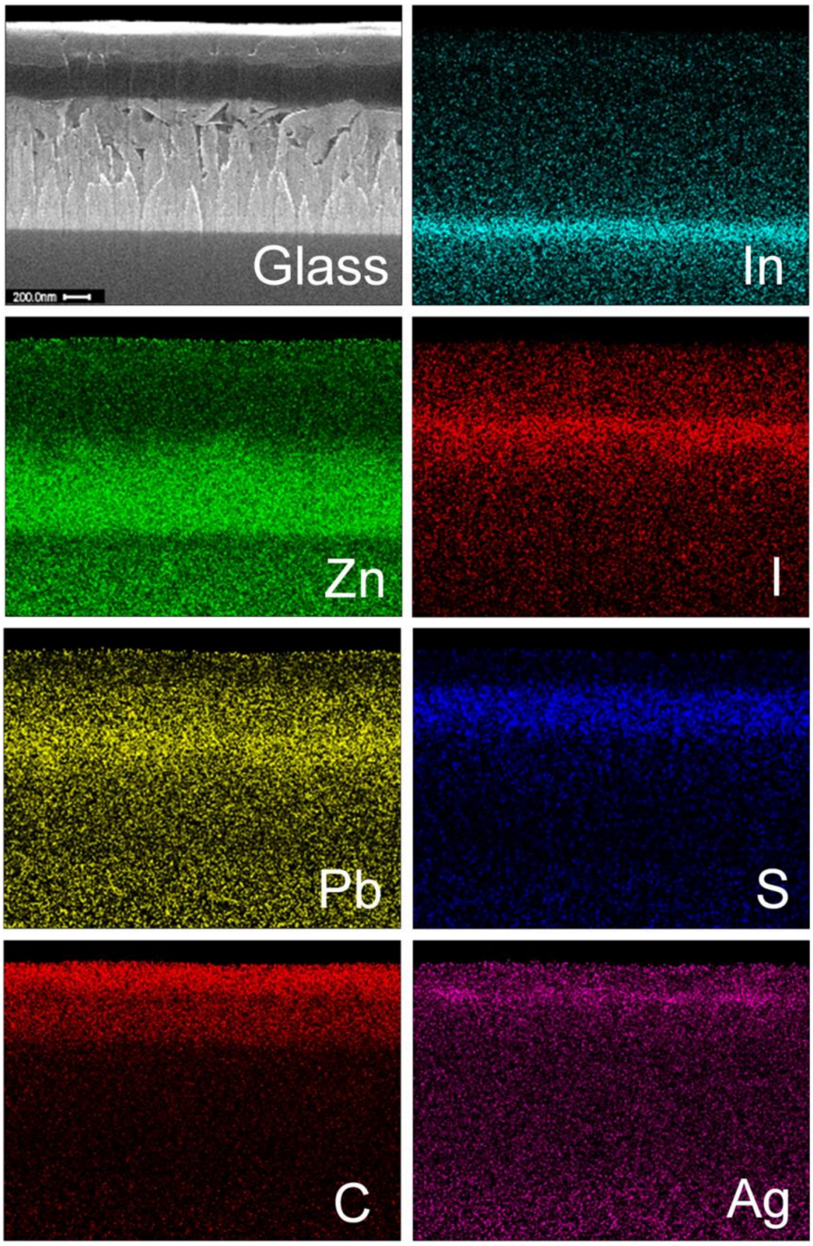

Figure 2.7 Cross-sectional elemental mapping of electrochemically deposited ZnO NRs-based PSC with rubrene:P3HT hole transporting layers.

Figure 2.8 shows the cross-sectional and top view SEM images of the as-prepared $CH_3NH_3PbI_3$ film on top of the ZnO NRs. Porous and coarse perovskite film was formed on top of the 10-min-ZnO sample, whereas a smoother film with larger crystallite size was obtained on top of the 20-min-ZnO NRs. Lesser number of pinholes can also be seen for the latter sample.

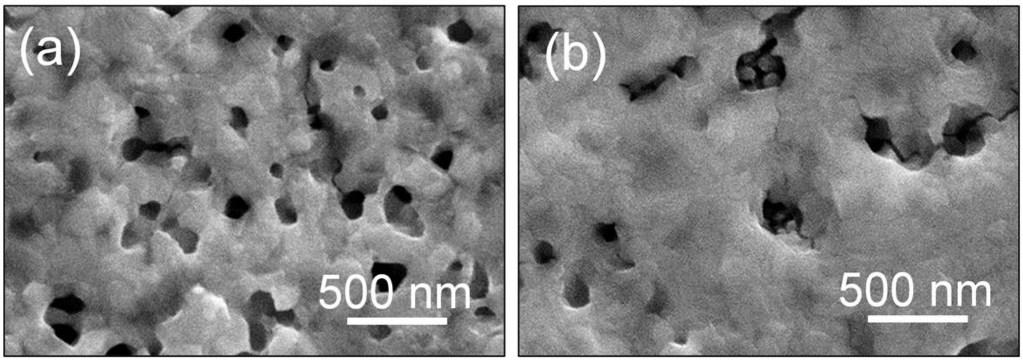

Figure 2.8 SEM images of perovskite films on top of electrochemically deposited ZnO NRs for 10 and 20 mins.

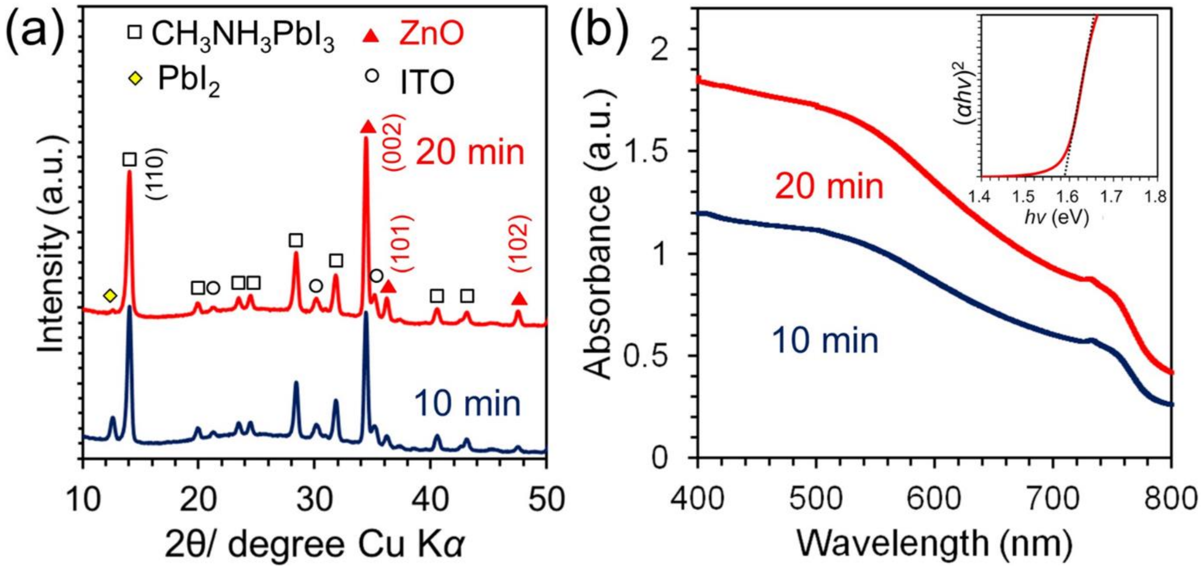

Figure 2.9 (a) XRD patterns and (b) optical absorption spectra of perovskite films on top of electrochemically deposited ZnO NRs. Inset: Tauc plot of perovskite film on top of 20 min-ZnO sample.

Figure 2.9(a) and (b) exhibit the XRD pattern and absorption spectra of the perovskite films. Both patterns exhibit a dominant peak at $2\theta = 34.45°$ that can be indexed to the (002) plane of hexagonal wurtzite crystal structure of ZnO. Major peaks (with square) can also be indexed to the tetragonal crystal structure of $CH_3NH_3PbI_3$ (See Appendix, Table 2). It should be noted that a stronger peak intensity at $2\theta = 12.6°$ was detected for the 10-min ZnO-perovskite bilayer, denoting a higher amount of unreacted PbI_2 precursor. Additionally, ZnO/perovskite bilayers exhibit panchromatic absorption of light. It can be seen that the 20-min-ZnO/perovskite sample absorbs more light than the 10-min-ZnO/perovskite sample. This could be due to higher perovskite loading in the clustered NRs formed after 20 min deposition. The band edge analysis shows that the perovskite films has a band gap of E_g = 1.59 eV which is suitable for solar cell application.

2.3.3 Device Performance

Figure 2.10(a) and Table 2.2 present the photocurrent (J)-voltage (V) curves in reverse scan under simulated AM1.5G illumination (100 mW cm^{-2}) and the complete photovoltaic parameters with statistical results in different scan directions, respectively. We first determine the effect of rubrene interlayer by fabricating PSCs with and without rubrene using the 10 min-ZnO NRs as electron selective layer. As shown in Table 2.2, the device without rubrene exhibited an average short circuit current density (J_{sc}) of 15.4 mA cm^{-2}, open circuit voltage (V_{oc}) of 0.58 V, fill factor (FF) of 0.37, maximum PCE (PCE_{max}) of 3.4% and average PCE (PCE_{ave}) of 3.3%. On the other hand, upon addition of rubrene interlayer between the perovskite and P3HT, most photovoltaic parameters increased including average J_{sc} (17.5 mA cm^{-2}), FF (0.40), PCE_{max} (4.3%) and PCE_{ave} (3.6%). This increase could be possibly attributed to the filling effect of rubrene:P3HT bilayer, resulting in reduced leakage current and better interfacial area between the active layer and HTL. However, the relatively low V_{oc} values for both devices could be related to the utilization of P3HT as main hole-selective layer. It is well known to have a low hole mobility, low charge carrier density and higher recombination rate than spiro-OMeTAD[33, 34]. Another possible reason for these relatively low V_{oc} values could be due to the presence of pinholes in perovskite layer leading to the direct contact between the NRs and hole-transporting materials.

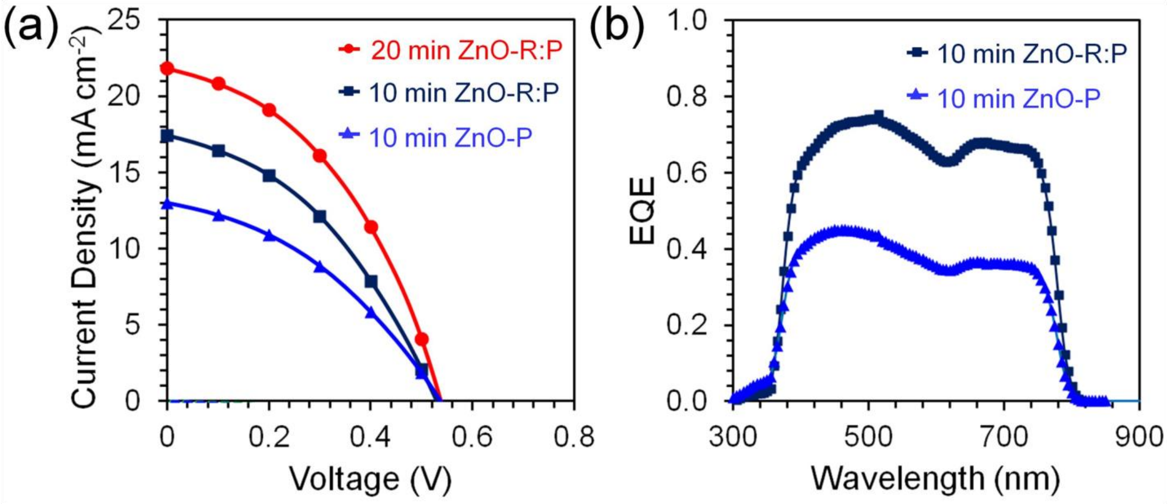

Figure 2.10 (a) *J-V* curves and (b) EQE spectra for PSCs based on electrochemically deposited ZnO NRs and rubrene:P3HT bilayer.

Figure 2.10(b) presents the external quantum efficiencies (*EQE*) of the 10-min-ZnO NR based devices with and without rubrene interlayer. As expected, the solar cell device with rubrene:P3HT bilayer displayed a higher *EQE* over the entire wavelength range than the P3HT only-device, which is in agreement with the J_{sc} trend in Table 2. The current generation starts at around λ = 800 nm for both devices, which is compatible with the band gap of perovskite layer. Additionally, the EQE peak at λ = 680 nm, which is followed by a dip at λ = 615 nm, is possibly triggered by the absorption edge of P3HT[35, 36].

To further confirm the beneficial effect of the addition of rubrene on the device performance, we observed the surface morphology evolution of HTLs on top of electrodeposited ZnO NRs/perovskite heterostructure, as shown in Figure 2.11. Fiber-like microstructures were obtained when P3HT solution is directly spin-coated on perovskite film, as shown in Figure 2.11(a).

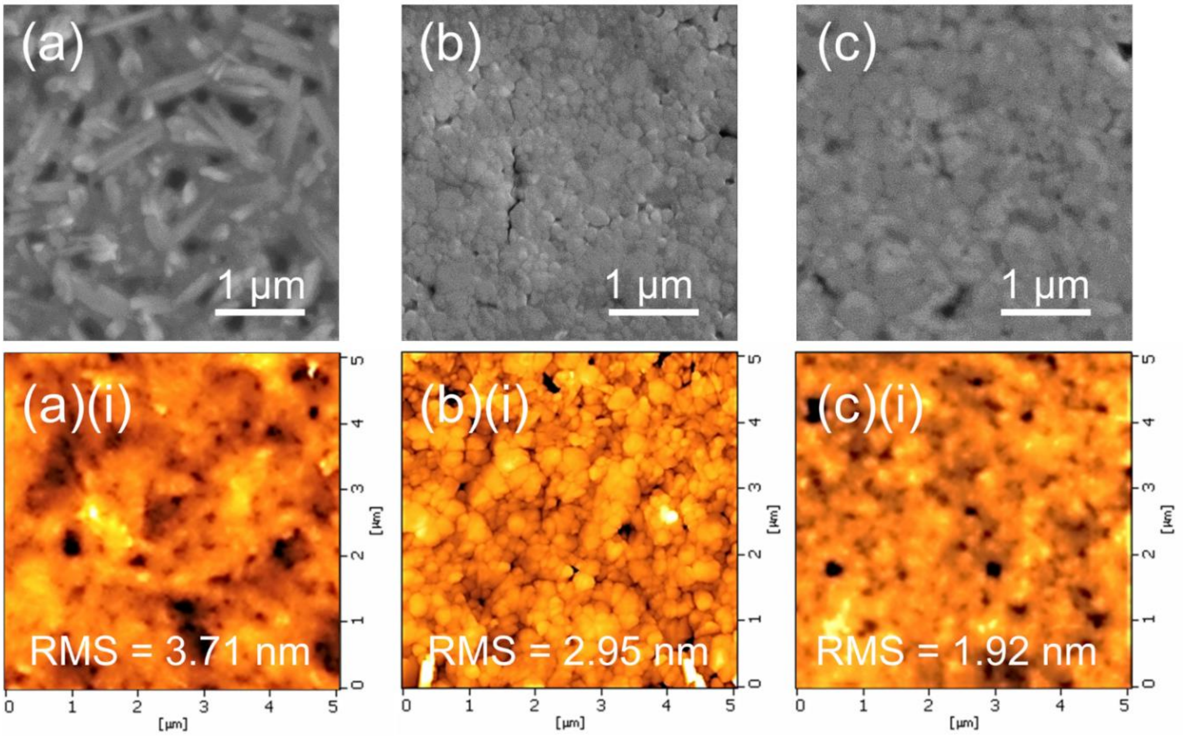

Figure 2.11 SEM images of (a) $CH_3NH_3PbI_3$/P3HT (b) $CH_3NH_3PbI_3$/rubrene and (c) $CH_3NH_3PbI_3$/rubrene/P3HT spin-coated on top of electrochemically deposited ZnO NRs. Images with (i) are their corresponding AFM images.

This P3HT layer shows a root-mean-square (rms) roughness of 3.71 nm (Figure 2.11(a)(i) with some pinholes in the range of 200−500 nm. On the other hand, rubrene layer covered the pinholes of the perovskite film and penetrated its grain boundaries effectively. The rubrene layer is composed of smooth grains with a mean diameter of ~ 100 nm and smaller rms roughness of 2.95 nm (Figure 2.11(b)(i)). Figure 2.11(c) shows that the addition of P3HT on top of rubrene layer further filled the grain boundaries of perovskite film with a smoother surface roughness of 1.92 nm. These results show that the passivation of perovskite film by rubrene clearly improved the interfacial area between the hole-selective materials and the absorber layer. In turn, this led to the reduction of leakage current resulting in a higher photocurrent generation and better photovoltaic performance.

Table 2.2 Summary of photovoltaic parameters recorded for PSCs based on electrochemically deposited ZnO NRs and rubrene:P3HT bilayer, under 1 sun illumination (AM 1.5G, 100 mW cm^{-2}).

ETL/HTL	Scan direction	J_{sc} (mA cm^{-2})	V_{oc} (eV)	FF	PCE_{ave} (%)	PCE_{max} (%)	Hysteresis index
20 min ZnO/Ru:P3HT	forward	19.0 ± 3.7	0.50 ± 0.11	0.38 ± 0.07	3.62 ± 1.1	4.87	0.020
	reverse	19.0 ± 3.8	0.51 ± 0.12	0.40 ± 0.02	3.82 ± 0.9	4.84	
10 min ZnO/Ru:P3HT	forward	16.0 ± 2.2	0.52 ± 0.02	0.40 ± 0.03	3.36 ± 0.8	4.29	0.086
	reverse	17.5 ± 1.4	0.52 ± 0.04	0.40 ± 0.03	3.61 ± 0.3	3.86	
10 min ZnO/P3HT	forward	13.7 ± 1.0	0.56 ± 0.05	0.36 ± 0.01	2.77 ± 0.4	3.18	0.141
	reverse	15.4 ± 0.7	0.58 ± 0.03	0.37 ± 0.00	3.33 ± 0.1	3.43	

Moreover, the 20-min-ZnO NRs based device with rubrene:P3HT bilayer exhibited the highest average J_{sc} of 19 mA cm^{-2}, PCE_{ave} of 3.8% and respectable PCE_{max} of 4.9%. This enhancement is possibly due to the suppression of recombination losses from the enhanced electron transport within the longer NRs and shorter path length for electron transfer[37, 38]. The increase in J_{sc} values (from 16−17.5 to 19 mA cm^{-2}) could also be associated to the clustered morphology of the 20 min-ZnO NRs which led to improved perovskite infiltration and light absorption, as seen in Figure 2.4(b)[39].

2.3.4 Hysteresis Behaviour

As shown in Table 2.2, the 10-min-ZnO NRs based PSC without rubrene exhibits stronger hysteresis compared with the devices having rubrene interlayer, as indicated by the difference of their efficiencies measured in forward (FS) and reverse (RS) scans. Herein, we quantify the hysteresis extent on PSCs by defining hysteresis index (*HI*) as Eq. 4 according to the literature[40]:

$$HI = \frac{J_{\mathrm{RS}}(0.6V_{\mathrm{OC}}) - J_{\mathrm{FS}}(0.6V_{\mathrm{OC}})}{J_{\mathrm{RS}}(0.6V_{\mathrm{OC}})} \qquad (4)$$

where, J_{RS} $(0.6V_{OC})$ and J_{FS} $(0.6V_{OC})$ represent photocurrent density at 60% of V_{OC} for reverse and forward scans, respectively. A HI of 0 denotes the absence of hysteresis, while a HI of 1 corresponds to the instance that the hysteresis is as high as the magnitude of the photocurrent[40]. According to the estimated *HI* values, the 20 min-ZnO NRs based PSC with rubrene passivation demonstrate the smallest *HI* value of 0.02. This means that the hysteresis behavior is synergistically diminished through the addition of rubrene interlayer and the utilization of longer NRs. Recently, most researchers associate the hysteresis effect through the ionic vacancy defect migration within the perovskite film which include Pb^{2+}, I^{-} and $CH_3NH_3^+$ (MA^+) ions[41]. Under increasing applied bias from 0 to V_{oc} of FS, these charged defects migrate towards the anode and cathode electrodes, and subsequently travel back into the bulk perovskite film under reducing applied potential of RS. This process initiates an accumulation of charges on the interface between the carrier extraction layers and the active layer and subsequently disrupts the collection of charge carriers' efficiency on both contacts[42]. Hence, through this mechanism, underestimation under FS and overestimation under RS usually occur, and the hysteresis behavior becomes more evident. Herein, we propose a mechanism for the suppression of hysteresis through the application of ZnO NRs and rubrene:P3HT bilayer as charge carrier selective contacts.

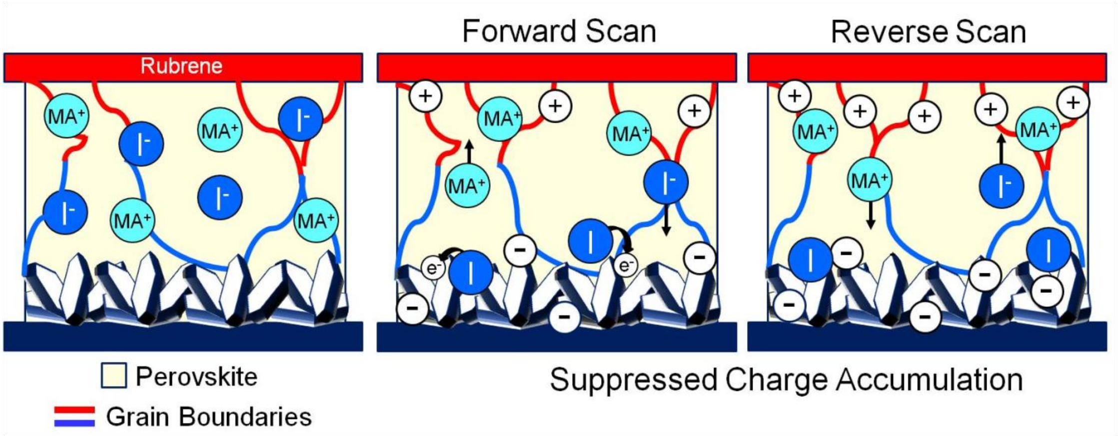

Figure 2.12 Schematic illustration of the synergistic effect of electrochemically deposited ZnO NRs and rubrene:P3HT bilayer to suppress hysteresis in PSC.

As shown in Figure 2.12, the ZnO NRs interact with I^- ions by converting them to I atoms. This process inhibits charge accumulation on the interface resulting in the stabilization of photocurrent generation at that part of the solar cell. In addition, the filling effect of rubrene layer on the grain boundaries of perovskite film greatly enhances the hole extraction process even in the presence of ionic defects. For the P3HT-only-device, the fiber-like microstructures of P3HT could not cover the grain boundaries of perovskite film effectively. This leads to the entrapment of generated holes simultaneously with the ionic defects along the grain boundaries of the active layer. These results indicate that rubrene is a promising passivation layer for efficient PSCs.

2.4 Summary

The synergistic effect of electrochemically deposited ZnO NRs and rubrene interlayer to enhance the photovoltaic performance of PSCs and suppress its hysteresis behavior is presented in this chapter. XRD, photoluminescence and Raman spectroscopy analyses showed that electrodeposited ZnO NRs had high-quality structural and optical properties. It was found out that the rubrene layer covered the pinholes of the perovskite film and penetrated its grain boundaries effectively. A PCE_{max} of 4.9% and PCE_{ave} of 3.8% were attained by a device based on 20 min-ZnO NRs and rubrene:P3HT bilayer. The devices with rubrene interlayer also displayed higher *EQE* over the whole wavelength range and reduced hysteresis behavior compared with the device having only P3HT as the HTL. Better perovskite infiltration, reduced charge carrier path length and at the same time improved photovoltaic parameters were observed by employing longer ZnO NRs as ETL. Based on the results, electrochemically deposited ZnO NRs and rubrene interlayer can work synergistically as ETL and HTL for efficient PSCs.

References

(1) S.-D. Baek, Y. Porte, Y. C. Kim and J.-M. Myoung, *J. Mater. Chem. C*, 2017, **5**, 9479–9487.

(2) J. B. You, C. C. Chen, L. T. Dou, S. Murase, H. S. Duan, S. A. Hawks, T. Xu, H. J. Son, L. P. Yu, G. Li and Y. Yang, *Adv. Mater.*, 2012, **24**, 5267–5272.

(3) Z. Zhao, N. Wang, H. Nan, L. Shen, C. Durkan and X. He, *J. Mater. Chem. C*, 2016, **4**, 5814-5821.

(4) Z. Kayani, R. Ishaque, B. Zulfiqar, S. Riaz and S. Naseem, *Opt. Quant. Electron.*, 2017, **49**, 223.

(5) M. R. Khajavi, D. J. Blackwood, G. Cabanero and R. Tena-Zaera, *Electrochim. Acta*, 2012, **69**, 181–189.

(6) Y. Lin, J. Yang and X. Zhou, *Appl. Surf. Sci.*, 2011, **258**, 1491-1494.

(7) S. Sun, S. Jiaon, K. Zhang, D. Wang, S. Gao, H. Li, J. Wang, Q. Yu, F. Guo and L. Zhao, *J. Cryst. Growth*, 2012, **359**, 15-19.

(8) J. Zhang, E. J. Juárez-Pérez, I. Mora-Seró, B. Vianaa and T. Pauporté, *J. Mater. Chem. A*, 2015, **3**, 4909-4915.

(9) Z. Liu, A Zhu, F. Cai, L. Tao, Y. Zhou, Z. Zhao, Q. Chen, Y. Cheng and H. Zhou, *J. Mater. Chem. A*, 2017, **5**, 6597-6605.

(10) Q. Xi, G. Gao, H. Zhou, Y. Zhao, C. Wu, L. Wang, P. Guo and J. Xu, *Nanoscale*, 2017, **9**, 6136-6144.

(11) N. Y. Nia, F. Matteocci, L. Cina and A. Di Carlo, *ChemSusChem*, 2017, **10**, 3854–3860.

(12) D. Huang, T. Goh, J. Kong, Y. Zheng, S. Zhao, Z. Xu and A. Taylor, *Nanoscale*, 2017, **9**, 4236-4243.

(13) R. S. Sanchez and E. Mas-Marza, *Sol. Energ. Mat. Sol. C*, 2016, **158**,189–194.

(14) Y. Song, S. Lv, X. Liu, X. Li, S. Wang, H. Wei, D. Li, Y. Xiao and Q. Meng, *Chem. Commun.*, 2014, **50**, 15239-15242.

(15) Q.-K. Wang, R.-B. Wang, P.-F. Shen, C. Li, Y.-Q. Li, L.-J. Liu, S. Duhm and J.-X. Tang, *Adv. Mater. Interfaces*, 2015, **2**, 1400528.

(16) P. Schulz, E. Edri, S. Kirmayer, G. Hodes, D. Cahen and A. Kahn, *Energy Environ. Sci.*, 2014, **7**, 1377–1381.

(17) K. Zhang, L. Wang, Y. Liang, S. Yang, J. Liang, F. Cheng and J. Chen, *Synth. Met.*, 2012, **162**, 490–496.

(18) J. Nitta, K. Miwa, N. Komiya, E. Annese, J. Fujii, S. Ono and K. Sakamoto, *Sci. Rep.*, 2019, **9**, 9645.

(19) C. Krellner, S. Haas, C. Goldmann, K. P. Pernstich, D. J. Gundlach, and B. Batlogg, *Phys. Rev. B*, 2007, **75**, 245115.

(20) N. Sato, K. Seki and H. Inokuchi, J. Chem. Soc., *Faraday Trans. 2*, 1981, **77**, 1621.

(21) J. Emara, T. Schnier, N. Pourdavoud, T. Riedl, K. Meerholz and S. Olthof, *Adv. Mater.*, 2016, **28**, 553–559.

(22) C. M. O. Pelicano and H. Yanagi, *J. Energy Chem.*, 2018, **27**, 455-462.

(23) C. M. Pelicano and H. Yanagi, *J. Mater. Chem. C*, 2017, **5**, 8059-8070.

(24) J.T. Damasco-Ty and H. Yanagi, *Jpn. J. Appl. Phys.*, 2015, **54**, 04DK05.

(25) M. Xiao, F. Huang, W. Huang, Y. Dkhissi, Y. Zhu, J. Etheridge, A. Gray-Weale, U. Bach, Y.-B. Cheng and L. Spiccia, *Angewandte Chemie*, 2015, **126**, 10056-10061.

(26) J. Zhang and T. Pauport´e, *J. Phys. Chem. C*, 2015, **119**, 14919– 14928.

(27) T. Pauporté and I. Jirka, *Electrochim.Acta*, 2009, **54**, 7558.

(28) T. Pauporte´ and D. Lincot, *Electrochimica Acta*, 2000, **45**, 3345–3353.

(29) A. K. Pradhan, K. Zhang, G. Loutts, U. Roy, Y. Cui and A. Burger, *J Phys: Condens Matter*, 2004, **16**, 7123.

(30) H. Park, K.-J. Byeon, K.-Y. Yang, J.-Y. Cho and H. Lee, *Nanotechnology*, 2010, **21**, 355304.

(31) L. Wu, Y. Wu, X. Pan and F. Kong, *Optical Materials*, 2006, **28**, 418-422.

(32) C. Wehrenfennig, M. Liu, H. J. Snaith, M. B. Johnston and L. M. Herz, *J. Phys. Chem. Lett.*, 2014, **5**, 1300-1306.

(33) Y. Guo, C. Liu, K. Inoue, K. Harano, H. Tanaka and E. Nakamura, *J. Mater. Chem. A*, 2014, **2**, 13827–13830.

(34) D. Bi, L. Yang, G. Boschloo, A. Hagfeldt and E.M.J. Johansson, *J. Phys. Chem. Lett.*, 2013, **4**, 1532–1536.

(35) M. Seetharaman S, P. Nagarjuna, P. N. Kumar, S. P. Singh, M. Deepac and M. A. G. Namboothiry, *Phys. Chem. Chem. Phys.*, 2014, **16**, 24691-24696.

(36) K. Rahimi, I. Botiz, J. O. Agumba, S. Motamen, N. Stingelin and G. Reiter, *RSC Adv.*, 2014, **4**, 11121.

(37) D. H. Kim, G. S. Han, W. M. Seong, J. W. Lee, B. J. Kim, N. G. Park, K. S. Hong, S. Lee and H. S. Jung, *ChemSusChem*, 2015, **8**, 2392-2398.

(38) J-H. Im, J. Luo, M. Franckevičius, N. Pellet, P. Gao, T. Moehl, S. M. Zakeeruddin, M. K. Nazeeruddin, M. Grätzel and N-G. Park, *Nano Letters*, 2015, **15**, 2120-2126.

(39) F. J. Ramos, M. C. López-Santos, E. Guillén, M. K. Nazeeruddin, M. Grätzel, A. R. Gonzalez-Elipe and S. Ahmad, *ChemPhysChem*, 2014, **15**, 1148-1153.

(40) C. Liu, J. Fan, X. Zhang, Y. Shen, L. Yang and Y. Mai, *ACS Appl. Mater. Interfaces*, 2015, **7**, 9066−9071.

(41) C. Eames, J. M. Frost, P. R. F. Barnes, B. C. O'Regan, A. Walsh and M. S. Islam, *Nat. Commun.*, 2015, **6**, 7497.

(42) J. Shao, S. Yang, L. Lei, Q. Cao, Y. Yu and Y. Liu, *Chem. Mater.*, 2016, **28**, 7134–7144.

Chapter 3

Perovskite Solar Cells Based on Nanostructured ZnO Films Designed via Low Temperature H_2O Oxidation

3.1 Effect of Oxidation Time and Temperature on H_2O-Oxidized Nanostructured ZnO Films for Perovskite Solar Cells

3.1.1 Introduction

In the previous chapter, electrochemical deposition was presented as an alternative low temperature technique for generating high-quality ZnO films. However, it still uses a complex set-up and substantial amount of chemical reagents. Herein, we present the strategic design of nanostructured ZnO from Zn thin films via H_2O oxidation and its application as electron-transporting layer (ETL) in perovskite solar cells (PSCs). H_2O oxidation technique offers a facile, low temperature ($T < 100°C$), environmental friendly and economical fabrication of different ZnO surface morphologies. The formation of nanostructures (NSs) from Zn thin film is induced by solely utilizing ultrapure H_2O avoiding contamination issues.

We initially employed H_2O-oxidized nanostructured ZnO films as ETL in organic-inorganic hybrid solar cells (glass/ITO/ZnO/P3HT:PCBM/MoO_3/Au) achieving a PCE_{max} of 1.18%[1].

In this study, H_2O oxidation is further optimized to determine the ideal parameters that could synthesize suitable morphologies for solar cell applications. Accordingly, various surface architectures were tailored through varying growth time and H_2O temperature. To establish the potential of H_2O-oxidized ZnO as ETL, we fabricated a simple device with a configuration of glass/ITO/ZnO nanorods (NRs)/perovskite/P3HT/Ag, resulting in a respectable PCE_{max} of ≈ 6%. This *PCE* is higher than its electrochemically deposited ZnO-based device counterpart having the same ZnO thickness and configuration. Moreover, H_2O-oxidized ZnO-based solar cells displayed low hysteresis and excellent stability. Based on these results, we established that simple oxidation of Zn in H_2O could produce high quality ZnO NSs that can be utilized for solar cells[2].

3.1.2 Experimental

3.1.2.1 Formation of ZnO NRs by H_2O oxidation

Indium tin oxide (ITO)-coated glass substrates (15 Ω sq^{-1}, 0.80 mm thick, Luminescence Tech. Corp.) were etched from regions under the anode contact by HCl and Zn paste. The substrates were then cleaned sequentially with detergent, distilled H_2O, acetone and methanol for 15 min each in an ultrasonic bath. After drying, the substrates were treated by UV ozone cleaner for 10 min to remove organic impurities. Prior to Zn thin film vacuum deposition, a 0.25M zinc acetate ($Zn(CH_3COO)_2$, Wako) in methanol:H_2O (10:1) solution was spin-coated onto cleaned ITO-glass substrate at 1500 rpm for 30s. The films were dried first at 100°C for 15 min and then annealed at 350°C for 20 min to form ZnO compact layer. Zn thin films were then deposited on top of ZnO compact layer samples by a vacuum evaporator (JEOL JEE-400) at a base pressure of $4x10^{-4}$ Pa. The thermally evaporated Zn thin films were subsequently immersed in ultrapure H_2O at varying temperatures (room temperature, 50°C, 70°C, and 90°C) for 2-24 h to form nanostructured ZnO. The H_2O-oxidized ZnO samples were washed with H_2O and then dried at 350°C for 1h. Finally, the glass/ITO/ZnO samples were transferred to a nitrogen-filled glove box for the film deposition.

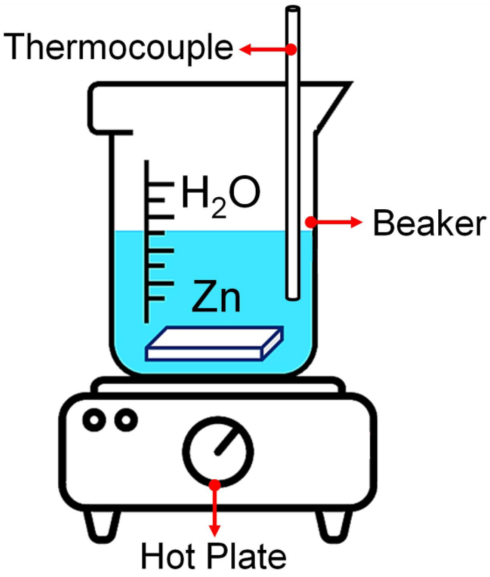

Figure 3.1 Illustration of the H_2O oxidation set-up.

3.1.2.2 Solar Cell Assembly

The $CH_3NH_3PbI_3$ layer was deposited on top of ZnO NSs using fast deposition crystallization as reported in the literature[3]. The perovskite precursor solution (45 wt%) was prepared by mixing 1.2 mmol of PbI_2 (99.999%, Wako) and 1.2 mmol of CH_3NH_3I (98.0%, Wako) in 1 mL of anhydrous N,N-dimethylformamide (DMF, Wako). A 60 µL of perovskite precursor solution was spin coated onto the substrates for 30 s. The substrates were spun at

5000 rpm and after 4-6 seconds, 150 µL of toluene was quickly dropped onto the center of the substrate and followed by thermal annealing at 70°C for 10 min. After cooling at room temperature, 60 µL of P3HT (Sigma Aldrich) in chlorobenzene (15 mg/mL, Wako) was spin-coated at 1500 rpm for 120 s. For complete drying of P3HT layer, the samples were then stored in nitrogen-filled glove box for 12 h under dark conditions. Finally, 50 nm Ag electrodes were deposited by thermal evaporation under a base pressure of 2x10^{-4} Pa. The active area of the devices is 0.09 cm^2. The solar cell devices were completed by putting silver paste in the electrode areas and stored again in vacuum to dry up before measurements.

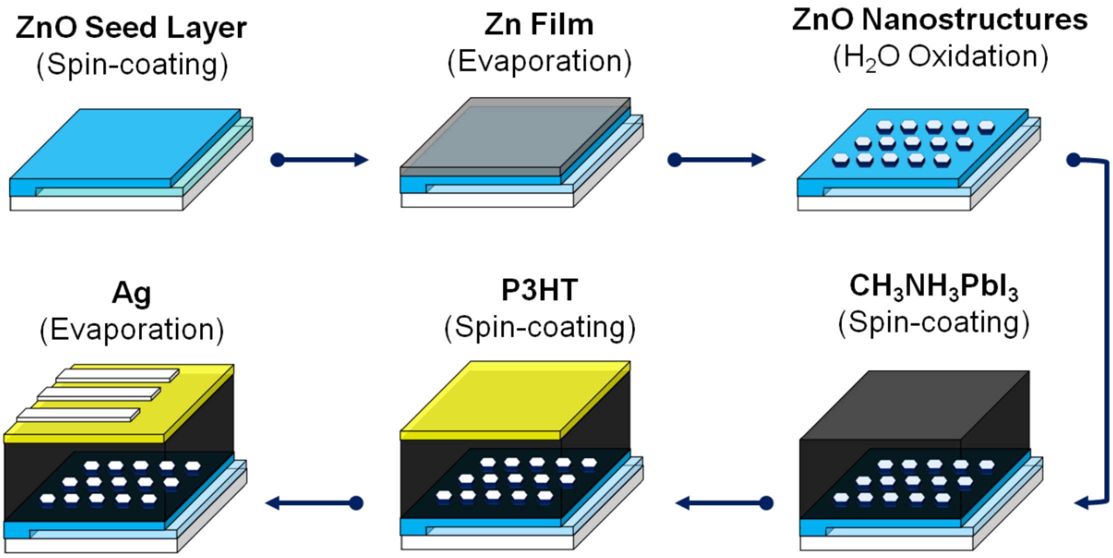

Figure 3.2 Systematic fabrication process of H_2O-oxidized ZnO-based PSC.

3.1.2.3 Device and Materials Characterization

Surface and cross-sectional morphologies were investigated by low vacuum scanning electron microscope (SEM, Hitachi SU6600). The focused ion beam-assisted (Hitachi FB2200) cross sectional SEM images and EDX analysis were observed using ultra high-resolution field emission scanning electron microscope (UHR FE-SEM, Hitachi SU9900) at

5kV. TEM and high-resolution TEM images were obtained using JEOL JEM-3100FEF at 300 kV. The XRD patterns were recorded on Rigaku X-ray diffractometer (RINT-TTR III) with CuK_α radiation (λ= 1.5418 Å). The optical transmission and absorption spectra of the films were measured on a UV-Vis spectrophotometer (JASCO V-530). PL spectra were obtained under ultraviolet excitation (λ_{ex} = 365 nm) using high-pressure mercury-vapor light source (Olympus BH2-RFL-T3) coupled with a microscope (Olympus BX51) and a CCD spectrometer (Hamamatsu PMA-12). Current-voltage (J-V) curves were recorded from a Keithley 2611B System Source Meter unit under AM 1.5G illumination (100 mW cm^{-2}, Bunko-keiki, CEP-2000RP). The external quantum efficiency (EQE) spectra were obtained under illumination of monochromatic light using the same system at an intensity of 1.25 mW cm^{-2}.

3.1.3 Results and Discussion

3.1.3.1 Influence of Growth Time on Nanostructured ZnO-based Solar Cells

Figure 3.3 shows the SEM images of the resulting NSs after H_2O oxidation of Zn thin film at different oxidation times at a constant growth temperature of 90 °C. Their corresponding cross-sectional images are shown as inset. First, ITO/glass substrates were spin-coated with a 30 nm-compact layer made up of small ZnO nanocrystals (NCs). This layer functions as the nucleation point for Zn thin film and at the same time as a compact hole-blocking layer. The Zn thin film is composed of hexagonal nanoplatelets with diameter of ~ 90 nm and thickness of ~ 100 nm, as shown in Figure 3.3(a). After 2 h of H_2O oxidation, bigger hexagonal ZnO nanoplatelets with a mean diameter of ~ 200 nm and thickness of ~ 300 nm developed. The lattice matching between Zn and ZnO crystals possibly dictated the ZnO to follow the nanoplatelet structure of Zn thin film. The significant increase in nanoplatelet diameter can be explained through Ostwald ripening process, wherein the smaller nanoparticles (NPs) seen in Figure 3.3(a) merged with the existing nanoplatelets during H_2O oxidation process (Figure 3.4(a)) [4]. The growth of rod-like structures on selected nanoplatelet regions can be noticed by increasing the reaction time to 4 h, as seen in Figure 3.3(c). At this moment, the dissolution of ZnO starts reducing the thickness of these NSs to 250 nm. When the growth time is increased to 8 h, the nanoplatelets were fully converted into pointed NRs as seen in the inset cross-sectional image of Figure 3.3(d). These NRs have a diameter of about ~ 180 nm and average length of ~ 200 nm. This preferential growth orientation of ZnO crystal along *c*-axis is due to its well-known reconstruction of high-surface energy polar (001) plane[5, 6].

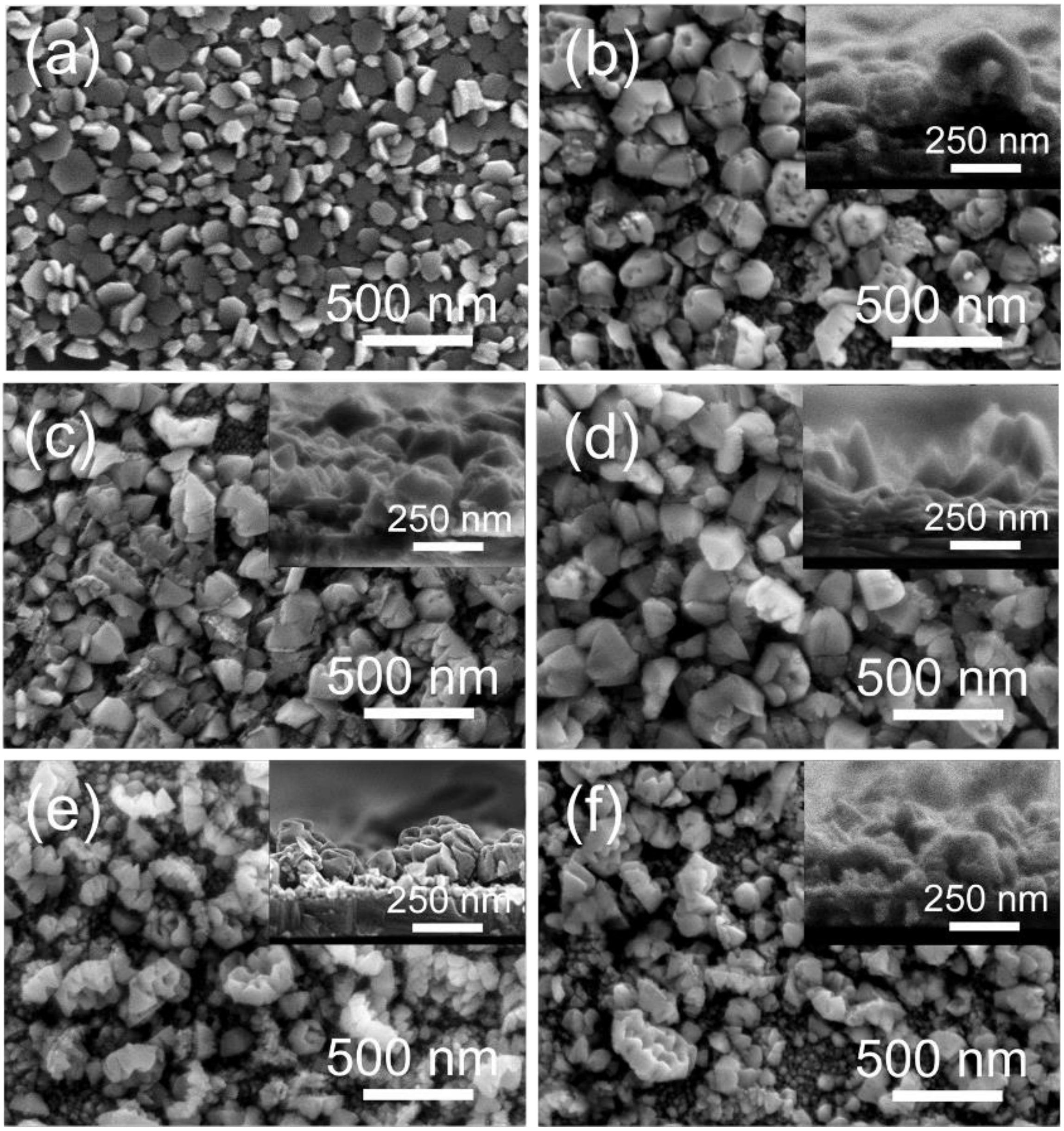

Figure 3.3 SEM images of (a) Zn thin film and ZnO NSs formed after H_2O oxidation at 90°C for (b) 2 h, (c) 4 h, (d) 8 h, (e) 16 h, and (f) 24 h. Inset images are the corresponding cross-sectional images for each oxidation time.

As ZnO molecules are generated in the solution, its negatively charged O^{2-} terminated $(00\bar{1})$ plane favorably adsorb onto the Zn^{2+} terminated (001) plane of the existing ZnO layer, driving the formation of 1D ZnO NRs (Fig. 3.4(b)). Likewise, by further extending the growth time to 16 h and 24 h, honeycomb NSs with small hollow tubes and collapsed NSs with rough surface evolved, respectively (Figure 3.3(e)-(f)). At this point, ZnO dissolution becomes the dominant reaction and natural selective etching occurs along the (001) plane of each ZnO crystal[7]. The rough surface of collapsed NSs could be attributed to the subsequent dissolution and recrystallization of ZnO crystals. It should be noted that the film thickness of both samples have reduced extensively, exposing the underlying ZnO seed layer. This phenomenon could be observed clearly for the sample oxidized for 24 h which is caused by the massive dissolution of the existing layers at a prolonged oxidation time.

A simple corrosion process can explain the growth mechanism of the formation of ZnO NSs from Zn nanoplatelets in H_2O, as shown in Figure 3.4(a). The anodic reaction takes place at the poorly oxygenated or strained regions of Zn nanoplatelets and releases Zn^{2+} ions in H_2O as expressed in Equation (1):

$$Zn_{(S)} \rightarrow Zn^{2+}_{(aq)} + 2e^- \quad (1)$$

The ultrapure H_2O used is weakly acidic to alkaline in nature (pH = 6.5-7.5). In this instance, the anodic dissolution of Zn develops sufficient energy to split H_2O as in Equation (2)[8, 9]:

$$2H_2O_{(l)} + 2e^- \rightarrow H_2 + 2OH^- \quad (2)$$

In addition, the corrosion of Zn takes place in an open system and H_2O contains dissolved oxygen that could be simultaneously reduced by consuming electrons from oxidation reaction (Equation (3)):

$$O_{2(g)} + 2H_2O_{(l)} + 4e^- \rightarrow 4OH^- \quad (3)$$

Finally, when the amount of Zn^{2+} and OH^- ions reached the supersaturation point of ZnO, hydrolysis of ZnO nuclei in the solution occurs as shown in Equation (4):

$$Zn^{2+}_{(aq)} + 2OH^-_{(aq)} \rightarrow ZnO + H_2O \quad (4)$$

(a) Corrosion of Zn nanoplatelet and conversion to ZnO

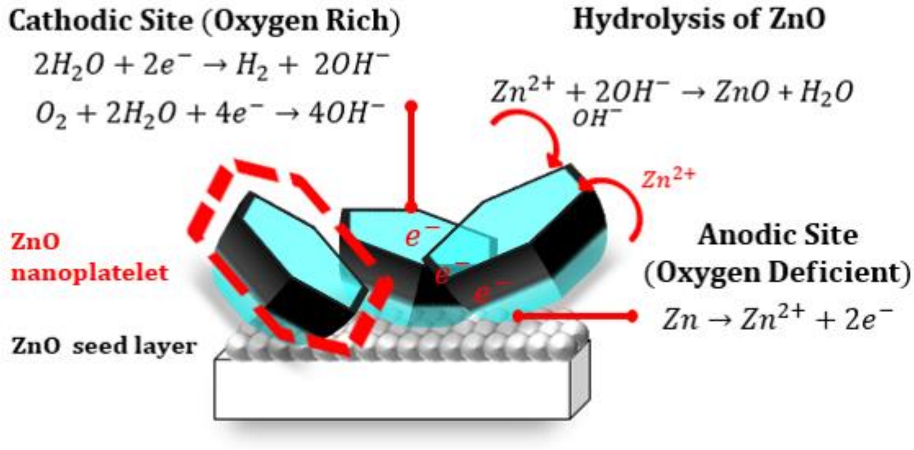

(b) Formation of pointed ZnO nanorod

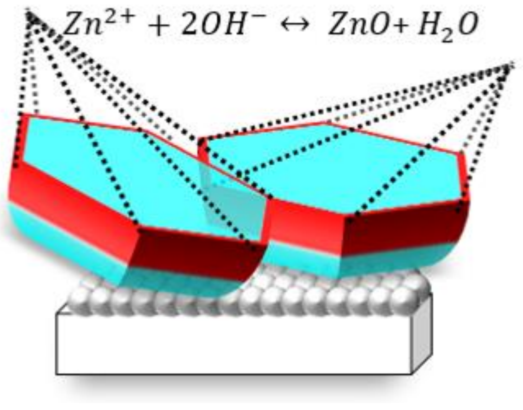

Figure 3.4 Growth mechanism for the formation of ZnO NSs from Zn thin film in H_2O.

Figure 3.5(a) shows the XRD patterns of the Zn thin films oxidized after 2, 4, 8, 16 and 24 h at a constant growth temperature of 90 °C. All the diffraction patterns exhibited four major reflection peaks on $2\theta = 31.70°$, 34.45°, 36.3°, and 47.60°, corresponding to the (100), (002), (101) and (102) planes of hexagonal wurtzite crystal structure of ZnO (See Appendix, Table 1). No impurities were detected except of the underlying ITO layer. It can be seen that the intensity of the (002) peak is gradually intensified starting from 2 h to 8 h suggesting the preferential growth of ZnO NSs along the *c*-axis, as oxidation proceeds.

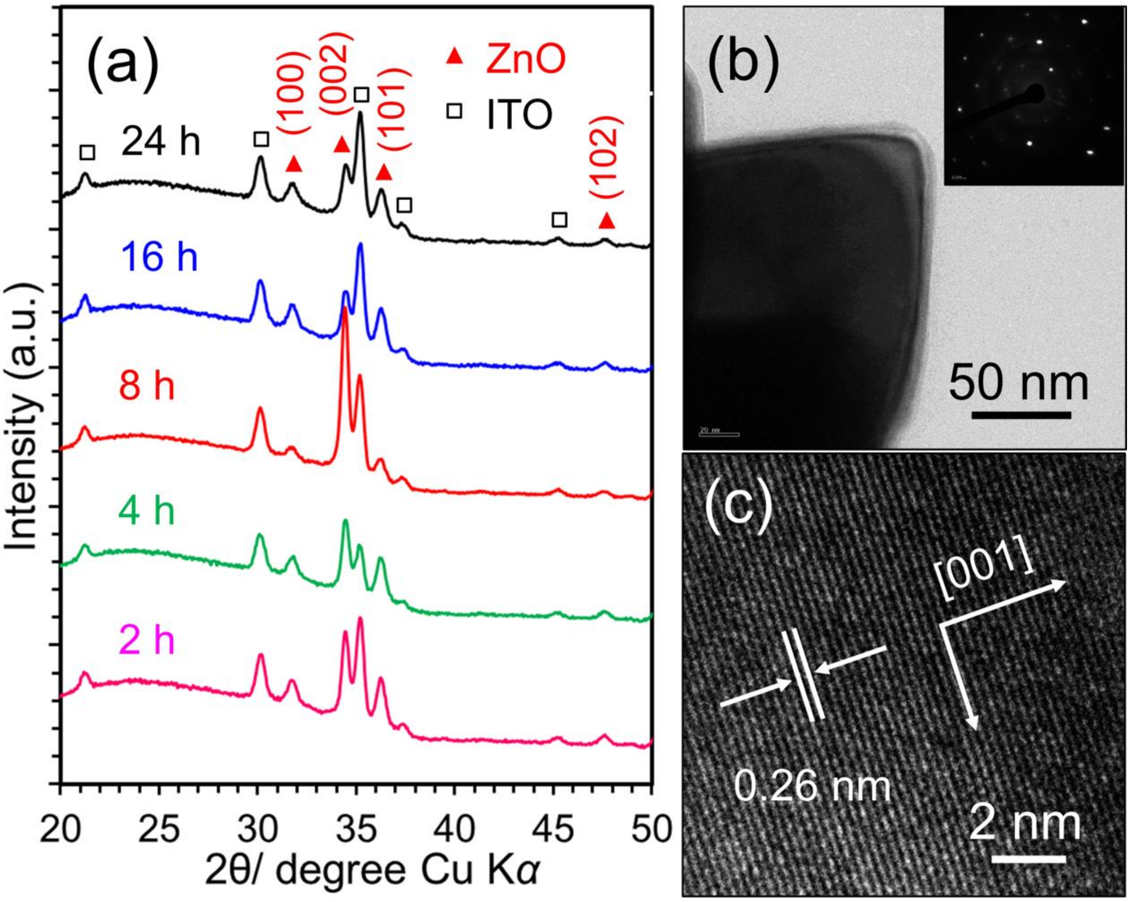

Figure 3.5 XRD patterns of the resulting ZnO NSs formed at different oxidation times. (b) TEM and SAED pattern and (c) HRTEM image of an individual pointed ZnO NR.

This was confirmed by TEM and HRTEM images of an individual pointed ZnO NR, as shown in Figure 3.5(b) and 3.5(c). The single ZnO NR has a diameter of 175 nm and possesses a high quality single-crystalline structure based on the selected area electron diffraction (SAED) pattern in the inset of Figure 3.5(b). Figure 3.5(c) demonstrates that the NR has a lattice fringe separation of 0.26 nm, which corresponds to the *d*-spacing of (001) planes. This confirms its preferential growth along the [001] direction. However, prolonged oxidation treatment of 16-24 h resulted to the decrease in the intensity of (002) peak confirming the inherent selective etching process on the (001) planes of ZnO NRs and the development of honeycomb and collapsed NSs.

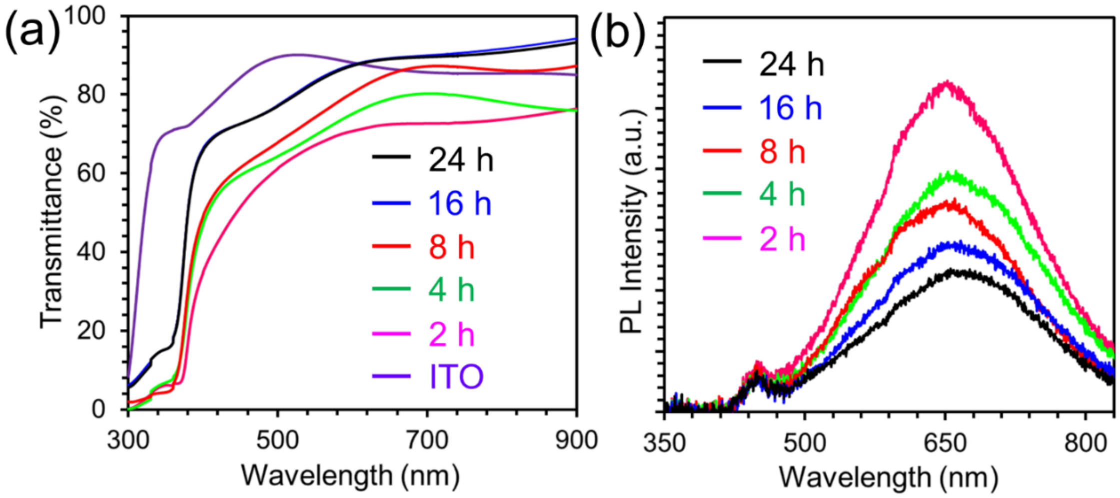

Figure 3.6 (a) Optical transmission spectra of ITO and H_2O-oxidized ZnO NSs grown at different oxidation times. (b) Photoluminescence spectra of the corresponding ZnO samples.

Optical transmission spectra of bare ITO and H_2O-oxidized ZnO NSs are presented in Figure 3.6(a). The samples displayed enhanced transmittance from 70.8% at 600 nm for the 2 h-sample to the maximum value of 87.5% for both 16 h and 24 h H_2O-oxidized samples. The lower transmittance for the platelet and rod-like NSs is associated to the Rayleigh scattering of light due to their tilted orientation that originated from the Zn thin film morphology[10]. The improved transmittance at longer reaction time is related to the reduced film thickness of the samples as described earlier. Furthermore, the 8-24 h H_2O-oxidized samples have higher transmittance than the bare ITO at wavelengths >600 nm, which could be attributed to the anti-reflection feature of nanostructured ZnO. This property of ZnO promotes sufficient light harvesting that leads to higher photocurrent generation and efficient PSCs[11]. Figure 3.6(b) shows the photoluminescence of ZnO NSs formed at different oxidation times. Under an excitation wavelength of 365 nm at room temperature, all the samples exhibited visible emissions including blue PL centered at 450 nm (2.75 eV) and orange-red peak emission centered at 650 nm (1.90 eV). Zeng et al. revealed that the blue emission originated from the radiative transition of electrons from the local interstitial zinc (Zn_i) level to the valence band[12]. On the other hand, deep level oxygen interstitials (O_i) trigger orange-red emission[13]. Both emission peaks were quenched as oxidation time is increased, indicating that the concentrations of zinc and oxygen interstitials similarly dropped as oxidation progresses. This reduction of defect concentration suggests that the carrier recombination in solar cells could be partly eliminated by utilizing nanostructured ZnO grown at an extended oxidation period.

To evaluate the preliminary charge transfer capability of H_2O-oxidized ZnO, the steady-state photoluminescence of glass/ITO/perovskite, glass/ITO/8 h-ZnO/perovskite and glass/ITO/perovskite/P3HT are presented in Figure 3.7(a). The strong PL emission peak around ~770 nm confirms the high structural quality of the perovskite film formed using fast crystallization deposition. Perovskite emission was quenched by almost ~50% when it was deposited on pointed ZnO NRs, demonstrating that H_2O-oxidized ZnO could extract electrons effectively.

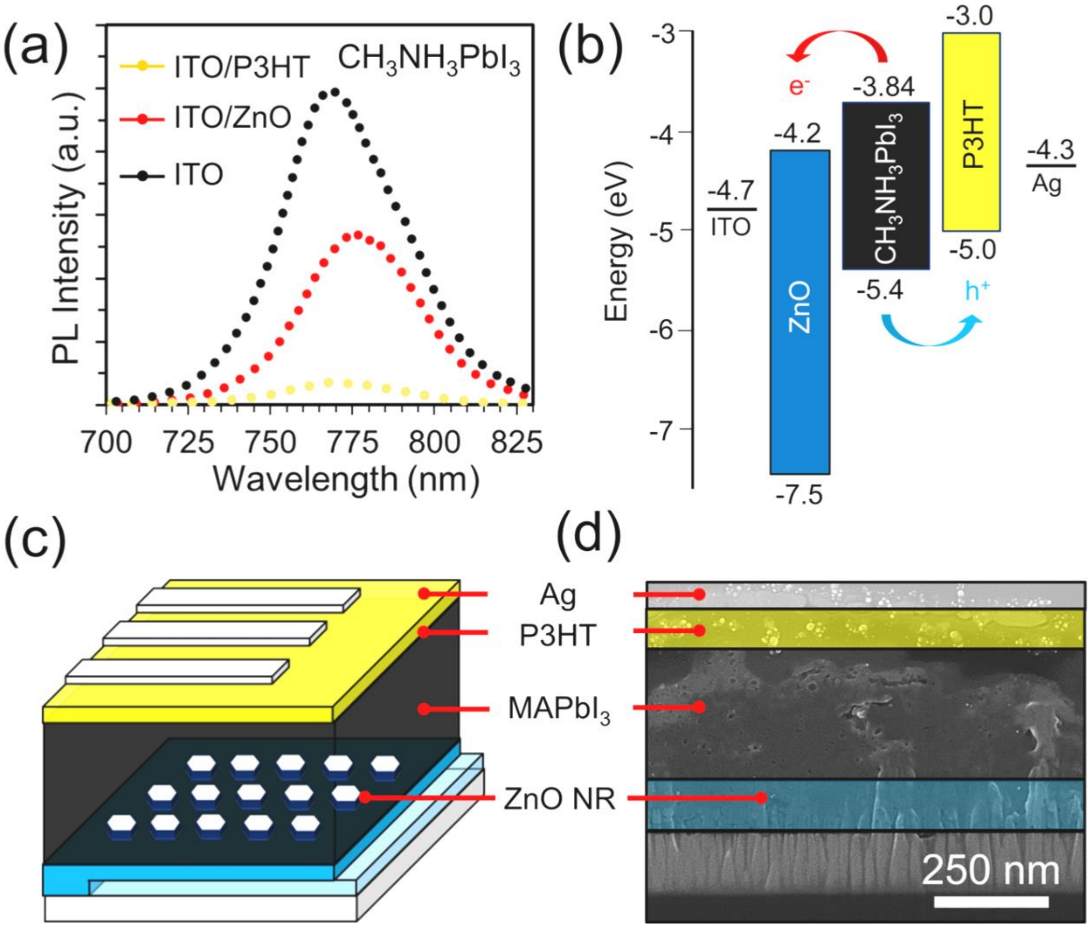

Figure 3.7 Steady-state photoluminescence spectra of perovskite films: glass/ITO/$CH_3NH_3PbI_3$ (black), glass/ITO/ZnO/$CH_3NH_3PbI_3$ (red), and glass/ITO/$CH_3NH_3PbI_3$/P3HT (yellow). (b) Energy band diagram and (c) device architecture and cross-sectional SEM images of the H_2O oxidized ZnO-based PSCs.

Perovskite/P3HT bilayer reveals a stronger PL quenching than ZnO, which is consistent with previous reports[14, 15]. The energy level diagram and schematic illustration with cross-sectional image of PSC based on H_2O-oxidized ZnO NSs are shown in Figure 3.7(b)-(d). The device consists of glass/ITO/ZnO seed layer-ZnO NSs/$CH_3NH_3PbI_3$/P3HT/Ag, wherein the H_2O-oxidized ZnO and P3HT work as the electron and hole selective layers, respectively.

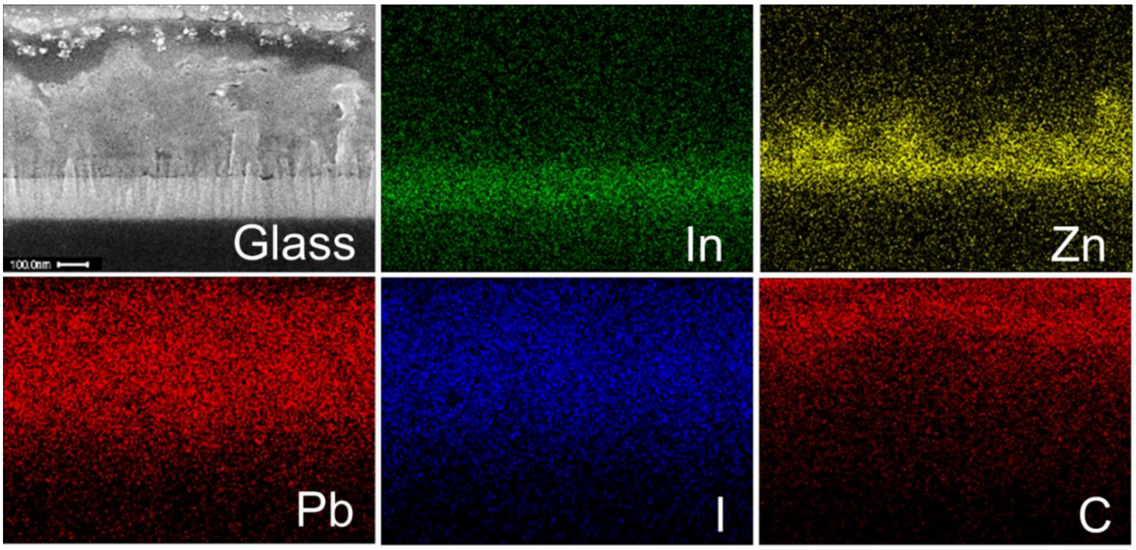

Figure 3.8 Cross-sectional elemental mapping of ZnO NR-based PSC.

Figure 3.8 shows the cross-sectional elemental mapping obtained by energy dispersive x-ray (EDX) analysis. The Zn signal follows both the shape of the compact ZnO seed layer and the pointed ZnO NRs. The Pb and I elements are seen to be well distributed three-dimensionally onto the pointed ZnO NRs. The strong C signal corresponds to the P3HT film and some to the perovskite layer. The estimated thicknesses for each layer are as follows: 200 nm-ZnO NRs, 250 nm- $CH_3NH_3PbI_3$, 100 nm-P3HT and 50 nm-Ag.

Figure 3.9(a)-(b) display the XRD pattern and absorption spectrum of the perovskite film deposited on top of pointed ZnO NRs. Most of the diffraction peaks can be indexed to the tetragonal crystal structure of $CH_3NH_3PbI_3$. A small peak at $2\theta = 12.7°$ denotes the presence of unreacted PbI_2, and peaks corresponding to ZnO and ITO/glass substrate can also be observed. Additionally, the $ZnO/CH_3NH_3PbI_3$ bilayer shows a broad range of light absorption from 350 nm to 800 nm. The calculated direct band gap of $CH_3NH_3PbI_3$ from absorption edge analysis is about 1.56 eV.

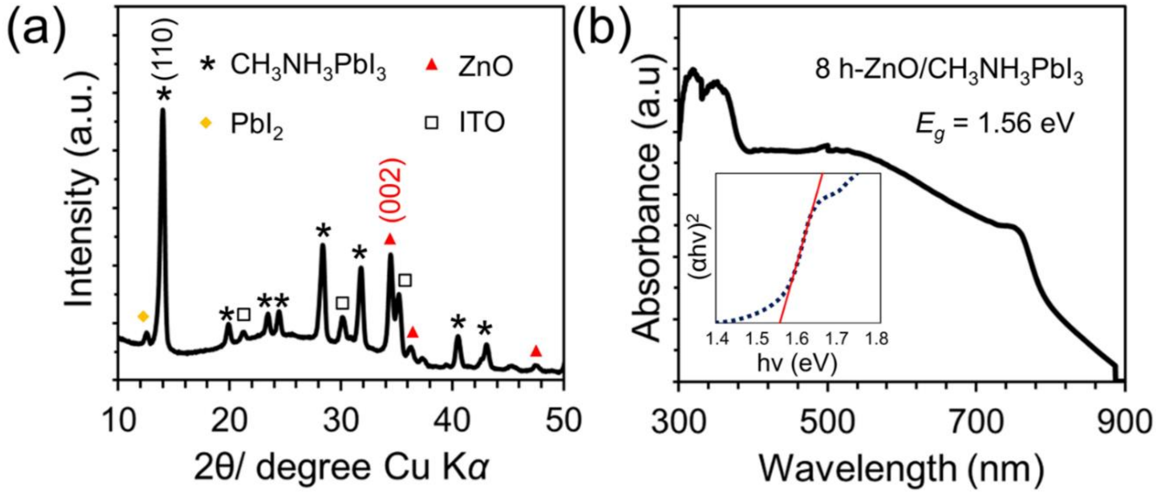

Figure 3.9 (a) XRD pattern and (b) optical absorption spectrum of perovskite film on top of 8 h-ZnO sample.

Figure 3.10 presents the photovoltaic parameters and statistical results of H_2O-oxidized ZnO-based PSCs, plotted as a function of oxidation time and scan direction. The corresponding photocurrent (J)-voltage (V) curves under simulated AM1.5G illumination (100 mW cm^{-2}) are shown in Figure 3.11. A device based on ZnO NRs, which are grown after H_2O oxidation of 8 h, exhibited the highest short circuit current density (J_{sc}) of 16.46 mA cm^{-2}, open circuit voltage (V_{oc}) of 0.82, fill factor (FF) of 44.2, maximum PCE (PCE_{max}) of 5.96% and average PCE (PCE_{ave}) of 5.28%. Based on the literature, our PCE_{max} of ≈6% is either higher or comparable with other studies that used P3HT as hole-transporting layer and ZnO (or TiO_2) as the ETL as shown in Table 3.1.

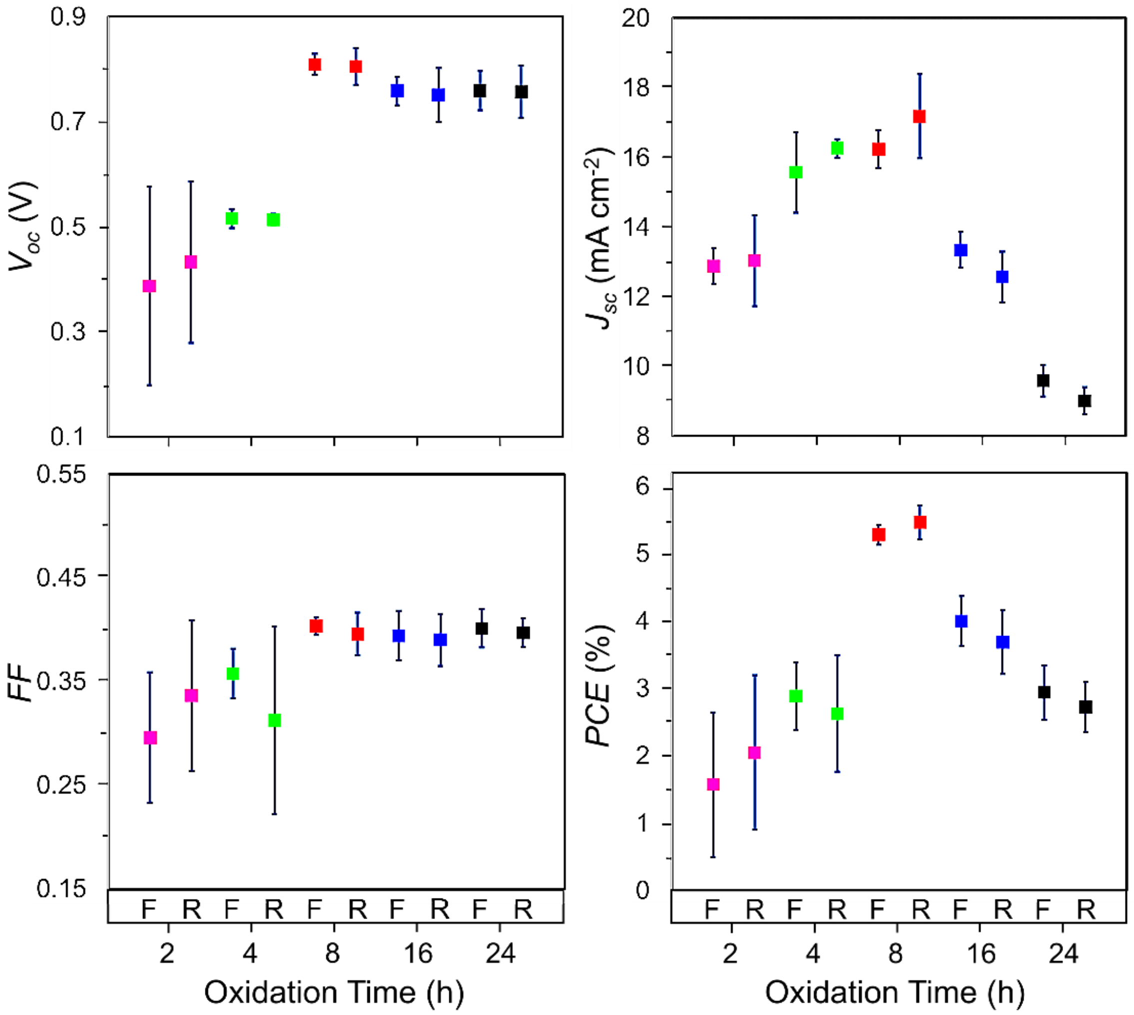

Figure 3.10 Photovoltaic parameters of PSCs based on ZnO NSs formed by H_2O oxidation of Zn thin film in H_2O. Values are plotted as a function of oxidatime time and scanning direction. (F: forward, R: reverse)

The 16 h- and 24 h-ZnO based solar cells followed with PCE_{ave} of 4.00% and 2.94%, and PCE_{max} of 4.42% and 3.40%, respectively. It can be seen that the V_{oc} dramatically increased from 0.51 V to around 0.80 V for the 4 h- to 8-24 h ZnO based devices. This could be attributed to suppressed recombination losses from the enhanced electron-transport properties within the rod and honeycomb NSs[16, 17].

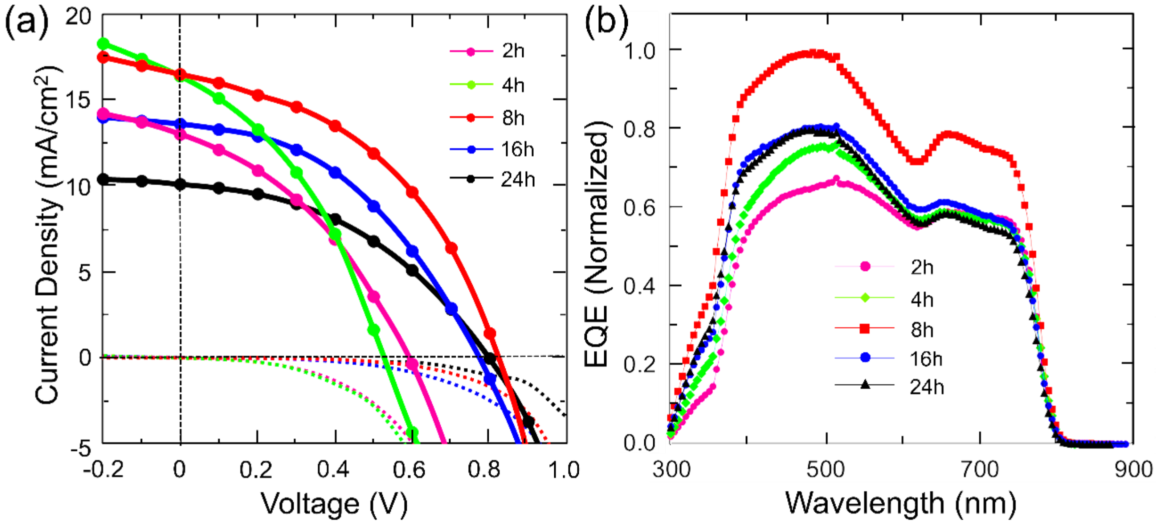

Figure 3.11 *J-V* curves and *EQE* spectra for PSCs based on H_2O-oxidized ZnO NSs grown at different oxidation times.

Table 3.1. Materials and photovoltaic parameters of PSCs based on ZnO or TiO_2 as ETLs.

ETL	Perovskite	HTL	V_{oc} (eV)	PCE_{max} (%)	Reference
ZnO NRs	$CH_3NH_3PbI_3$	P3HT	0.82	5.96	This work
ZnO NRs	$CH_3NH_3PbI_3$	P3HT	0.56	3.05	(18)
ZnO NRs/TiO_2	$CH_3NH_3PbI_3$	P3HT	0.50	3.41	(18)
TiO_2 compact film	$CH_3NH_3PbI_3$	P3HT	0.64	4.24	(19)
ZnO nanowires	$CH_3NH_3PbI_3$	P3HT	0.79	4.8	(20)
TiO_2 compact film	$CH_3NH_3PbI_3$	P3HT	0.64	5.67	(21)
TiO_2 compact film	$CH_3NH_3PbI_{3-x}Cl_x$	P3HT	0.74	6.06	(22)
ZnO film	$CH_3NH_3PbI_{3-x}Cl_x$	P3HT	1.04	6.3	(23)

The relatively low V_{oc} of the devices could be due to the utilization of P3HT as the hole-transporting layer, since it has higher HOMO level (-5.0 eV) than Spiro-MeOTAD (-5.22 eV) [24]. On the other hand, 2 h-ZnO based device exhibited the lowest PCE_{ave} of 2.04% and PCE_{max} of 2.77% followed by 4 h-ZnO based device with PCE_{ave} of 2.88% and PCE_{max} of 3.24%. The planar surface architecture of 2 h-ZnO device possibly reduced the effective interfacial area between the perovskite film and ZnO leading to more recombination and relatively low J_{sc} and FF values of 13 mA cm^{-2} and 0.30-0.35, respectively. The increase in J_{sc} values from 2 h to 8 h-ZnO based solar cell (from 13 to 18 mA cm^{-2}) can be related to the larger surface area of the nanostructured layer resulting in better perovskite infiltration, shorter path length for electron transfer and higher FF values[25, 26]. Another possible reason is the reduced recombination due to the smaller amount of defect concentration on the surface of nanostructured layers grown at longer oxidation times, as stated earlier. However, the continued oxidation up to 24 h, which led to the massive dissolution of ZnO, significantly affected the J_{sc} values and decreased them to around 9 mA cm^{-2}. The exposed ZnO seed layer in some areas of the 24 h-ZnO based device functions as the only ETL left, which is not enough for efficient electron extraction and transfer.

As shown in Figure 3.10, the 2-4 h ZnO-based devices demonstrate strong hysteresis, whereas the 8-24 h ZnO-based devices reveal weak hysteresis, as indicated by the difference in their efficiencies measured in forward and reverse scan directions. Currently, the origin of hysteresis effect is still under debate, but the dominant proposed mechanism is the ionic defect migration within the perovskite film[27-30], as illustrated in Figure 3.12. These intrinsic ionic defects include vacancies and interstitials of Pb^{2+}, I^- and $CH_3NH_3^+$ (MA^+) ions[31]. Under an applied electrical field, these charged defects travel towards their appropriate electrodes and create a p-i-n like junction within the active layer. Through forward bias, this junction arises to a complementary electronic contact for charge extraction. Conversely, this has a negative effect during reverse bias[32].This explains the higher PCE measurements recorded for most fabricated devices by forward scan direction, as shown in Figure 3.10. Moreover, De Bastiani et al.[33] established the importance of electron extraction, which mainly depends on the nature of the perovskite/transporting layer interface and thin film polarization condition.

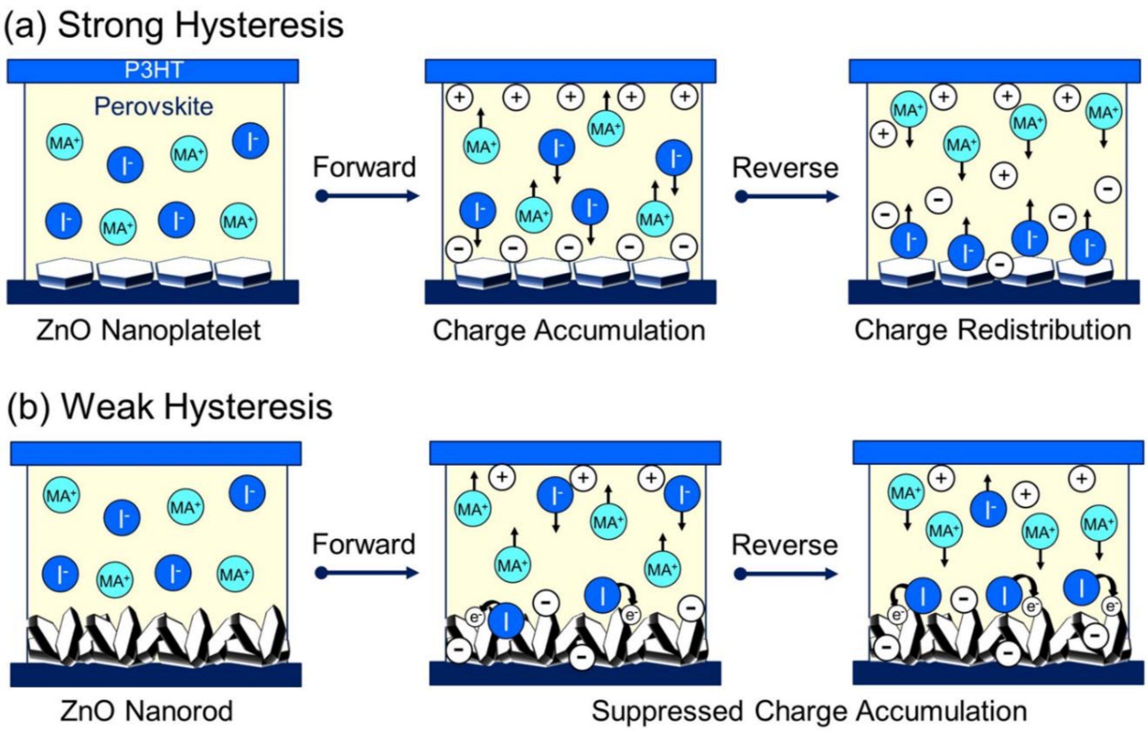

Figure 3.12 Mechanism of ion migration in PSC based on ZnO (a) nanoplatelet and (b) NR.

They found that phenyl-C61-butyric acid methylester (PCBM) layer is chemically doped through the diffusion of I^- ions from the perovskite film. This process creates electrostatic traps and hinders the iodide back diffusion/drift stabilizing the open circuit voltage and suppressing hysteresis. Herein, the perovskite layer could not easily diffuse into the large platelet-like NSs of the 2 h- and 4 h-ZnO samples (Figure 3.12(a)). This prevents ionic interaction between the ZnO and perovskite layers, allowing the ionic defects to move freely within the active layer and resulting in the observed hysteresis[34]. Consequently, as discussed in Chapter 2, I^- ions are converted to I atoms through interaction with ZnO NRs leading to weaker hysteresis (Figure 3.12(b)).

Figure 3.11(b) presents the normalized external quantum efficiencies (*EQE*) of the devices. 8 h-ZnO NR-based solar cell displayed the highest *EQE* over the entire wavelength range, which is in agreement with the trend for J_{sc} in Figure 3.10. The onset of photocurrent is around λ = 800 nm for all the devices, which is consistent with the calculated band gap of $CH_3NH_3PbI_3$ layer. Furthermore, the absorption edge of P3HT possibly caused the *EQE* peak at around λ = 660 nm[21]. The *EQE* spectra also showed a notch at around λ = 620 nm which could be due to the reduced contribution from P3HT after the formation of excitons[21, 35].

Figure 3.13 shows the preliminary stability test for 8 h-ZnO based solar cell over a 40-day period. Increasing trend over time can be observed for the V_{oc}, *FF* and *PCE* values. All devices attained their highest efficiencies after 15-20 days in vacuum at room temperature. On the 25th day of storage, hysteresis effect became almost negligible. It should be noted that the devices were completed by annealing the perovskite precursor at a moderately low temperature of 70 °C and the P3HT layer is slowly dried at room temperature for 12 h, before silver electrode deposition. As these solution-processed layers gradually dry up, enhanced interfacial area between them develops over time[36]. This was verified by examining the focused ion-beam (FIB)-assisted cross-sectional SEM images of the ZnO NR-based solar cell taken on the 1st day and 40th day after fabrication, as illustrated in Figure 3.13(e)-(f). The freshly prepared device (Figure 3.13(e)) shows that the perovskite film partially covered the NRs resulting in the formation of voids between the layers. These voids caused the high series resistance of the solar cell devices (R_s = 180-300 Ω. cm^2) leading to low fill factor values in spite of relatively high shunt resistance values ($R_{sh} = 1.0 \text{ x } 10^3 - 2.9 \text{ x } 10^3$ Ω cm^2).

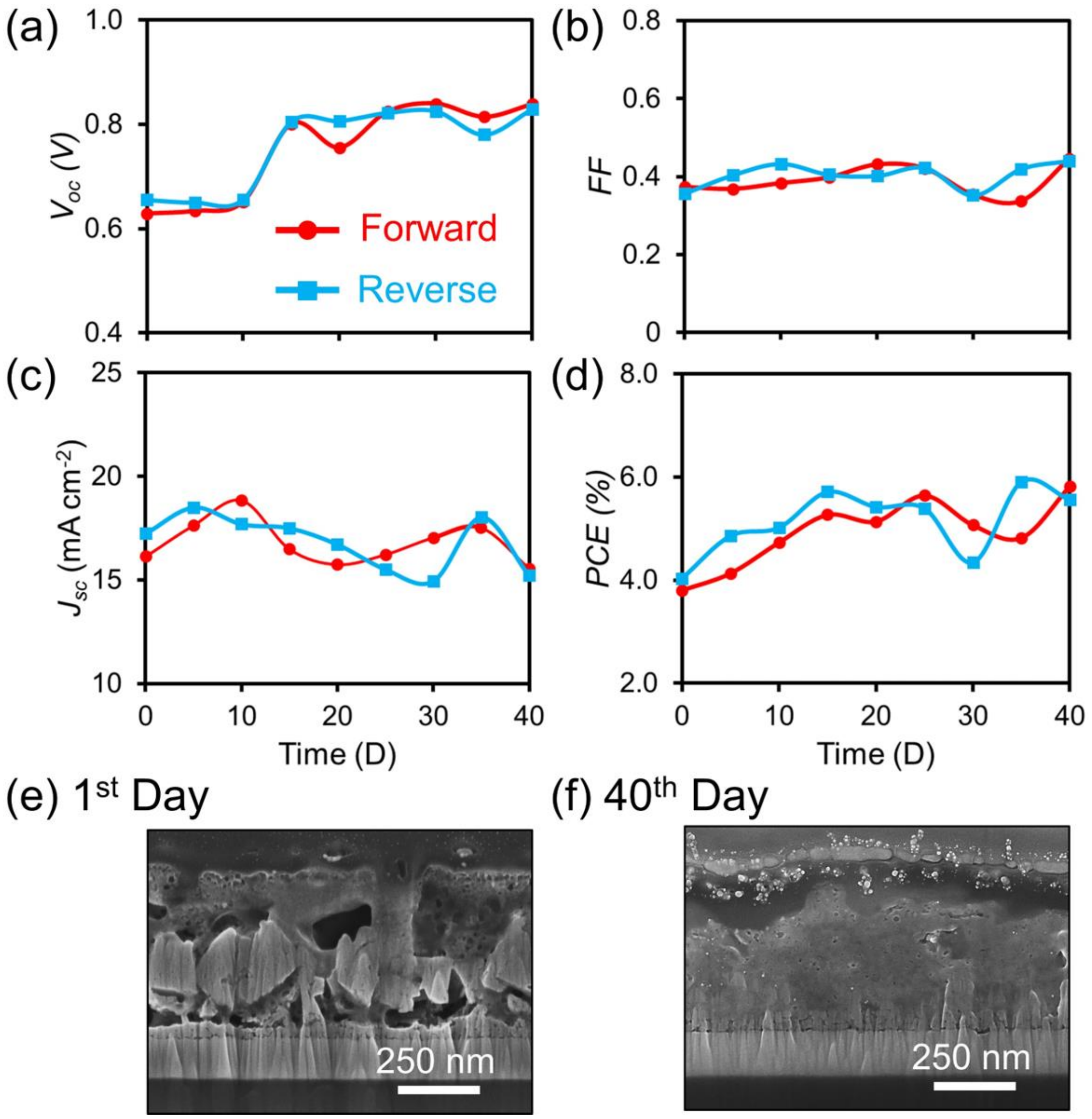

Figure 3.13 Photovoltaic parameters of ZnO NR-based PSC (Glass/ITO/ZnO NR/perovskite/P3HT/Ag) as a function of storage time in vacuum. FIB-assisted cross-sectional SEM images of ZnO NR-based PSC after (e) 1 day and (f) 40 days of fabrication.

After 40 days of storage, the pinholes can no longer be observed and the perovskite has fully permeated into the ZnO NRs (Figure 3.13(f)). However, J_{sc} values were reduced steadily after 10 days and hysteresis behavior became more evident due to the noticeable degradation of Ag electrode. This corrosion of Ag electrode is attributed to the formation of silver iodide (AgI) from the reaction of silver and iodine-containing volatile compounds

(MAI and/or HI)[37]. These volatile compounds are produced from the degradation of perovskite due to its reaction with water in air. Subsequently, the compounds could diffuse through the pinholes in P3HT and consequently corroding the Ag electrode.

3.1.3.2 Influence of Growth Temperature on Nanostructured ZnO-based Solar Cells

It has been well established that the growth temperature dictates the resulting morphologies of ZnO NSs[38, 39]. To examine the influence of oxidation temperature, the Zn thin films were immersed in H_2O under different oxidation temperatures (room temperature, 50°C, 70°C and H_2O vapor) at a constant growth time of 8 h. Figure 3.14 shows the surface morphologies and XRD patterns of the resulting ZnO NSs grown in increasing oxidation temperature. At room temperature, the platelet-like structure of Zn thin film developed into NPs with diameters ranging from 10-20 nm. It can be seen that these NPs tend to align, forming fiber-like structures parallel to the substrate, as shown in Figure 3.14(a). The formation of NPs could be possibly related to the lower kinetic energy and slower diffusion rate of ZnO molecules to form rod-like structures at a low temperature and surfactant-free system. Owing to their low kinetic energies, these NPs could not exceed the free energy barrier of the (001) plane to promote growth in axial direction and tend to aggregate to minimize their surface energies. Figure 3.14(b) shows that NRs with rounded tip having a mean diameter of 100 nm started to grow at an oxidation temperature of 50 °C. These NRs have a low aspect ratio and are composed of aggregated NPs resulting in a relatively planar surface morphology of the overall film. The visible presence of NPs indicates that their acquired energy at this given temperature (50 °C) is still not sufficient to form well-faceted rod-like structures. Increasing the growth temperature to 70 °C resulted in the development of pointed NRs, as shown in Figure 3.14(c). These NRs have a smaller mean diameter of about 115 nm but have almost the same morphology with the NRs produced at 90 °C. Figure 3.14(d) shows that when the Zn thin film was oxidized by H_2O vapor, clustered NRs and the underlying ZnO seed layer were observed. The NRs were evidently longer, with a mean diameter of about 140 nm. The exposure of the underlying seed layer could be associated with the high temperature of steam, which subsequently damages and removes the initial ZnO NSs formed during H_2O oxidation.

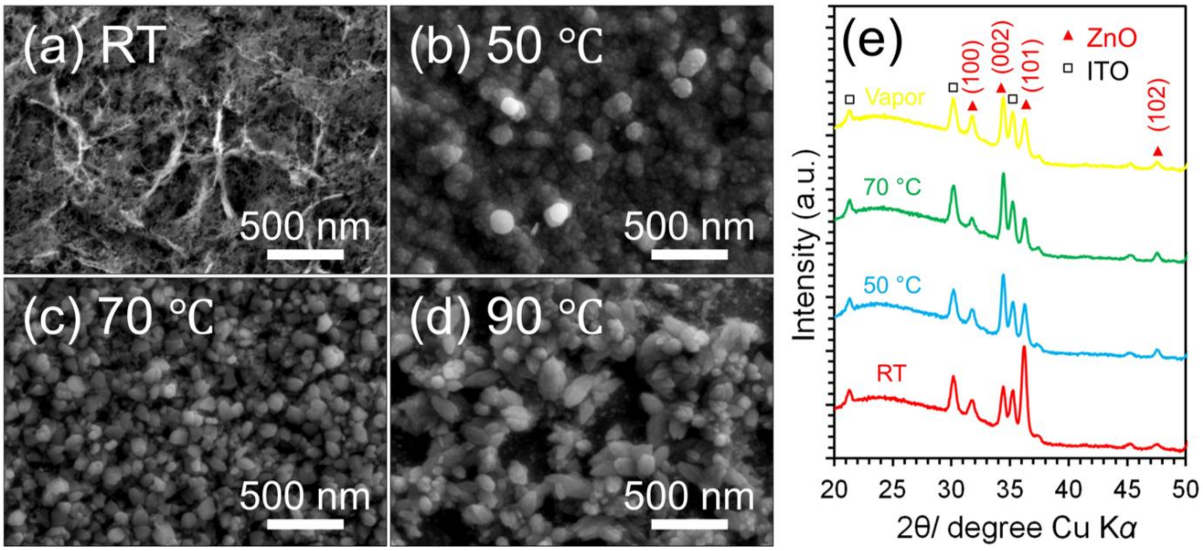

Figure 3.14 SEM images of ZnO NSs formed after H_2O oxidation for 8 h at (a) room temperature, (b) 50 °C, (c) 70 °C, and (d) H_2O vapor. (e) XRD patterns of the corresponding ZnO samples, respectively.

Figure 3.14(e) shows the XRD patterns of the Zn thin films H_2O-oxidized for 8 h at different oxidation temperatures. The diffraction peaks positioned at 2θ = 31.85°, 34.45°, 36.3°, and 47.70° can be indexed to the hexagonal wurtzite phase of ZnO. Similarly, no characteristic peaks from impurities are detected except those of the underlying ITO/glass cathode. This indicates that the Zn thin film can be fully converted to ZnO even at low H_2O temperatures. ZnO NPs formed at room temperature exhibited a stronger (101) plane intentsity. This is in agreement with Figure 3.14(a), wherein fibrous structures parallel to the substrate developed through the aggregation of NPs. The (002) plane became the dominant peak starting at 50 °C which signifies the appearance of rod-like structures. However, the intensity of ZnO peaks visibly decreased after vapor oxidation implying a reduction in ZnO concentration on the substrate. This result supports the presence of holes and exposure of underlying ZnO seed layer in Figure 3.14(d).

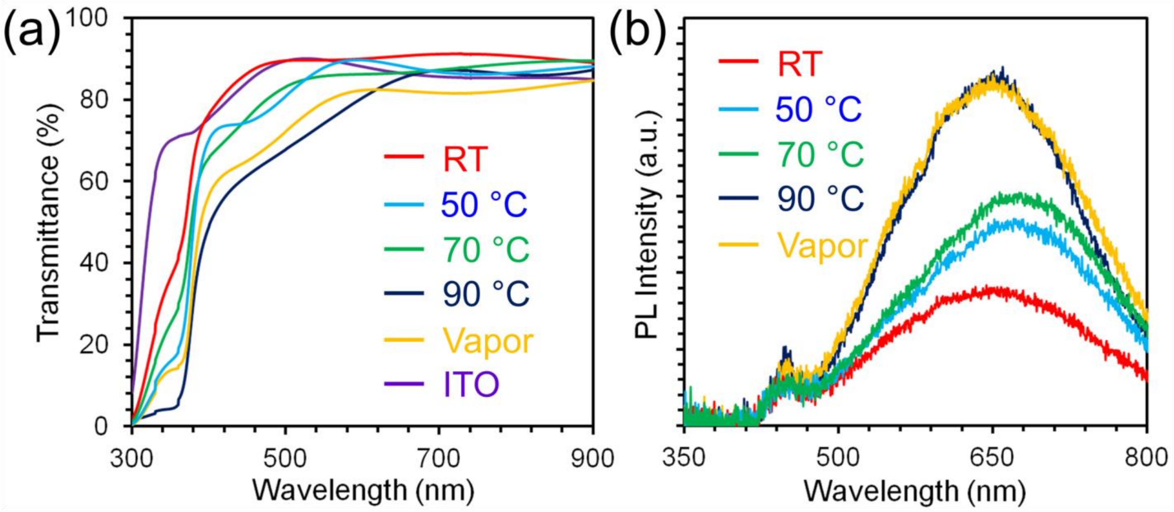

Figure 3.15 (a) Optical transmission spectra of ITO and H_2O-oxidized ZnO NSs grown at different growth temperatures. (b) Photoluminescence spectra of the corresponding ZnO samples.

Figure 3.15(a) and (b) present the optical transmission and photoluminescence spectra of H_2O-oxidized ZnO NSs grown under different temperatures for 8 h. The room temperature-oxidized sample displayed the highest transmittance of 90.6%, whereas the vapor-oxidized sample exhibited a comparable transmittance of 82.3% with the 90 °C sample (at 600 nm). All the samples demonstrate similar violet-blue and orange-red emissions but are noticeably quenched at lower temperatures, as shown in Figure 3.15(b). This could be attributed to the lower concentration of ZnO on lower temperatures. The vapor-oxidized sample also matches the PL emission intensity of the 90 °C sample.

Table 3.2 Summary of photovoltaic parameters recorded for PSCs based on nanostructured ZnO formed by H_2O oxidation at different growth temperatures for 8 h, under 1 Sun illumination (AM 1.5G, 100 mW cm^{-2})

Temperature [°C]	Scan Direction	J_{sc} [mA cm^{-2}]	Voc [eV]	*FF*	PCE_{ave} [%]	PCE_{max} [%]
RT	Forward	14.5	0.643	0.39	2.85	3.62
	Reverse	13.2	0.548	0.39	2.65	2.80
50	Forward	15.5	0.703	0.37	1.90	4.01
	Reverse	15.7	0.638	0.37	2.45	3.75
70	Forward	16.4	0.674	0.37	3.64	4.11
	Reverse	14.8	0.637	0.39	3.29	3.64
90	Forward	15.8	0.832	0.41	5.28	5.96
	Reverse	18.0	0.780	0.42	5.46	5.91
Vapor	Forward	16.1	0.815	0.38	3.73	5.03
	Reverse	15.8	0.614	0.36	3.30	3.50

Table 3.2 summarizes the photovoltaic parameters for both scanning directions and statistical results of PSCs based on ZnO NSs grown at different growth temperature. Figure 3.16(a) and (b) present the photocurrent (*J*)-voltage (*V*) curves and EQE spectra of the corresponding solar cells. The solar cell device based on ZnO NRs grown at 90 °C still has the highest maximum efficiency, followed by the vapor oxidized ZnO-based device with PCE_{max} of 5.03% and PCE_{ave} of 3.73%, and 70°C-ZnO based device with PCE_{max} of 4.11% and PCE_{ave} of 3.64%. These three devices are based on rod-like structures, which are established to be advantageous for better perovskite permeation and interfacial area resulting in higher J_{sc} values (Table 3.1). The 50 °C-ZnO based solar cell showed the strongest hysteresis and presented the lowest PCE_{ave} of 2.45% with a PCE_{max} of 4.01%. This low performance of 50 °C-ZnO based solar cell could likewise be attributed to its planar surface configuration, preventing the perovskite layer to diffuse into the ZnO film.

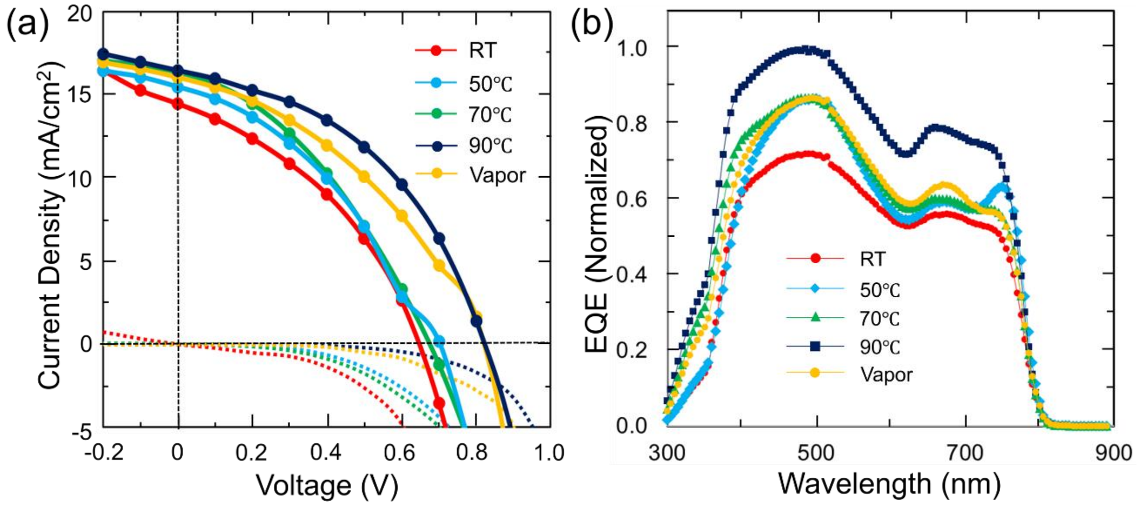

Figure 3.16 *J-V* curves and *EQE* spectra for PSCs based on H_2O-oxidized ZnO NSs grown at different oxidation times.

Consequently, this leads to charge carrier recombination and relatively low average J_{sc} and V_{oc} values of 13 mA cm^{-2} and 0.375-0.475 V, respectively. This result further confirms that the electrical contact between the perovskite and ETL is critical for high performance and suppression of hysteresis. Interestingly, the PSC based on fibrous ZnO grown at room temperature displayed a respectable PCE_{ave} of 2.85% and PCE_{max} of 3.62%. This solar cell demonstrates a higher average V_{oc} of 0.60 V but lower average J_{sc} of 12.65 mA cm^{-2} compared to the 50 °C-ZnO based solar cell. The higher V_{oc} is possibly due to the penetration of perovskite film between the spaces of fiber-like structures, whereas the lower J_{sc} values could be due to the discontinuity of the same structures normal to the substrate leading to a higher recombination before carrier collection to the cathode. Finally, the J_{sc} trend from the EQE spectra of the solar cells (Figure 316(b)), based on nanostructured ZnO grown at different oxidation temperature, confirms the J_{sc} trend observed in Table 3.1. The 90 °C-ZnO based solar cell still exhibits the highest EQE over the entire wavelength range followed by

50 °C-, 70 °C-, and vapor-oxidized ZnO based devices. Thus, based on these results we found that the optimum oxidation temperature for H_2O oxidation is 90 °C.

3.2 Effect of pH on H_2O-Oxidized Nanostructured ZnO Films for Bi-Based Pb-Free $(CH_3NH_3)_3Bi_2I_9$ Perovskite Solar Cells

3.2.1 Introduction

Pb-based PCSs are still facing several issues despite their fast development including the inherent toxicity of Pb and their instability under ambient conditions. Alternative materials like Sn and Ge were reported to replace Pb[40-43]. The record efficiency of $MASnI_3$-based (MA: methyl ammonium) solar cells has already exceeded 6%[44] however, Sn(II) is readily oxidized to Sn(IV) upon air exposure which makes it unstable. Thus, Sn-based PSCs are usually fabricated in a nitrogen atmosphere, $MASnI_3$ especially by hermetic encapsulation to avoid contact with oxygen. Ge-based perovskite has poor ability of forming homogenous films and Ge analogs can be more easily oxidized than Sn^{2+}. Ge based-PSCs were first reported by Krishnamoorthy with *PCE* of 0.11% and 0.20% for solar cells based on $CsGeI_3$ and $MAGeI_3$ as absorber layers, respectively[45]. Other reported Pb-free PSCs such as Cu and Sb-based ones have lower performances than Sn-based devices[46, 47].

Recently, Bi-based perovskites have gained much interest as the next alternative for Pb halide perovskites. Bi is a promising replacement for Pb due to its non-toxic nature, identical $6s^2$ electronic configuration and ionic radius as Pb[48, 49]. Up to now, solar cells based on $(CH_3NH_3)_3Bi_2I_9$ as light absorbers have already reached a world record hysteresis-free *PCE* of 3.17%, wherein a two-step vapor-assisted solution process (VASP) technique was applied to react films of BiI_3 with MAI vapors to form the perovskite[50]. This development and most importantly their non-toxicity and high stability in air render these solar cells as a viable alternative for next-generation photovoltaics. All previous studies about Bi-based PSCs are relying on TiO_2 as the ETL. To the best of our knowledge, no study on Bi-based PSCs using nanostructured ZnO as ETL has been reported so far.

In the previous section, we presented a novel route of fabricating nanostructured ZnO films via a strategic low-temperature H_2O oxidation of Zn thin films and showed their capability as an ETL for Pb-based PSCs. The H_2O oxidation method offers a simple, low-temperature ($T \leq 100$ °C), sustainable and cost-effective way of producing diverse ZnO surface architectures. Furthermore, potential contamination due to unwanted impurities is avoided since only deionized H_2O is used to initiate the NS growth. We have successfully fabricated different nanostructured ZnO films from platelets to rods, honeycomb structures and fibrous wires composed of particles by changing the oxidation time and temperature. Additionally, it has been reported that the solution pH considerably affects the ensuing morphologies and properties of ZnO NSs. Devabharathi et al. reported a precipitation method to produce ZnO NCs at different pH values[51]. Better crystallinity was observed for ZnO NCs produced at higher pH which led to an enhanced photovoltaic performance of dye-sensitized solar cells. Another study explored the effect of pH on various ZnO NSs grown by hydrothermal method[52]. All the ZnO NSs exhibited violet emission unlocking their application in LEDs. Zhang et al. also established that pH was essential to consistently prepare flower-like ZnO NPs for biological fluorescent imaging[53]. Herein, novel nanostructured ZnO films were designed by controlling the pH of H_2O[54] and were subsequently utilized as an ETL for Bi-based PSCs for the first time.

3.2.2 Experimental

3.2.2.1 Formation of ZnO NRs by pH-controlled H_2O oxidation

Flourine-doped tin oxide (FTO)-glass substrates were thoroughly cleaned with DMSO, acetone and isopropanol for 5 min each, washed with DI H_2O, and dried under N_2 flow. A 15 nm Ti film was then deposited on cleaned FTO-glass substrates and annealed at 500 °C for 1 h in air to form a compact TiO_2 layer (c-TiO_2). After cooling down, 50, 80, and 100 nm Zn were deposited on top of the compact layer via e-beam evaporation, and the samples were subsequently immersed in H_2O at 90 °C. The influence of pH value on the growth of ZnO NSs was examined by adjusting the solution pH from 4 to 11 through addition of HCl and NaOH. After H_2O oxidation, the samples were washed with DI H_2O and annealed at 350 °C for 1 h in air.

3.2.2.2 Solar Cell Assembly

0.20 M perovskite precursor solution was prepared by mixing 235.9 mg of BiI_3 and 95.4 mg of CH_3NH_3I in 1 ml anhydrous DMF. Then, 50 µL of this solution was spin-coated on top of ZnO films at 5000 rpm for 30 s and annealed at 100 °C for 10 min. For the preparation of HTL, 83.3 mg Spiro-MeOTAD, 11.13 mg 4-tert-butylpiridine and 7.5mg lithium bis-(trifluoromethyl sulphonyl) imide were dissolved in 1ml chlorobenzene: acetonitrile (10: 1) solution. Then, 50 µL of this solution was spin-coated on top of perovskite layers at 2000 rpm for 30 s to form the HTL. Finally, 80 nm of Au was evaporated on the samples to form an electrode. The solar cells were masked with a metal aperture of 0.19 cm^2 to define the active area.

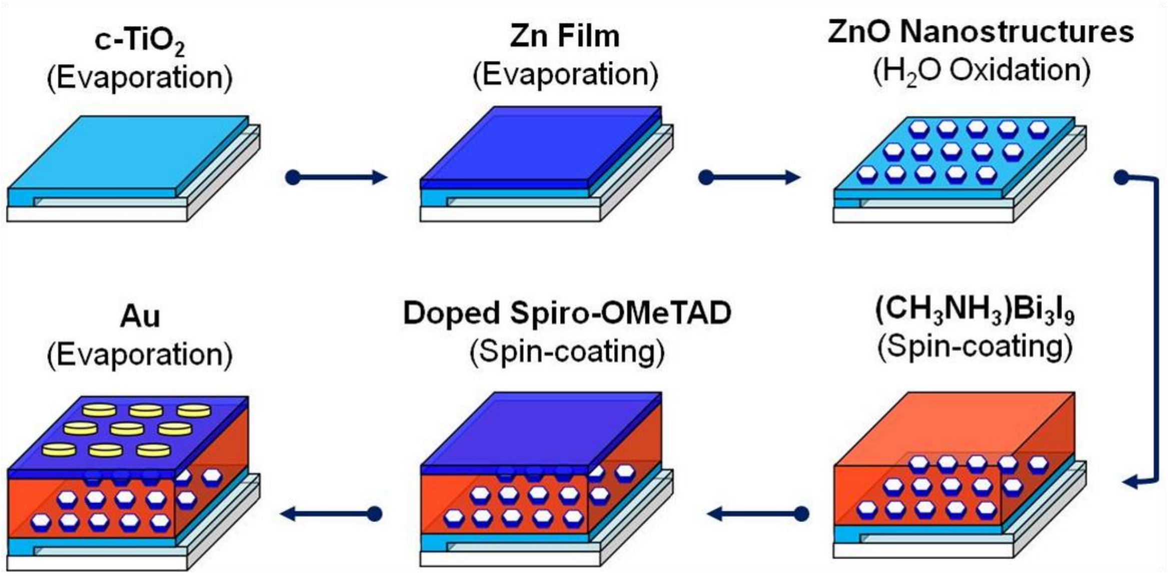

Figure 3.17 Systematic fabrication process of H_2O-oxidized ZnO NRs-based PSC.

3.2.2.2 Device and Materials Characterization

The top-view, cross-sectional morphology observations and energy-dispersive X-ray spectroscopy (EDX) were taken through a scanning electron microscope (SEM, ZEISS Sigma and SU6600 equipped with an EDX system). High-resolution transmission electron microscopy (TEM) images, selected-area electron diffraction (SAED) patterns, and electron energy loss spectroscopy (EELS) elemental mappings were obtained using JEOL JEM-3100FEF operating at 300 kV. The roughness of the ZnO films was analyzed by an atomic force microscope (AFM, Seiko SPA-400 using Olympus SI-DF20 Probe) in tapping mode[55]. AFM images were taken in air by scanning an area of 5 x 5 µm with a scan rate of 0.70 Hz. The thickness of each ZnO film was measured by a profilometer (Tencor P-10). Raman scattering measurement was performed at room temperature using a Raman Spectrometer

(JASCO NRS-4100). The crystallinity and phase purity of all samples were examined using a Rigaku X-ray diffractometer (RINT-TTR III) with CuK_{α} radiation (λ= 1.5418 Å). A UV-Vis spectrophotometer (JASCO V-530) was used to acquire the transmission spectra. Photoluminescence spectra were measured under ultraviolet excitation (λ_{ex} = 365 nm) using a high-pressure mercury-vapor light source (Olympus BH2-RFL-T3) coupled with a microscope (Olympus BX51) and a CCD spectrometer (Hamamatsu PMA-12). The surface chemistry of the ZnO films was further investigated using X-ray photoelectron spectroscopy (XPS, PHI5000 VersaProbeII, ULVAC-PHI) at room temperature with Al-Kα radiation (1486.6 eV). Charging effects on the binding energies were corrected with respect to the C 1s peak (284.6 eV). The photovoltaic properties of the devices were measured using a Keithley 2400 Source Meter unit under AM 1.5G simulated sunlight with a power density of 100 mW cm^{-2} (Newport Solar Simulator).

3.2.3 Results and Discussion

Figure 3.18(a) shows the SEM and AFM images of compact TiO_2 (c-TiO_2) layer formed after annealing of Ti film at 500 °C. The c-TiO_2 has a smooth surface with a thickness of ~15 nm and root-mean-square (RMS) roughness of 4.14 nm. Additionally, this layer mainly functions as a nucleation point for the Zn thin film. As shown in Figure 3.18(b), an e-beam-deposited Zn thin film is composed of hexagonal nanoplatelets with a mean diameter of ~ 100 nm and a thickness of ~ 80 nm.

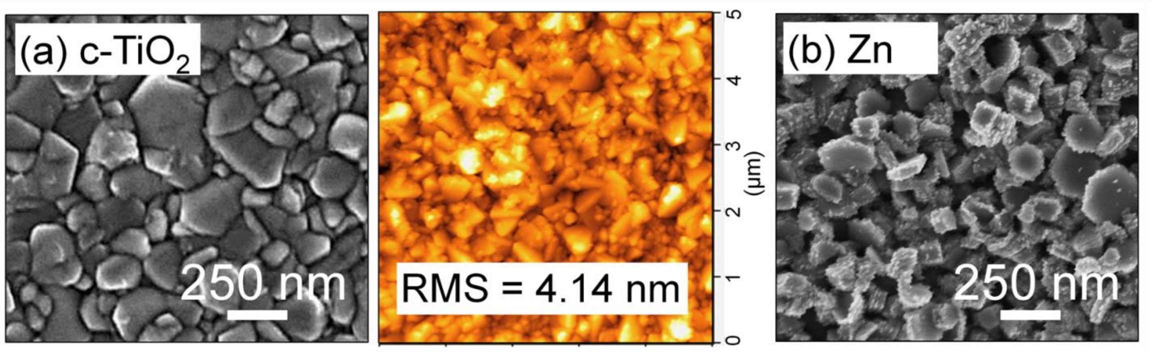

Figure 3.18 SEM and AFM images of (a) compact TiO_2 layer and (b) SEM image of e-beam deposited Zn thin film.

Figure 3.19 shows the proposed growth mechanism for the nanostructured ZnO during pH-controlled H_2O oxidation, which is primarily governed by a number of electrochemical reactions. First, the anodic corrosion of Zn nanoplatelets (Eqn. (1)) in the presence of H_2O and dissolved oxygen occurs, as shown in Figure 3.20(a).

$$Zn_{(S)} \rightarrow Zn^{2+}_{(aq)} + 2e^- \qquad (1)$$

$$2H_2O_{(l)} + 2e^- \rightarrow H_2 + 2OH^- \qquad (2)$$

$$O_{2(g)} + 2H_2O_{(l)} + 4e^- \rightarrow 4OH^- \quad (3)$$

The OH^- ions from NaOH and eqn. 2 and 3 react with Zn^{2+} ions to form ZnO crystals through hydrolysis (Eqn. (4)).

$$Zn^{2+}_{(aq)} + 2OH^-_{(aq)} \rightarrow ZnO + H_2O \quad (4)$$

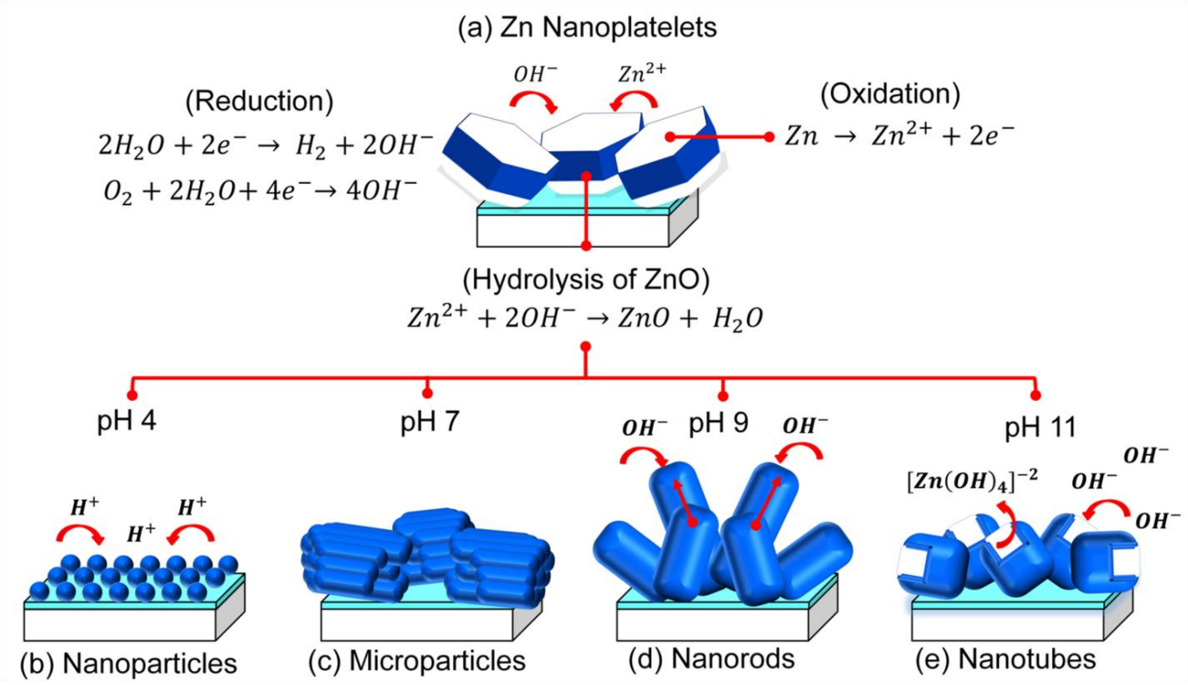

Figure 3.19 Growth mechanisms of ZnO NSs via pH-controlled H_2O oxidation from (a) Zn nanoplatelets to (b) ZnO NPs, (c) MPs, (d) columnar NRs, and (e) NTs.

It is well-established that the crystal formation in solution starts with nucleation and followed by crystal growth[56]. In H_2O oxidation, the concentration of either Zn^{2+} or OH^- ions regulate the nucleation of ZnO crystals, which function as nuclei for ZnO NSs. These nuclei then create larger ZnO clusters, which will later aggregate to reduce their interfacial free energy. When the size of a ZnO cluster reaches a certain threshold, the existing ZnO crystals in H_2O can now be adsorbed onto the crystal facets. This leads to a preferred growth orientation of each NS depending on a given set of growth conditions. Thus, it can be inferred that the concentration of OH^- ions functions as a kinetic factor for the growth of H_2O-oxidized ZnO NSs.

To check this assumption, the effect of solution pH value on the resulting NSs after H_2O oxidation of the Zn thin films was investigated at a constant growth temperature of 90 °C and for an immersion time of 8 h, as shown in SEM and AFM images in Figure 3.20. The pH value of H_2O was adjusted to either acidic or basic values at room temperature by addition of either HCl solution or NaOH pellets, respectively. Upon immersion in acidic H_2O, the Zn thin film was dissolved instantaneously and NPs with a mean diameter of 10 nm and thickness of about 20 nm were obtained, as illustrated in Figure 3.20(a). The roughness of the seeded FTO increased to 4.90 nm and was covered by NPs. The addition of H^+ ions from HCl neutralized most of the OH^- ions in H_2O (Eqn. (2) and (3)), which limited the production and growth of ZnO. This led to the development of NPs, as shown in Figure 3.19(b).

Moreover, densely packed microparticles (MPs) with a mean diameter of 0.18 µm evolved from hexagonal platelets at normal pH 7, as shown in Figure 3.20(b). This nanostructured film has a thickness of 80 nm and surface roughness of 5.94 nm. A closer inspection of these MPs shows that they are composed of smaller NRs with a mean diameter of 40 nm. Additionally, the NRs can be seen lying parallel to the substrate.

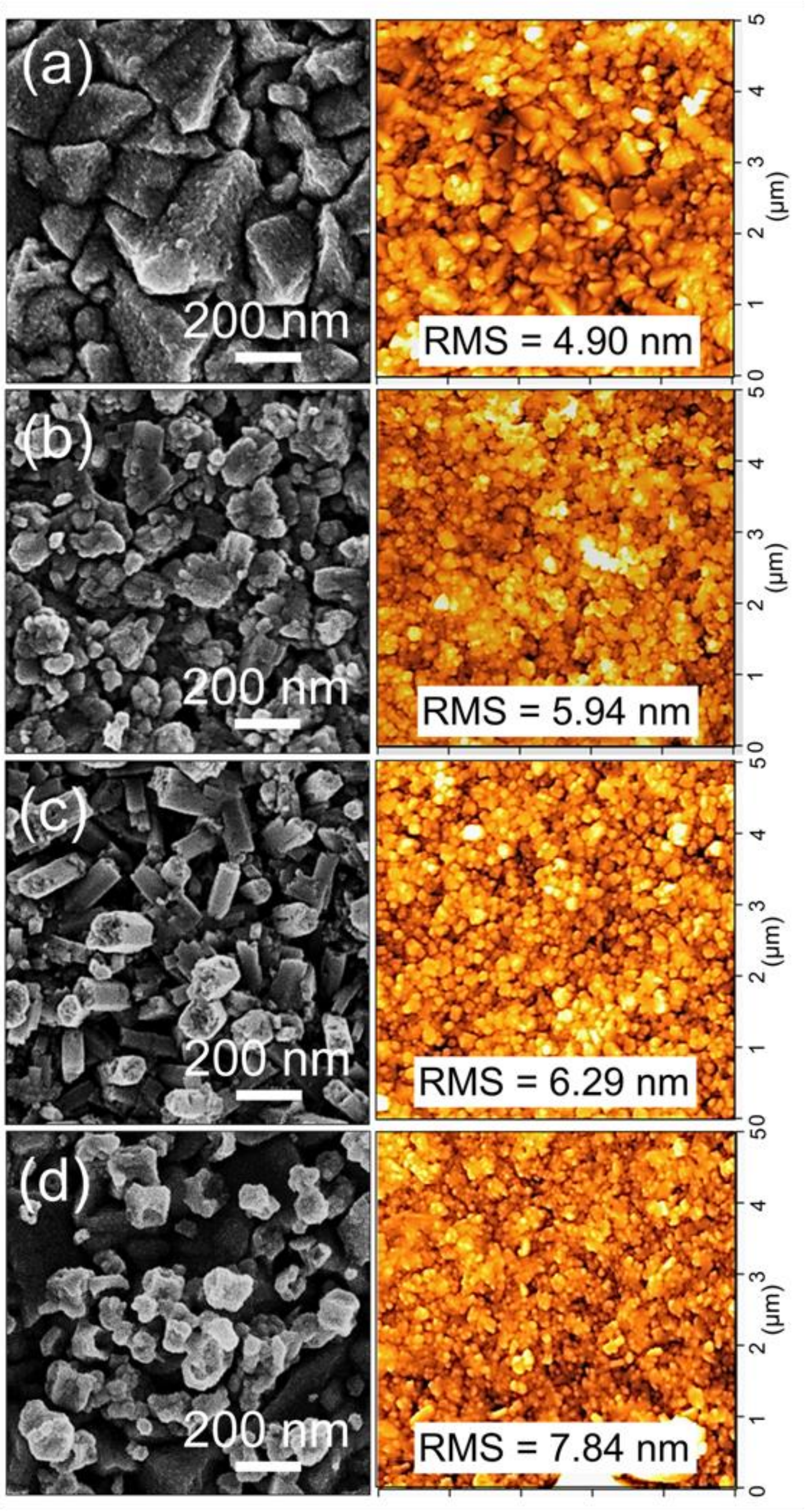

Figure 3.20 SEM (left) and AFM (right) images of ZnO NSs formed after H_2O oxidation for 8 h at 90 °C under different pH conditions: (a) pH 4, (b) pH 7, (c) pH 9 and (d) pH 11.

This aggregation of smaller NRs into larger MPs could be due to widely known Ostwald ripening process[57]. On the other hand, increasing the pH value of H_2O to 9 initiated the growth of larger columnar NRs with RMS roughness of 6.29 nm, as seen in Figure 3.20(c). These NRs have flat basal planes with a mean diameter of 95 nm and increased thickness of 135 nm. It is well known that the reconstruction of the high surface energy polar (001) plane of ZnO causes this anisotropic growth along their c-axis. Furthermore, the O^{2-}-terminated $(00\bar{1})$ planes of ZnO molecules in H_2O diffuse towards onto the Zn^{2+}-terminated (001) plane of the existing ZnO layer on the substrate, driving the generation of columnar NRs[58]. The evolution of longer NRs could be attributed to the additional OH^- ions provided to the system, as demonstrated in Figure 3.20(d). Finally, nanotubes (NTs) with a mean outer diameter of 90 nm and inner diameter of 50 nm were formed at pH 11 (Figure 3.20(d)). It also has the highest surface roughness of 7.84 nm, owing to its larger surface area with an average thickness of 90 nm. The excess OH^- ions are favorably adsorbed to (001) planes of the existing ZnO NRs due to electrostatic adherence. Consequently, the defects on these ZnO planes further react with OH^- ions to produce soluble hydroxyl complex such as zincate ions $[Zn(OH)_4]^{2-}$, as expressed in eqn. 5[59]:

$$ZnO_{(s)} + OH^- + H_2O \rightarrow [Zn(OH)_4]^{-2} \quad (5)$$

This selective dissolution of the ZnO crystal along its c-axis resulted in the formation of NTs, as illustrated in Figure 3.19(e).

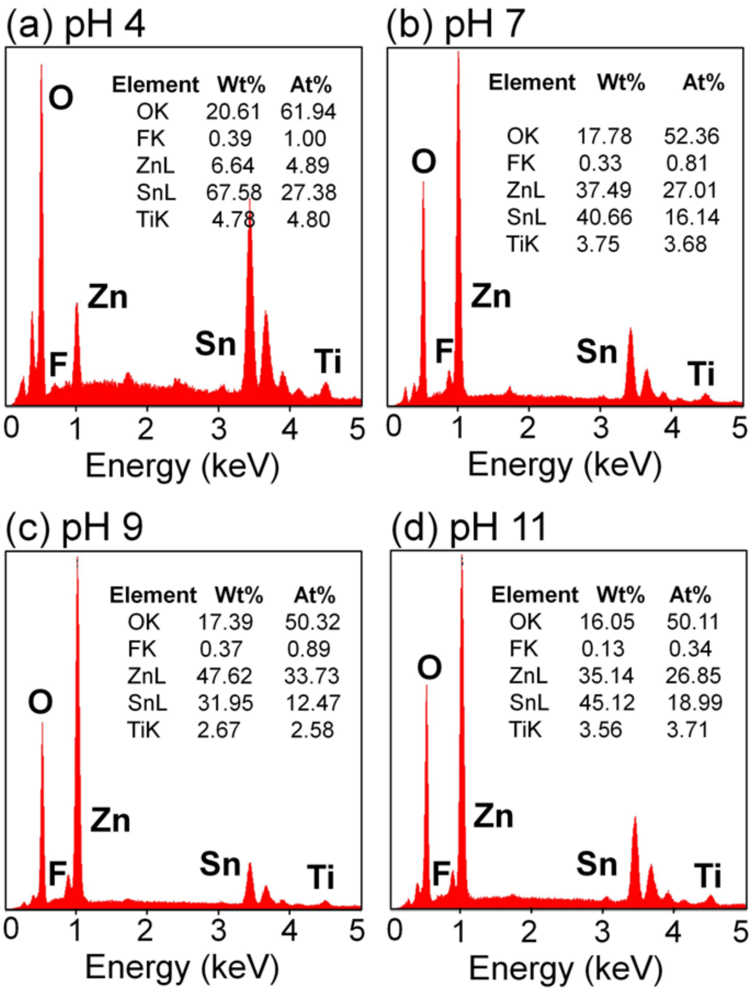

Figure 3.21 EDX analyses of ZnO NSs formed after H_2O oxidation for 8 h at 90 °C under different pH conditions: (a) pH 4, (b) pH 7, (c) pH 9 and (d) pH 11.

The chemical compositions of all the samples were verified by performing EDX analysis, as shown in Figure 3.21. All EDX patterns indicated the presence of Zn and O elements, as well as Ti, Sn and F elements from c-TiO_2 and FTO substrate, respectively. The trend of atomic weight percent of Zn element is in agreement with the measured thicknesses of each nanostructured ZnO film. These data confirm the high-purity of the ZnO NSs fabricated by H_2O oxidation.

The phase composition and crystallinity of all the samples were investigated by XRD analyses. Figure 3.22(a) shows the XRD patterns of c-TiO_2 and the nanostructured ZnO films obtained after H_2O oxidation under different pH conditions. The nanostructured films obtained at pH 7, 9, and 11 showed diffraction peaks at 2θ = 31.7°, 34.4°, 36.2°, and 47.6°, corresponding to the (100), (002), (101) and (102) planes of the wurtzite (*P6₃mc*) crystal structure of ZnO, respectively[60, 61].

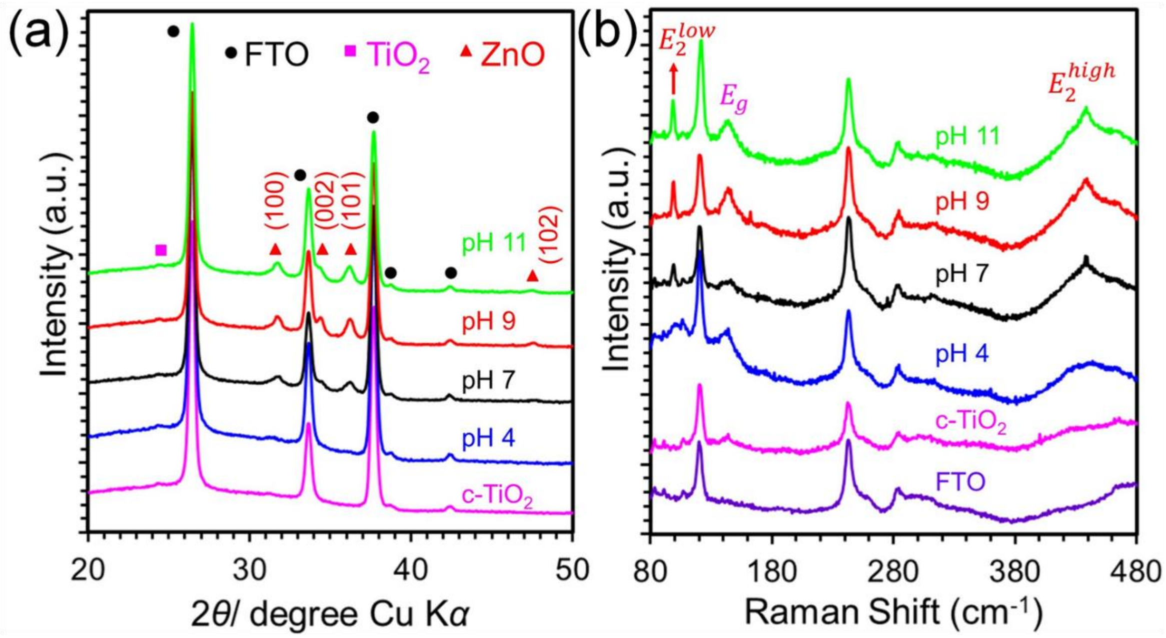

Figure 3.22 (a) XRD patterns and (b) Raman spectra of compact TiO_2 and ZnO NSs formed after H_2O oxidation at 90 °C under different pH conditions.

No other additional peaks of impurities or secondary phase were detected in the XRD patterns which signify the complete conversion of Zn to ZnO films. The poor overall NS alignment for each sample could be linked to the lattice mismatch between TiO_2 and ZnO crystals.

Figure 3.22(b) shows the room temperature Raman spectra of the c-TiO_2 and nanostructured ZnO films under excitation of a 532 nm laser line. The c-TiO_2 sample showed a single peak located at 144 cm^{-1}, corresponding to the main E_g mode of anatase vibration[62]. All nanostructured ZnO films, except the NPs, exhibited two sharp peaks centered at 99 cm^{-1} and 439 cm^{-1} which can be assigned to the E_2^{low} and E_2^{high} modes of non-polar optical phonons, respectively. The latter mode is due to the vibrations of oxygen atoms, while the vibrations of the heavy Zn sub-lattice activate the former[63]. These two dominant E_2 peaks are typical to the wurtzite phase of ZnO which further confirmed the highly crystalline nature of the NSs. On the other hand, the NPs showed broad and weak E_2 modes due to their low concentration.

Figure 3.23 presents the TEM and HRTEM images representing the general morphologies of all the samples. The TEM images (Figure 3.23(a)-(d), left) closely resemble the SEM images shown in Figure 3.20, whereas their HRTEM images (Figure 3.23(a)-(d), right) reveal that the as-prepared NSs have well-ordered crystalline planes. All the NSs can be seen to have a single crystalline structure, which is confirmed by their corresponding SAED patterns (insets) showing clear and sharp diffraction spots. Figure 3.23 also shows the EELS elemental mapping based on TEM images of the samples. The mappings further confirmed the chemical composition and revealed the elemental distribution of Zn and O elements over the entire surface area of the NSs.

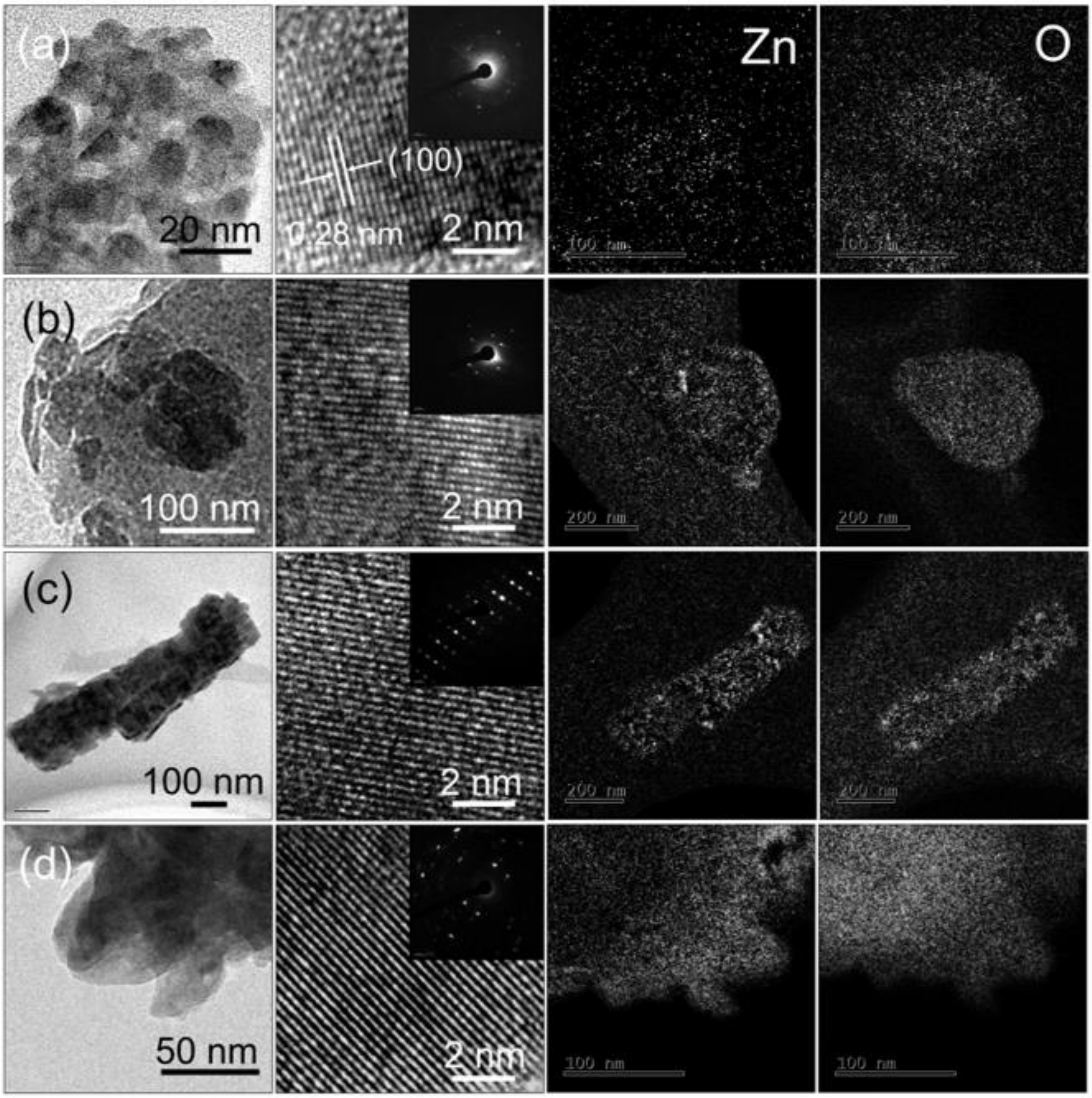

Figure 3.23 TEM images of ZnO NSs formed after H_2O oxidation for 8 h at 90 °C under different pH conditions: (a) pH 4, (b) pH 7, (c) pH 9 and (d) pH 11. Right images are their corresponding HRTEM images with SAED patterns as inset and EELS elemental mapping.

To gain more insight into the surface chemistry of the nanostructured ZnO films, the chemical states of Zn and O atoms were investigated by XPS. Figure 3.24 shows two main peaks centered at 1021.8 eV and 1044.8 eV, which are assigned to the Zn$2p_{3/2}$ and Zn$2p_{1/2}$ states, respectively. A spin-orbital splitting of 23.0 eV confirms that Zn exists only in the oxidized state (Zn^{2+}) 64. The core line of Zn $2p_{3/2}$ shows high symmetry on the surface of all films. The variation in the intensities of the peaks is consistent with the thickness of each sample.

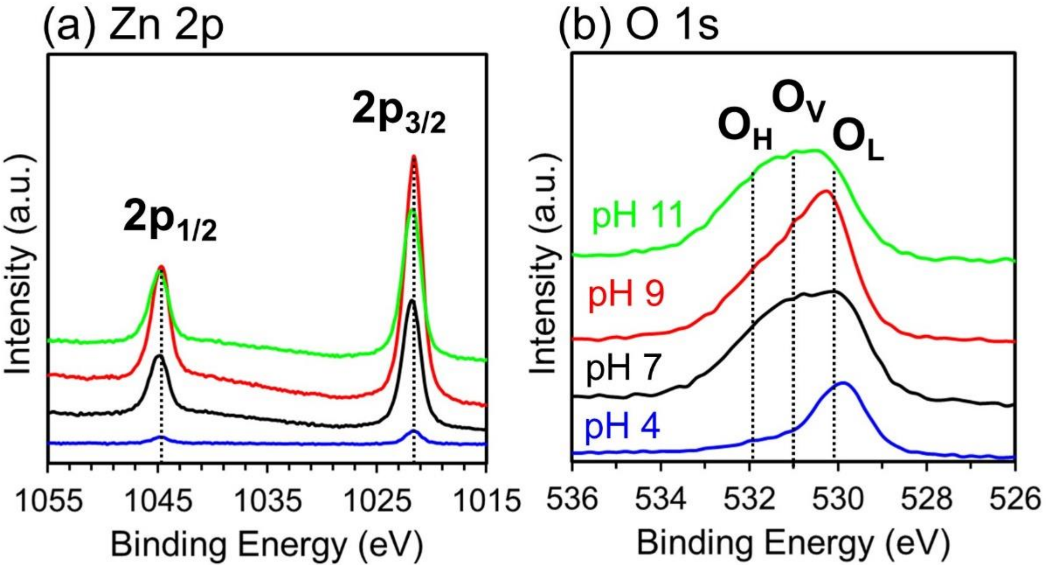

Figure 3.24 (a) Zn2p and (b)-(e) O1s high-resolution XPS spectra of nanostructured ZnO films formed after H_2O oxidation at 90 °C under different pH conditions.

The high-resolution O1s spectra of nanostructured ZnO films can be *described* as the superposition of three peaks by Gaussian distribution, centered at 530.3 eV, 531.0 eV, and 531.9 eV, respectively, as indicated in Figure 3.24(b)-(e). The low binding energy O_L peak located at 530.3 eV is attributed to O^{2-} ions in the wurtzite structure of a hexagonal Zn^{2+} ion array[65].The medium binding energy O_V peak, centered at 531.0 eV, is associated with O^{2-} in oxygen-deficient regions within the matrix of ZnO[66]. The higher binding energy O_H peak at 531.9 eV corresponds to chemisorbed oxygen such as OH^- and adsorbed H_2O[67]. Thus, changes in the area under these peaks can be correlated to the differences in the chemical states of oxygen at the surface of the nanostructured ZnO films. It can be seen that the O_H peak is nearly negligible for the NPs. As stated earlier, this result is highly probable since HCl was introduced to the system and subsequently neutralized most OH^- ions in H_2O.

Consequently, the relative O_H peak area for each sample is steadily intensified which is related to the supplied OH^- ions at higher pH values. It should be noted that the O_V peak is present in all ZnO films designating that a substantial amount of oxygen vacancies can also be found in each sample. Interestingly, the NTs is centered at O_V peak, which is associated with oxygen vacancies. At the same time, the reduction of the relative area under the O_L peak of the NTs indicates that the formation of zincate ions $[Zn(OH)_4]^{2-}$ weakens the Zn-O bonding and exposes the defects present on the central interior part of the NRs, which are most possibly oxygen vacancy related defects. Evidently, this investigation of the amount of OH^- groups and oxygen vacancies is essential for solar cell application, since these species are possible trap states for charge carriers.

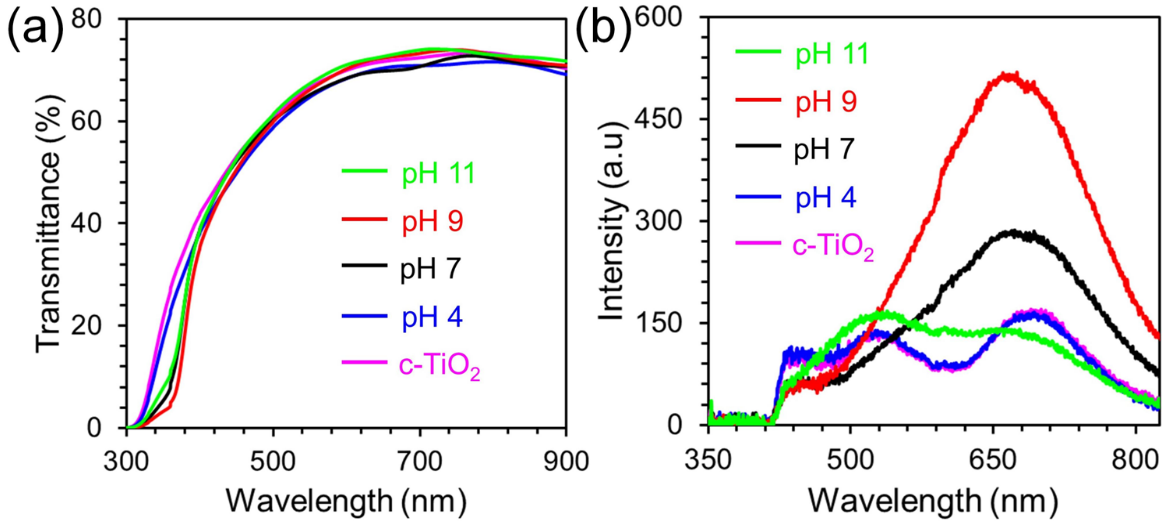

Figure 3.25 (a) Optical transmission and (b) room temperature photoluminescence spectra of c-TiO_2 and nanostructured ZnO films formed after H_2O oxidation at 90 °C under different pH conditions on FTO/glass substrate.

The transmittance of the nanostructured ZnO films is another important factor that strongly affects device performance. The optical transmission spectra of the c-TiO_2 and nanostructured ZnO samples are presented in Figure 3.25(a). It is well established that the transmittance of ZnO films not only depends on the film thickness, but is also related to their crystal size, defects and crystallinity[68]. The thicker nanostructured ZnO films formed at pH 9 and 11 have shown enhanced transmittance in the visible region compared with c-TiO_2 and other ZnO films. This could be correlated to their superior crystal quality as seen in their XRD and Raman spectra, as well as to their antireflection property originating from the suitable refractive index (n ~ 2) of ZnO[69]. In addition, the absorption edge shows a gradual red shift, which demonstrates a reduction in band gap for thicker nanostructured ZnO films.

Figure 3.25(b) shows the photoluminescence of all the samples at room temperature under excitation at $\lambda = 365$ nm. The NPs have shown exactly the identical emission spectrum as the c-TiO_2/FTO sample due to its low concentration and its emission is nearly negligible. The columnar NRs and MPs obtained at pH 9 and pH 7 exhibited similar orange-red emission centered at 650 nm. This emission is commonly attributed to the deep level oxygen interstitials (O_i) in ZnO[70]. The presence of higher OH^- group in columnar NRs might be another reason to its higher orange-red emission peak. Interestingly, a green emission centered at 530 nm appeared on the PL spectra of NTs, which is related to the radial recombination of photo-generated holes with electrons of singly charged oxygen vacancy states (V_O^+) [71]. This result also supports the emergence of large O_V peak area in its high-resolution O1s XPS spectrum.

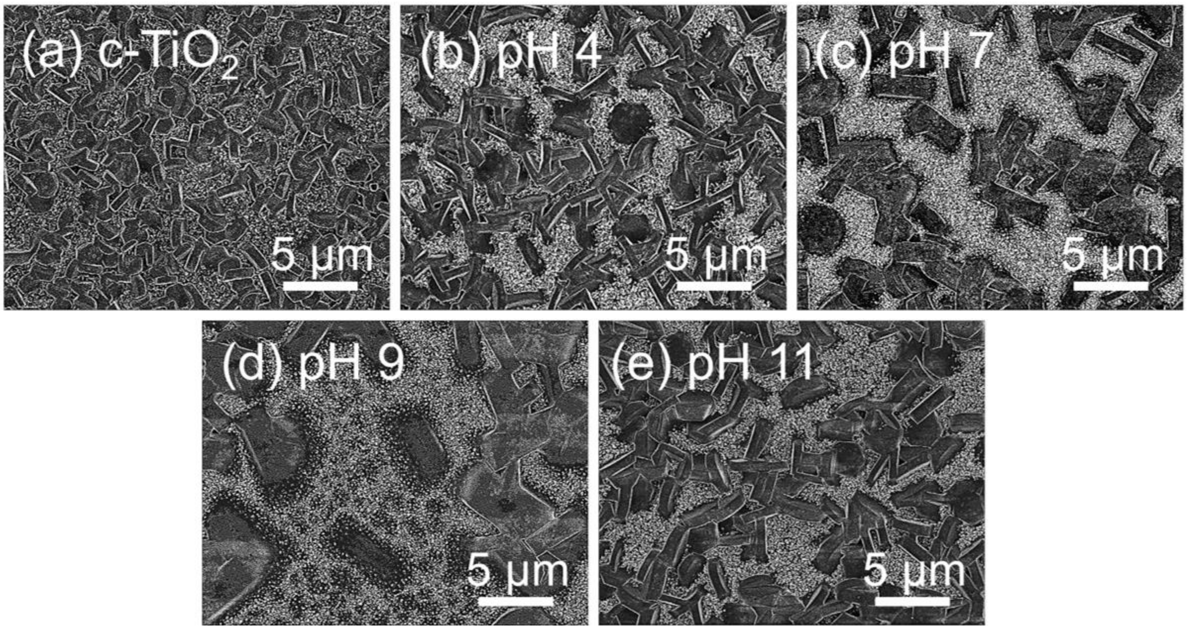

Figure 3.26 Top view SEM images of $(CH_3NH_3)_3Bi_2I_9$ films on top of nanostructured ZnO films formed after H_2O oxidation at 90 °C under different pH conditions.

The morphology of the active layer performs a significant role in solar cell devices. Hence, we carefully examined the development of the $(CH_3NH_3)_3Bi_2I_9$ film morphologies on top of ETLs, as shown in Figure 3.26. The deposited films, which are composed of hexagonal platelet-like crystals, display irregular orientation setting a large area of the samples uncovered. The surface coverage of perovskite films on c-TiO_2 and ZnO NPs (pH 4) was found to be comparable and denser compared with the ZnO MPs (pH 7), columnar NRs (pH 9) and NTs (pH 11). It is also noticeable that the most exposed ZnO NSs are on samples developed at pH 7 and pH 9, which is due to the higher density packing observed for the NSs under these pH values. This indicates that the morphology of the nanostructured ZnO films dramatically influences the surface uniformity of perovskite films. Consequently, this discontinuity of perovskite film layers might be another limiting factor on the performance.

Figure 3.27 shows the XRD patterns of $(CH_3NH_3)_3Bi_2I_9$ perovskite films deposited on nanostructured ZnO films. The diffraction peaks at 2θ = 11.7°, 12.6°, 14.5°, 17.1°, 24.6°, 25.2°, 29.1°, 31.7°, and 32.1° can be indexed to the (100), (101), (102), (103), (006), (202), (204), (205), and (211) planes, respectively, demonstrating the formation of hexagonal $(CH_3NH_3)_3Bi_2I_9$ crystals with space group $P6_3/mmc$[72]. No BiI_3 peaks were detected in all the spectra indicating that all BiI_3 was converted completely into $(CH_3NH_3)_3Bi_2I_9$. It should be noted that the perovskite films deposited on NPs and c-TiO_2 exhibited enhanced intensity for (101) peak suggesting preferential orientation along [101] direction. The optical absorption measurements showed an edge at approximately 560 nm (Figure 3.27(b)), which was consistent with the typical absorption characteristic of $(CH_3NH_3)_3Bi_2I_9$[73].

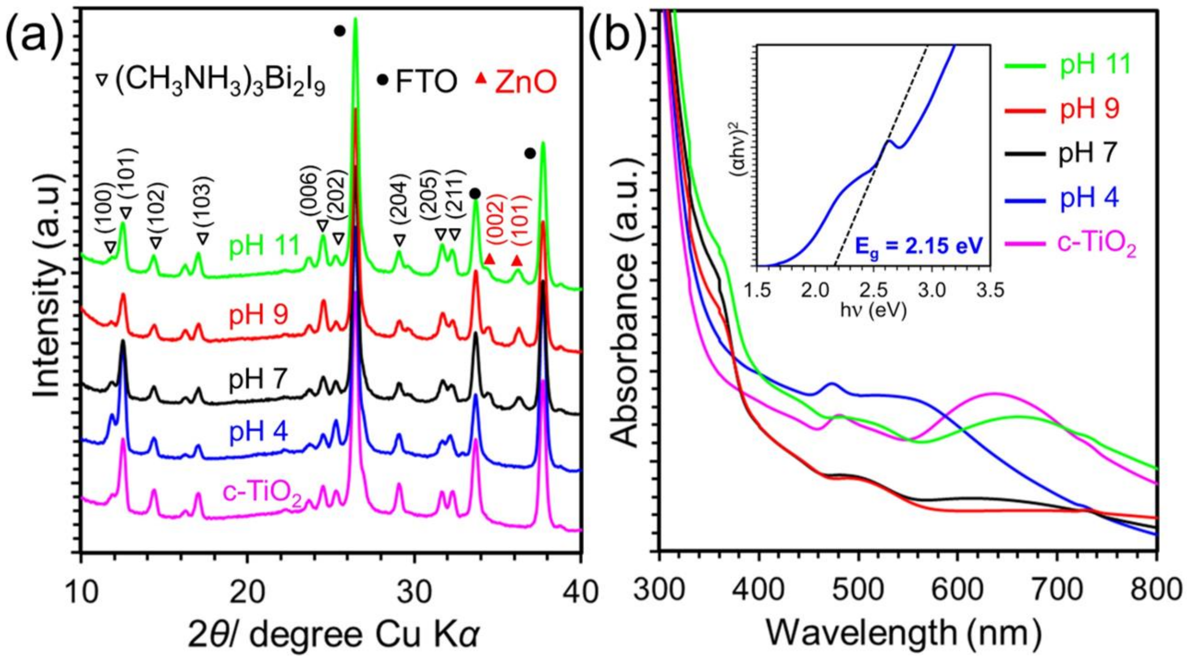

Figure 3.27 (a) XRD patterns and (b) optical absorption and photoluminescence spectra of $(CH_3NH_3)_3Bi_2I_9$ films on top of nanostructured ZnO films formed after H_2O oxidation at 90 °C under different pH conditions.

The perovskite films formed on c-TiO_2 and ZnO NPs revealed higher absorption owing to its denser configuration and thinner underlying ZnO layer. The calculated indirect band gap of $(CH_3NH_3)_3Bi_2I_9$ from Tauc plot analysis is about 2.15 eV. To examine the preliminary charge transfer between the active layer and ETLs, the steady-state photoluminescence spectra of perovskite layer on top of c-TiO_2 and nanostructured ZnO films are presented in Figure 3.28(a). The weak emissions centered at ~595 nm corresponds with the indirect band gap of the perovskite films. The peak at 520 nm originated from the FTO substrate, which subsequently masked the emission from the non-uniform perovskite layers.

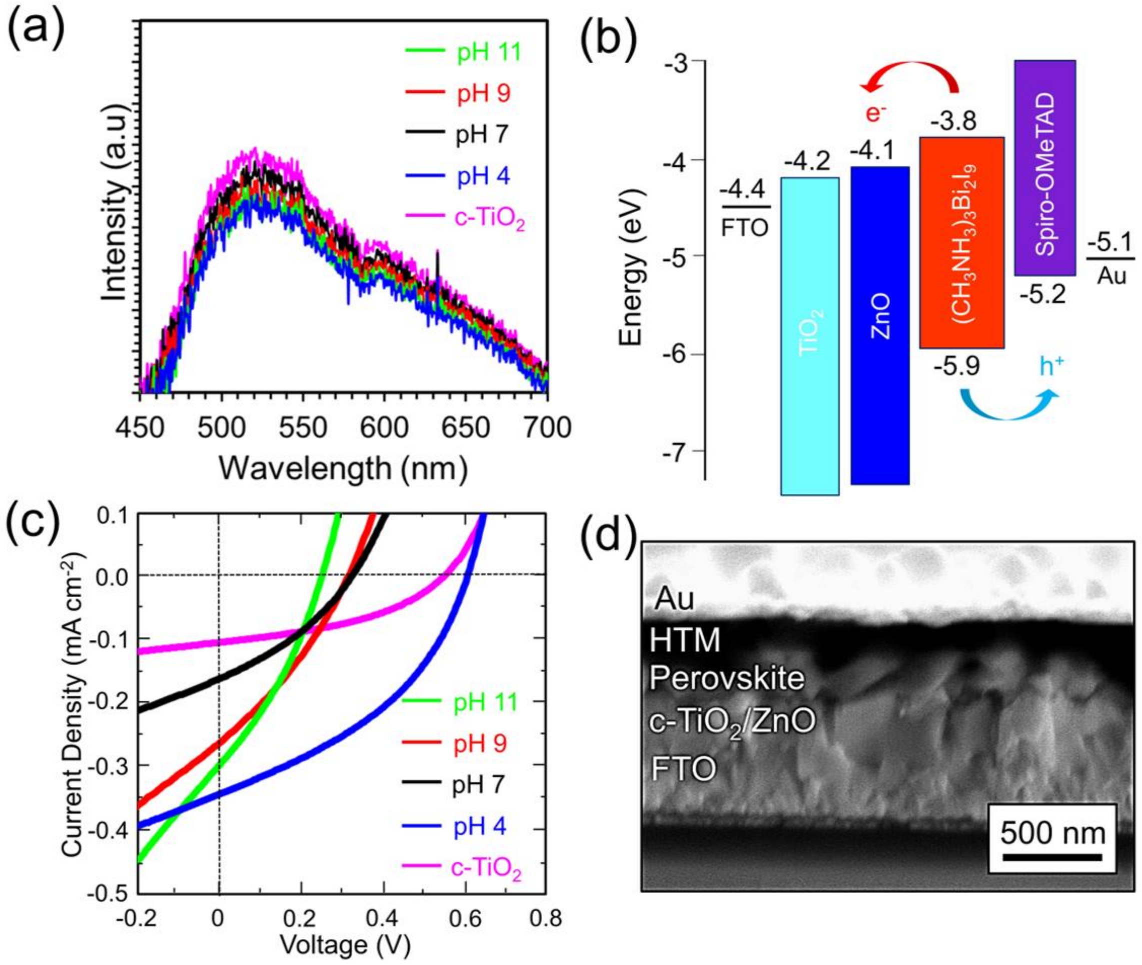

Figure 3.28 (a) Schematic illustration, (b) energy level diagram, and (c) *J-V* curves of $(CH_3NH_3)_3Bi_2I_9$ solar cells based nanostructured ZnO films grown at different pH conditions. (d) Cross-sectional SEM image of the best performing device based on ZnO NPs.

Additionally, the NP/$(CH_3NH_3)_3Bi_2I_9$ bilayer showed the minimum PL intensity indicating a faster electron extraction rate. The energy level diagram of PSCs based on nanostructured ZnO films are shown in Figure 3.28(b). The device consists of glass/FTO/c-TiO_2/ZnO NSs/$(CH_3NH_3)_3Bi_2I_9$/Spiro-OMeTAD/Au. The energy levels for the conduction band (CB) and valence band (VB) edges of $CH_3NH_3)_3Bi_2I_9$ are at -3.8 and -5.9 eV, with a good match of the ZnO CB of -4.1 eV and Spiro-OMeTAD VB of -5.2 eV. The thickness of the perovskite layer based on ZnO NPs is approximately 250 nm, whereas the thickness of

Spiro-MeOTAD is about 150 nm (Figure 3.28(d)). It can be seen that some unfilled regions emerged in between the platelet-like absorber crystals and Spiro-MeOTAD is able to permeate directly to the ZnO layer, which may lead to increased recombination.

To evaluate the effect of different nanostructured ZnO on the photovoltaic performance, $(CH_3NH_3)_3Bi_2I_9$ solar cells were fabricated following the same experimental process. Figure 3.29 present the photovoltaic parameters and statistical results of $(CH_3NH_3)_3Bi_2I_9$ solar cells based on c-TiO_2 and nanostructured ZnO films, plotted as a function of pH value. The corresponding photocurrent (J)-voltage (V) curves under simulated AM 1.5G illumination (100 mW cm^{-2}) are shown in Figure 3.28(c). The device based on ZnO NPs, which were grown in acidic H_2O, exhibited the highest short circuit current density (J_{sc}) of 0.342 mA cm^{-2}, an open circuit voltage (V_{oc}) of 0.608 V, a fill factor (FF) of 40.0, a maximum PCE (PCE_{max}) of 0.083% and an average PCE (PCE_{ave}) of 0.073%. This value is comparable with other studies that used mesoporous TiO_2 as ETL and employed solution-based techniques for perovskite deposition, as shown in Table 3.3. The ZnO NRs and NTs-based solar cells followed with comparable PCE_{max} of 0.026% and 0.024%. Subsequently, the NTs-based devices showed a more consistent performance with slightly higher PCE_{ave} of 0.021% compared with 0.017% for the NRs-based devices. These results demonstrate that the thickness and morphology of the nanostructured ZnO films have a considerable effect on the device performance.

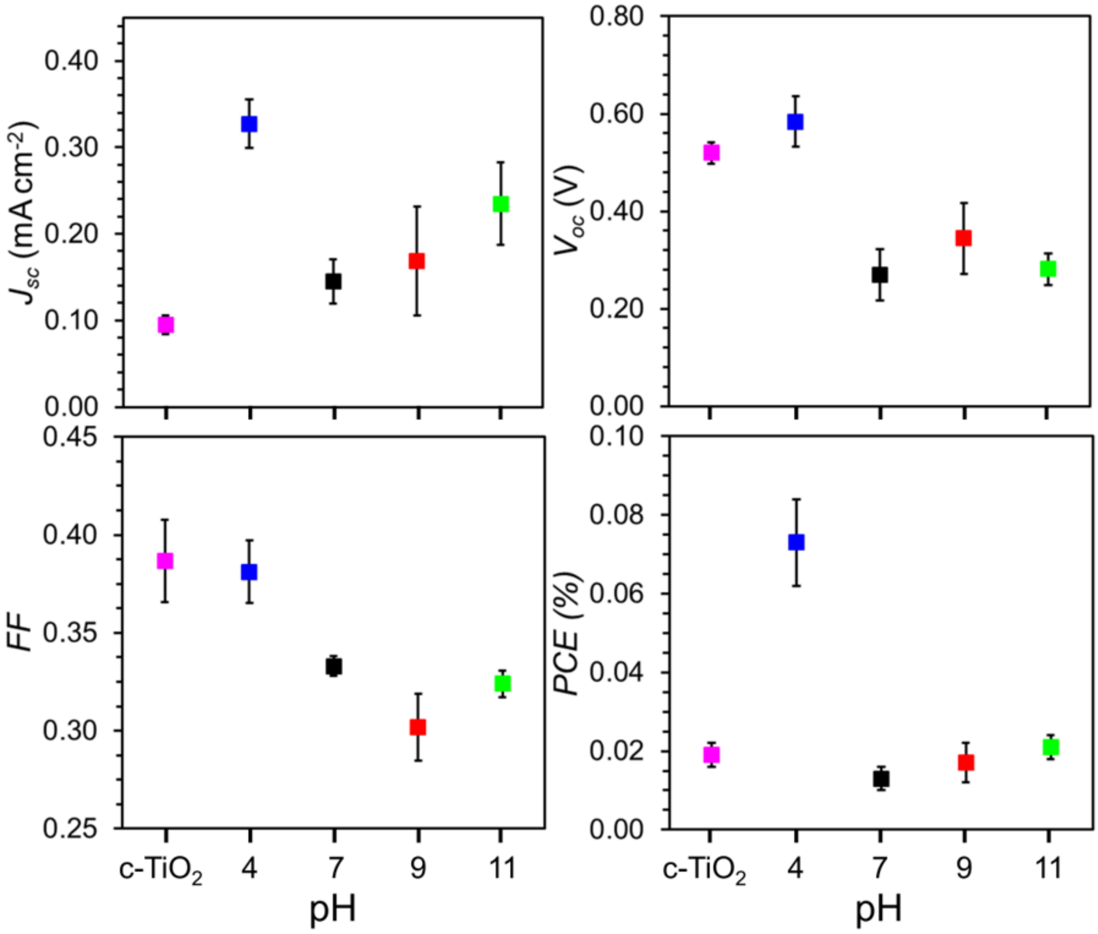

Figure 3.29 Photovoltaic parameters of PSCs based on c-TiO$_2$ and nanostructured ZnO films grown at different pH conditions. Values (average of 5 cells) are plotted as a function of pH value.

The enhancement in *PCE* with thinner and smoother ZnO films is attributed to the improved perovskite surface coverage, which results in superior interface between the active layer and charge selective layers and reduces junction resistance[74]. Thus, a more efficient and kinetically favorable charge extraction takes place. At the same time, it can be observed that the V_{oc} increased dramatically from 0.3 V for thicker ZnO-based devices to around 0.6 V for the pH 4-ZnO-based devices. Moreover, ZnO NPs have fewer recombination centers due to the absence of OH^- group at its surface, which results in reduced leakage current[75]. The low photocurrent values are generally associated to the low rate of charge separation and slow-charge carrier transport within the $(CH_3NH_3)_3Bi_2I_9$ perovskite[76].

Table 3.3 Materials and photovoltaic parameters of solution-processed $(CH_3NH_3)_3Bi_2I_9$ solar cells based on ZnO or mesoporous TiO_2 as ETLs.

ETL	PCE_{max} [%]	Active Area [cm^2]	Reference
ZnO NPs	0.083	0.190	This work
TiO_2	0.108	0.090	73
TiO_2	0.256	0.090	73
TiO_2	0.053	0.096	76
TiO_2	0.023	0.120	77
TiO_2	0.054	NA	78
TiO_2	0.070	0.087	79

On the other hand, the MPs-based solar cells revealed the lowest PCE_{max} of 0.017% and PCE_{ave} of 0.013%. This low performance of pH 7-ZnO based solar cell could be attributed to its densely packed configuration, preventing the perovskite layer to diffuse throughout its surface area. Another possible reason is the increased recombination within the MPs, since the smaller NRs comprising them were seen to be lying parallel to the FTO/glass substrate. Hence, the initial extracted electrons from the perovskite are slowly transported to the cathode (FTO). Consequently, this leads to relatively low J_{sc} and V_{oc} values of 0.160 mA cm^{-2} and 0.323 V, respectively. As a reference, the c-TiO_2-based solar cell showed a respectable V_{oc} (0.550 V) and FF (41.0) values but a very low J_{sc} value of 0.103 mA cm^{-2}, resulting in a PCE_{max} of 0.023% and PCE_{ave} of 0.019%. Clearly, this implies that the 15 nm thick c-TiO_2 as ETL is not enough for efficient electron extraction and transfer due to its limited contact with perovskite layer. Figure 3.30 shows that all the devices displayed small hysteresis in *J*-*V* curves, which could be due to the unbalanced electron and hole transfer at the interface of their corresponding selective layers[80]. This uneven carrier movement possibly originates from the energy level mismatch between the $(CH_3NH_3)_3Bi_2I_9$ layer and its neighboring charge transporting layers[81].

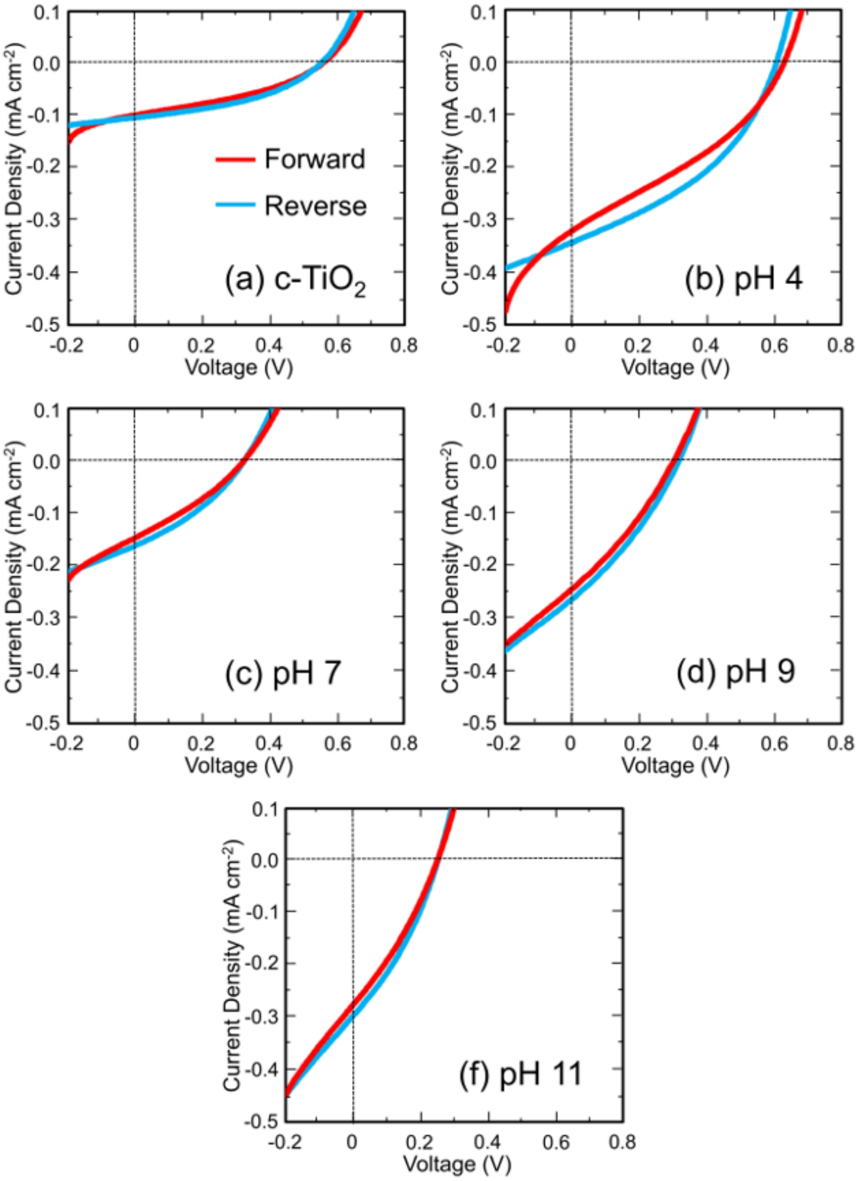

Figure 3.30 *J-V* curves and hysteresis behavior of $(CH_3NH_3)_3Bi_2I_9$ solar cells based on nanostructured ZnO films grown at different pH conditions.

The thickness of Zn film was also varied at optimum pH to determine its effect on the device performance. Figure 3.31(a) summarizes the photovoltaic parameters and statistical results $(CH_3NH_3)_3Bi_2I_9$ solar cells based on nanostructured ZnO film formed at pH 4 by varying the thickness of Zn film. The solar cell device based on ZnO NPs, which were grown from 80 nm-Zn film, still exhibited the PCE_{max} of 0.083%, followed by 50 nm-Zn film with PCE_{max} of 0.047% and PCE_{ave} of 0.042%, and 100 nm-Zn film with PCE_{max} of 0.041% and PCE_{ave} of 0.037%. Thus, based on these results we found that the optimum thickness for Zn thin film is 80 nm. In order to elucidate the long-term stability of the ZnO-based $(CH_3NH_3)_3Bi_2I_9$ solar cells, the devices were kept in ambient conditions without any sealing for almost one month. Figure 3.31(b) shows the PCE of the best performing device as a function of time. It shows that the device retained 75% of its efficiency after 4 weeks, revealing a remarkable stability over the Pb-based PSCs.

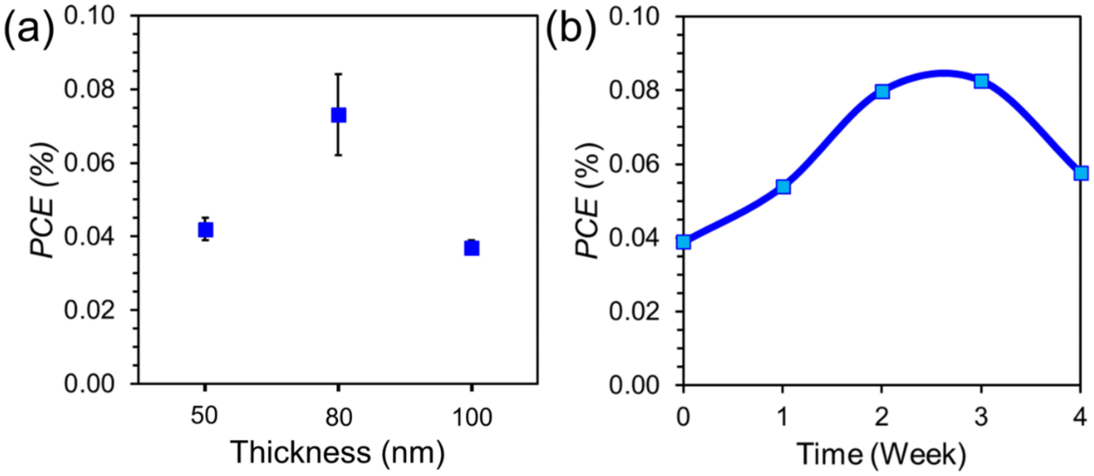

Figure 3.31 (a) Photovoltaic parameters of PSCs based on nanostructured ZnO films formed through H_2O oxidation at pH 4 by varying the thickness of Zn film. (b) Long-term stability of the best performing solar cell.

3.3 Summary

This chapter presented a facile synthesis method employing a simple oxidation of Zn thin films in H_2O to produce nanostructured ZnO as ETL in PSCs. The necessity for any growth directing agents or complex equipment is eliminated through our innovative technique. By varying the H_2O temperature and growth time, various surface morphologies such as particles, fibers, rods, tubes and platelets having different preferential growth orientations were obtained. A fabricated PSC device based on pointed ZnO NRs, which are generated at 90 °C for 8 h of H_2O oxidation, exhibited the highest *PCE* of 5.96% and average *PCE* of 5.46% with weak hysteresis. This sample also displayed the highest *EQE* over the whole wavelength range among all the fabricated devices. The development of rod-like structures led to better perovskite penetration and effective interfacial area, which resulted in reduced charge carriers' path length and increased photovoltaic parameters. All devices showed good stability over time reaching their maximum efficiencies after 15-20 days of storage due to the slow drying of the solution-processed layers. I believe that through the optimization of Zn thin film and perovskite deposition, as well as the use of better HTL and electrodes, much higher efficiencies can be achieved.

Furthermore, the modification of H_2O oxidation technique by varying the pH of H_2O was also explored. The resulting nanostructured ZnO films were then applied as ETLs for Bi-based Pb-free PSCs. Various morphologies such as particles, rods and tubes with different growth orientations were generated. These nanostructured films were comprehensively characterized to determine their effect on the solar cell performance. The surface coverage of the perovskite films depended strongly on the morphology and surface roughness of the nanostructured ZnO films. A device based on ZnO NPs, which were obtained in acidic H_2O with a pH of 4, exhibited the maximum *PCE* of 0.083%, average *PCE* of 0.073% and small hysteresis. The superior coverage of perovskite films on top of ZnO NPs led to a better interfacial area, which resulted in reduced charge carrier recombination and increased photovoltaic parameters. These NPs also have the smallest amount of hydroxyl group which are possible trap centers for the extracted electrons from the perovskite layer. The best performing device shows good stability in ambient conditions for almost a month. These results indicate that the nanostructured ZnO films can be an effective ETL for Pb-free PSCs. Moreover, uniform and smoother $(CH_3NH_3)_3Bi_2I_9$ films should be developed through strategic optimizations to further improve its photovoltaic performance. Overall, these results suggest that the oxidation of Zn thin films in H_2O can produce highly crystalline nanostructured ZnO which can be utilized not only in photovoltaics but also in other optoelectronic devices.

References

(1) M.D. Balela, C.M. Pelicano, J.D. Ty and H. Yanagi, *Opt. Quant. Electron.*, 2017, **49**, 3.

(2) C. M. Pelicano and H. Yanagi, *J. Mater. Chem. C*, 2017, **5**, 8059-8070.

(3) T. Jacobsson, J. Correa-Baena, E. H. Anaraki, B. Philippe, S. Stranks, M. Bouduban, W. Tress, K. Schenk, J. Teuscher, J. Moser, H. Rensmo and A. Hagfeldt, *J. Am. Chem. Soc.*, 2016, **138**, 10331-10343.

(4) S. Zhang, H-S. Chen, K. Matras-Postolekl and P. Yang, *Phys. Chem. Chem. Phys.*, 2015, **17**, 30300-30306.

(5) J. Lauritsen, S. Porsgaard, M. Rasmussen, M. Jensen, R. Bechstein, K. Meinander, B. Clausen, S. Helveg, R. Wahl, G. Kresse and F. Besenbacher, *ACS Nano*, 2011, **5**, 5987-5994.

(6) K.Yadav, B. R. Mehta, S. Bhattacharya and J. P. Singh, *Sci Rep.*, 2016, **6**, 35073.

(7) S. Bai, L. Wang, Z. Li and Y. Xiong, *Adv. Sci*, 2017, **4**, 1600216.

(8) P. Roberge, Corrosion Engineering Principles and Practice, McGraw Hill Professional, USA, 2008.

(9) N. Sato, Basics of Corrosion Chemistry in Green Corrosion Chemistry and Engineering: Opportunities and Challenges, Wiley-VCH Verlag GmbH & Co. KGaA, Weinheim, Germany, 2011.

(10) H. Park, K.-J. Byeon, K.-Y. Yang, J.-Y. Cho and H. Lee, *Nanotechnology*, 2010, **21**, 355304.

(11) L. Xiong, M. Qin, G. Yang, Y. Guo, H. Lei, Q. Liu, W. Ke, H. Tao, P. Qin, S. Li, H. Yu and G. Fang, *J. Mater. Chem. A*, 2016, **4**, 8374-8383.

(12) H.B. Zeng, Z. Li, W.P. Cai, B. Cao, P. Liu and S. Yang, *J. Phys. Chem. B*, 2007, **111**, 14311-14317.

(13) L. Wu, Y. Wu, X. Pan and F. Kong, *Opt. Mater.*, 2006, **28**, 418-422.

(14) C. Wehrenfennig, M. Liu, H. J. Snaith, M. B. Johnston and L. M. Herz, *J. Phys. Chem. Lett.*, 2014, 5, 1300-1306.

(15) D. Liu, J. Yang and T. Kelly, *J. Am. Chem. Soc.*, 2014, **136**, 17116-17122.

(16) D. H. Kim, G. S. Han, W. M. Seong, J. W. Lee, B. J. Kim, N. G. Park, K. S. Hong, S. Lee and H. S. Jung, *ChemSusChem*, 2015, **8**, 2392-2398.

(17) J-H. Im, J. Luo, M. Franckevičius, N. Pellet, P. Gao, T. Moehl, S. M. Zakeeruddin, M. K. Nazeeruddin, M. Grätzel and N-G. Park, *Nano Letters*, 2015, **15**, 2120-2126.

(18) P. Ruankhama, D. Wongratanaphisan, A. Gardchareon, Surachet Phadungdhitidhada, S. Choopun, T. Sagawa, *Appl. Surf. Sci.*, 2017, 410, 393-400.

(19) P. Nagarjuna, K. Narayanaswamy, T. Swetha, G. Hanumantha Rao, S. P. Singh, G.D. Sharma, *Electrochim. Acta*, 2015, 151, 21-26.

(20) Md. M. Rahman, N. Uekawa, F. Shiba, Y. Okawa, M. Sakai, K. Yamamoto, K. Kudo, T. Konishi, *Jpn. J. Appl. Phys.*, 2016, 55, 01AE09.

(21) M. Seetharaman S, P. Nagarjuna, P. N. Kumar, S. P. Singh, M. Deepac, M. A. G. Namboothiry, *Phys. Chem. Chem. Phys.*, 2014, 16, 24691.

(22) Y. Zhang, W. Liu, F. Tan, Y. Gu, *J. Power Sources*, 2015, 274, 1224-1230

(23) Z. Qiu, S. Yuan, H. Gong, H. Zhang, X. Qiu, T. Luo, B. Cao, *J. Am. Ceram. Soc.*, 2016, 1-7.

(24) N. K. Elumalai, Md A. Mahmud, D.Wang, A. Uddin, *Energies*, 2016, **9**, 861.

(25) K. Mahmood, B. Swain, A. Kirmania and A. Amassian, *J. Mater. Chem. A*, 2015, **3**, 9051-9057.

(26) F. J. Ramos, M. C. López-Santos, E. Guillén, M. K. Nazeeruddin, M. Grätzel, A. R. Gonzalez-Elipe and S. Ahmad, *ChemPhysChem*, 2014, **15**, 1148-1153.

(27) J. M. Azpiroz, E. Mosconi, J. Bisquert and F. De Angelis, *Energy Environ. Sci.*, 2015, **8**, 2118-2127.

(28) J. Haruyama, K. Sodeyama, L. Y. Han, and Y. Tateyama, *J. Am. Chem. Soc.*, 2015, **137**, 10048-10051.

(29) S. D. Stranks and H. J. Snaith, *Nat. Nanotechnol.*, 2015, **10**, 391-402.

(30) J. Xu, A. Buin, A. Ip, W. Li, O. Voznyy, R. Comin, M. Yuan, S. Jeon, Z. Ning, J. McDowell, P. Kanjanaboos, J-P. Sun, X. Lan, L. N. Quan, D. H. Kim, I. G. Hill, P. Maksymovych and E. H. Sargent, *Nat Commun.*, 2015, **6**, 7081.

(31) C. Eames, J. M. Frost, P. R. F. Barnes, B. C. O'Regan, A. Walsh and M. S. Islam, *Nat Commun.*, 2015, **6**, 7497.

(32) Y. Zhang, M. Liu, G. Eperon, T. Leijtens, D. McMeekin, M. Saliba, W. Zhang, M. de Bastiani, A. Petrozza, L. Herz, M. Johnston, H. Lin and H. J. Snaith, *Mater. Horiz.*, 2015, **2**, 315-322.

(33) M. D. Bastiani, G. Dell'Erba, M. Gandini, V. D'Innocenzo, S. Neutzner, A. R. S. Kandada, G. Grancini, M. Binda, M. Prato, J. M. Ball, M. Caironi and A. Petrozza, *Adv. Energy Mater.*, 2016, **6**, 1501453.

(34) J. You, L. Meng, T-B. Song, T-F. Guo, Y. (M.) Yang, W-H Chang, Z. Hong, H. Chen, H. Zhou, Q. Chen, Y. Liu, N. De Marco and Y. Yang, *Nat. Nanotechnol.*, 2016, **11**, 75.

(35) K. Rahimi, I. Botiz, J. O. Agumba, S. Motamen, N. Stingelin, G. Reiter, *RSC Adv.*, 2014, **4**, 11121.

(36) J. Zhang, P. Barboux and T. Pauporté, *Adv. Energy Mater.*, 2014, **4**, 1400932.

(37) Y. Kato, L. K. Ono, M. V. Lee, S. Wang, S. R. Raga and Y. Qi, *Adv. Mater. Interfaces*, 2015, **2**, 1500195.

(38) D. Pradhan and K. T. Leung, *J. Phys. Chem. C,* 2008, **112**, 1357-1364.

(39) S.B. Kulkarni, U.M. Patil, R.R. Salunkhea, S.S. Joshi and C.D. Lokhande, *J Alloy Compd.*, 2011, **509**, 3486-3492.

(40) F. Hao, C. Stoumpos, D. Cao, R. Chang and Kanatzidis, *Nat. Photon.,* 2014, **8**, 489−494.

(41) D. Sabba, H. K. Mulmudi, R. R. Prabhakar, T. Krishnamoorthy, T. Baikie, P. P. Boix, S. Mhaisalkar and N. Mathews, *J. Phys. Chem. C,* 2015, **119**, 1763−1767.

(42) P. Cheng, T. Wu, J. Zhang, Y. Li, J. Liu, L. Jiang, X. Mao, R.-F. Lu, W.-Q. Deng and K. Han, *J. Phys. Chem. Lett.,* 2017, **8**, 4402−4406.

(43) M. G. Ju, J. Dai, L. Ma and X. C. Zeng, *J. Am. Chem. Soc.*, 2017, **139**, 8038−8043.

(44) N. K. Noel, S. D. Stranks, A. Abate, C. Wehrenfennig, S. Guarnera, 65 A. A. Haghighirad, A. Sadhanala, G. E. Eperson, M. B. Johnston, A. M. Petrozza, L. M. Herz, and H. J. Snaith, *Energy Environ. Sci.*, 2014, 7, 3061.

(45) T. Krishnamoorthy, H. Ding, C. Yan, W. L. Leong, T. Baikie, Z. Zhang, M. Sherburne, S. Li, M. Asta, N. Mathews and S. G. Mhaisalkar, *J. Mater. Chem. A*, 2015, **3**, 23829–23832.

(46) F. Jiang, D. Yang, Y. Jiang, T. Liu, X. Zhao, Y. Ming, B. Luo, F. Qin, J. Fan, H. Han, L. Zhang and Y. Zhou, *J. Am. Chem. Soc.*, 2018, **140**, 1019−1027.

(47) D. Cortecchia, H. A. Dewi, J. Yin, A. Bruno, S. Chen, T. Baikie, P. P. Boix, M. Grätzel, S. Mhaisalkar, C. Soci and N. Mathews, *Inorg. Chem.*, 2016, **55**, 1044–1052.

(48) L. M. Schoop, L. Muchler, C. Felser and R. J. Cava, *Inorg. Chem.*, 2013, **52**, 5479–5483.

(49) R. Brandt, V. Stevanovi´c, D. Ginley and T. Buonassisi, *MRS Commun.*, 2015, **5**, 265–275.

(50) S. Jain, D. Phuyal, M. Davies, M. Li, B. Philippe, C. De Castro, J. Kim, T. Watson, W. Tsoi, O. Karis, H. Rensmo, G. Boschloo, T. Edvinsson and J. Durrant, *Nano Energy,* 2018, **49**, 614-624.

(51) V. Devabharathi, K.L. Palanisamy and N. Meenakshi Sundaram, *Superlattices Microstruct.*, 2014, **75,** 99–104.

(52) W-Y. Wu, W-Y. Kung and J-M. Ting, *J. Am. Ceram. Soc.*, 2011, **94**, 699–703.

(53) Z. Zang and X. Tang, *J Alloys Compd.*, 2015, **619**, 98–101

(54) C. M. Pelicano and H. Yanagi, Appl. Surf. Sci., 2019, **467-468**, 932−939.

(55) G. Fakhrullina, F. Akhatova, M. Kibardina, D. Fokin and R. Fakhrullin, *NanoMed-Nanotechnol.*, 2017, **13**, 483-491.

(56) B. Ruqia, K. Nam, H. Lee, G. Lee and S. Choi, *CrystEngComm*, 2017, **19**, 1454-1458.

(57) S. Zhang, H.-S. Chen, K. Matras-Postolekl and P. Yang, *Phys. Chem. Chem. Phys.*, 2015, **17**, 30300–30306.

(58) Q. Ahsanulhaq, A. Umar and Y. B. Hahn, *Nanotechnology*, 2017, **18**, 115603.

(59) K. S. Ranjith, B. Kiruthika and R. T. Rajendrakumar, *J. Micros.*, 2013, **252**, 217-225.

(60) Sunaina, M. Sreekanth, S. Ghosh, S. K. Mehta, A. K. Ganguli and Menaka Jha, *CrystEngComm*, 2017, **19**, 2264-2270.

(61) H. S. Jang, B. Son, H. Song, G. Y. Jung and H. C. Ko, *J. Mater. Sci.,* 2014, **49**, 8000–8009.

(62) V. Manthina, J. P. C. Baena, G. Liu and A. Agrios, *J. Phys. Chem. C*, 2012, **116**, 23864-23870.

(63) I. Musa, N. Qamhieh and S. Mahmoud, *Results Phys.*, 2017, **7**, 3552-3556.

(64) B. Panigrahy, M. Aslam and D. Bahadur, *J. Phys. Chem. C*, 2010, **114**, 11758−11763.

(65) M. Chen, X. Wang, Y. H. Yu, Z. L. Pei, X. D. Bai, C. Sun, R. F. Huang and L. S. Wen, *Appl. Surf. Sci.*, 2000, **158**, 134−140.

(66) R. N. Aljawfi and S. Mollah, *J. Magn. Magn. Mater.*, **323**, 3126−3132.

(67) J. C. C. Fan and J. B. Goodenough, *J. Appl. Phys.*, 1977, **48**, 3524.

(68) Z. Liang, Q. Zhang, L. Jiang and G. Cao, *Energy Environ. Sci.*, 2015, **8**, 3442-3476.

(69) K.P. Bhuvana, J. Elanchezhiyan, N. Gopalakrishnan and T. Balasubramanian, *J Alloys Compd.*, 2009, **473**, 534-537.

(70) D. Liu, Y. Lv, M. Zhang, Y. Liu, Y. Zhu, R. Zong and Y. Zhu, *J. Mater. Chem. A*, 2014, **2**, 15377-15388.

(71) Y. Jiao, H. J. Zhu, M. J. Zhou, X. F. Wang and Q. Li, *J. Phys. Chem. C*, 2010, **114**, 208–211.

(72) K. Eckhardt, V. Bon, J. Getzschmann, J. Grothe, F. Wisser and S. Kaske, *Chem. Comm.* 2016, **52**, 3058-3060.

(73) T. Singh, A. Kulkarni, M. Ikegami and T. Miyasaka, *ACS Appl. Mater. Interfaces*, 2016, **8**, 14542–14547.

(74) M. Chen, L. Wan, M. Kong, H. Hu, Y. Gan, J. Wang, F. Chen, Z. Guo, D. Eder and S. Wang, *J Alloys Compd.*, 2018, **738**, 422-431.

(75) W. Qin, X. Xu, D. Liu, C. Ma, Y. Yang, S. Yin, F. Zhang and J. Wei, *J. Renew. Sustain. Energy*, 2013, **5**, 053106.

(76) H. Li, C. Wu, Y. Yan, B. Chi, J. Pu, J. Li and S. Priya, *ChemSusChem*, 2017, **10**, 3994-3998.

(77) C. Lan, J. Luo, S. Zhao, W. Liu and S. Hayase, *J. Alloys Compd.*, 2017, **701**, 834-840.

(78) M. Kong, H. Hu, L. Wan, M. Chen, Y. Gan, J. Wang, F. Chen, B. Dong, D. Eder and S. Wang, *RSC Adv.*, 2017, **7**, 355-349.

(79) T. Okano and Y. Susuki, *Mater. Lett.*, 2017, **191**, 77-79.

(80) J. H. Heo, H. J. Han, D. Kim, T. K. Ahn and S. H. Im, *Energy Environ. Sci.*, 2015, **8**, 1602-1608.

(81) M. Lyu, J.-H. Yun, M. Cai, Y. Jiao, P. V. Bernhardt, M. Zhang, Q. Wang, A. Du, H. Wang, G. Liu and L. Wang, *Nano Res.*, 2016, **9**, 692-702.

Chapter 4

Enhanced Charge Transport in Al-doped ZnO Nanotubes Designed via Simultaneous Etching and Al Doping of H_2O-Oxidized ZnO Nanorods for Perovskite Solar Cells

4.1 Introduction

One dimensional (1-D) ZnO nanotubes (NTs) could be outstandingly valuable in solar cells owing to their higher surface area as well as a direct path for charge transport. In spite of this, the application of ZnO NTs in photovoltaics has been very limited due to the complexity of its fabrication route. For instance, Wei et al. described an improvement in the photocurrent density of Cu_2O/ZnO heterojunction solar cells based on ZnO NTs[1]. In their report, the ZnO NTs were formed by a two-step method, wherein electrodeposited ZnO nanorods (NRs) were immersed in KOH at 80 °C for 2 h. Another study established the applicability of ZnO NTs, constructed through a combination of anodic aluminum oxide (AAO) templating and atomic layer deposition (ALD), as photoanodes in dye-sensitized solar cells[2]. Hence, the challenge now is to develop a simpler, faster and energy-efficient protocol of designing ZnO NTs.

Furthermore, the possibility of modulating the electronic properties of ZnO NTs via low-content doping opens challenging paths to further boost the overall device performance beyond its current limits. Through accurate doping, the electronic properties of wide band gap semiconductors like ZnO can be enhanced but their transparency can be maintained[3]. A number of typical n-type dopants such as Al, Ga and In have been commonly used to develop highly conductive ZnO films[4-6]. Among these Group 13 elements, Al is the most ideal dopant since it is low cost, highly reactive, non-toxic and abundant in nature. Additionally, Al^{3+} ions has a smaller ionic radius (~0.54 Å) with respect to Zn^{2+} ions (~0.74 Å) promoting easy substitution in the ZnO lattice[4]. Several doping techniques for AZO thin films have been described in the literature, such as metal organic chemical vapor deposition (MOCVD) with dimethylzinc-triethylamine (DMZn-TEN) and trimethylaluminum (TMAl) as Zn and Al sources[7], ion implantation[8], and magnetron sputtering deposition with a mixture target of Al_2O_3 and ZnO[9], among others. However, these above-mentioned methods have limited doping tunability and involved introduction of dopants during thin film growth. The latter could consequently affect or change the final morphology and generate internal defects in the ZnO crystal. Thus, a separate doping process is more advantageous to minimize the effects on film growth and uncover doping-dependent changes on the thin film properties[10].

In this study, I develop an innovative approach to form AZO NTs via simultaneous etching and Al doping of H_2O-oxidized ZnO NRs[11]. The transformation to AZO NTs was accomplished via a facile one-step spin-coating process of a methanolic $AlCl_3$ solution on top of the NRs. This novel technique of generating NTs via $AlCl_3$ etching is much faster and efficient compared with conventional methods. Furthermore, the present strategy allows us a flexible doping tunability, and doping effects can be examined separately. The critical role of the doping process and the effect of etching on ZnO NRs were discussed through comprehensive structural, chemical, optical and electrical characterizations. To the best of the author's knowledge, this is the first study to report the Al doping of ZnO NRs and at the same time, the evolution of these NRs to NTs via a one-step process. Finally, the synergistic effect of etching and Al doping of the NRs brought us a potential multifunctional material for solar cells and other optoelectronic devices.

4.2 Experimental

4.2.1 Formation of ZnO NRs by H_2O oxidation

Indium tin oxide (ITO)-coated glass substrates (Luminescence Tech. Corp.) substrates were etched with diluted hydrochloric acid and cleaned via sonication with detergent, ultrapure water, acetone and methanol for 15 min, separately. Then, the substrates were treated with UV/O_3 for 10 min to remove organic impurities. Before depositing Zn thin films, a 0.50 M zinc acetate ($Zn(CH_3COO)_2$, Wako) in methanol: H_2O (10:1) solution was spin-coated onto the substrates at 5000 rpm for 30s. The films were dried first at 100 °C for 15 min and then annealed at 200 °C for 30 min to form ZnO seed layer. Zn thin films were then thermally evaporated (JEOL JEE-400) on top of ZnO seed layer at a base pressure of $4x10^{-4}$ Pa. The Zn thin films were subsequently immersed in ultrapure water at 90 °C for 8 h to obtain ZnO NRs.

4.2.2 Simultaneous Al-Doping and Etching of ZnO NRs

To form Al-doped ZnO NTs, a 150 µL of (50 mM) methanolic solution of aluminum chloride hexahydrate ($AlCl_3 \cdot 6H_2O$, Wako) was spin-coated on top of the ZnO NRs. The amount of Al dopant concentration was controlled by increasing the number of $AlCl_3$

coatings. Then the thermal diffusion treatment was performed by annealing the samples at 300 °C for 1 h on a hotplate inside a N_2-filled glove box.

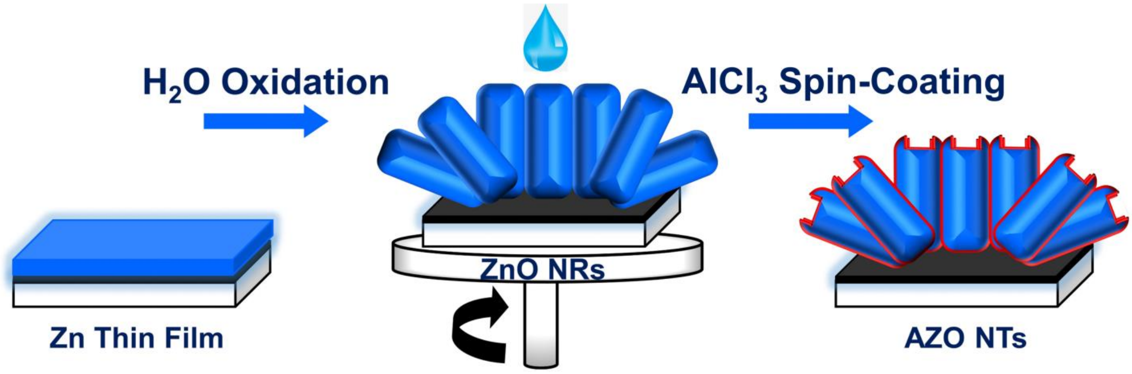

Figure 4.1 Schematic of simultaneous etching and doping of H_2O-oxidized ZnO NRs to form AZO NTs.

4.2.3 Materials Characterization

The morphologies of the samples and energy-dispersive X-ray spectroscopy (EDX) were taken through a low vacuum scanning electron microscope (SEM, Hitachi SU6600 equipped with an EDX system). High-resolution transmission electron microscopy (TEM) images, selected-area electron diffraction (SAED) patterns, and electron energy loss spectroscopy (EELS) elemental mappings were obtained using JEOL JEM-3100FEF operating at 300 kV. The sample for TEM measurement was prepared by dry adhesion of the AZO NTs on a copper grid. The crystallinity and phase composition of the samples were studied using a Rigaku X-ray diffractometer (RINT-TTR III) with CuK_α radiation (λ= 1.5418 Å). Raman scattering measurement was performed at room temperature using a Raman Spectrometer (JASCO NRS-4100). The optical transmission and absorption spectra of the films were measured on a UV-Vis spectrophotometer (JASCO V-530). PL spectra were obtained under ultraviolet excitation (λ_{ex} = 365 nm) using high-pressure mercury-vapour light source (Olympus BH2-RFL-T3) coupled with a microscope (Olympus BX51) and a CCD spectrometer (Hamamatsu PMA-12). The surface chemistry of the films was further investigated using X-ray photoelectron spectroscopy (XPS, PHI5000 VersaProbeII, ULVAC-PHI) at room temperature with Al-Kα radiation (1486.6 eV). Charging effects on the binding energies were corrected with respect to the C 1s peak (284.6 eV). Electron-transporting property was examined by using a space-charge limited current (SCLC) model based on electron-only devices with a configuration of ITO/ZnO or AZO/PCBM/Ag. Current-voltage (J-V) curves were recorded from a Keithley 2611B System Source Meter unit (Bunko-keiki, CEP-2000RP).

4.3 Results and Discussion

4.3.1 Morphological and Structural Properties

Initially, Zn thin film with a thickness of 100 nm was deposited on top of ZnO seed layer/ITO-glass substrate using thermal evaporation. Then, the samples were H_2O-oxidized at 90 °C for 8 h to convert the Zn nanoplatelets into ZnO NRs (Figure 4.2(a)), completely, as depicted in Figure 4.1. Herein, as the oxidation of metallic Zn takes place in H_2O, OH^- ions are also being released from the reduction of dissolved oxygen and H_2O. These OH- ions would then react with Zn^{2+} ions to form ZnO crystals. An in-depth discussion of the growth mechanism of nanostructured ZnO films via H_2O oxidation can be read in our previous works[12, 13].

Figure 4.2 shows the SEM images and the corresponding EDX measurements of the ZnO NRs and AZO NTs formed after the $AlCl_3$ coatings. Note that the H_2O-oxidized ZnO NRs have a mean diameter of ~ 100 nm and a thickness of ~250 nm. The NRs are seen to be fairly aggregated, forming microparticles. Consequently, a methanolic solution of $AlCl_3 \cdot 6H_2O$ was spin-coated on top of the ZnO NRs to realize the simultaneous etching and Al doping to obtain AZO NTs. The Al content in the AZO films was adjusted through the deposition of $AlCl_3$ coatings. The doped samples are denoted as AZO-1, AZO-2 and AZO-3, indicating the number of coatings applied. Surprisingly, the tips of each NRs were slightly etched and their walls became rough after one coating of $AlCl_3$, as shown in Figure 4.2(b). The appearance of wall corrugation indicates that the NRs have a layer-stacked structure. Figure 4.2(c) shows that the addition of another $AlCl_3$ coating further etched the NRs leading to the development of honeycomb-like structures.

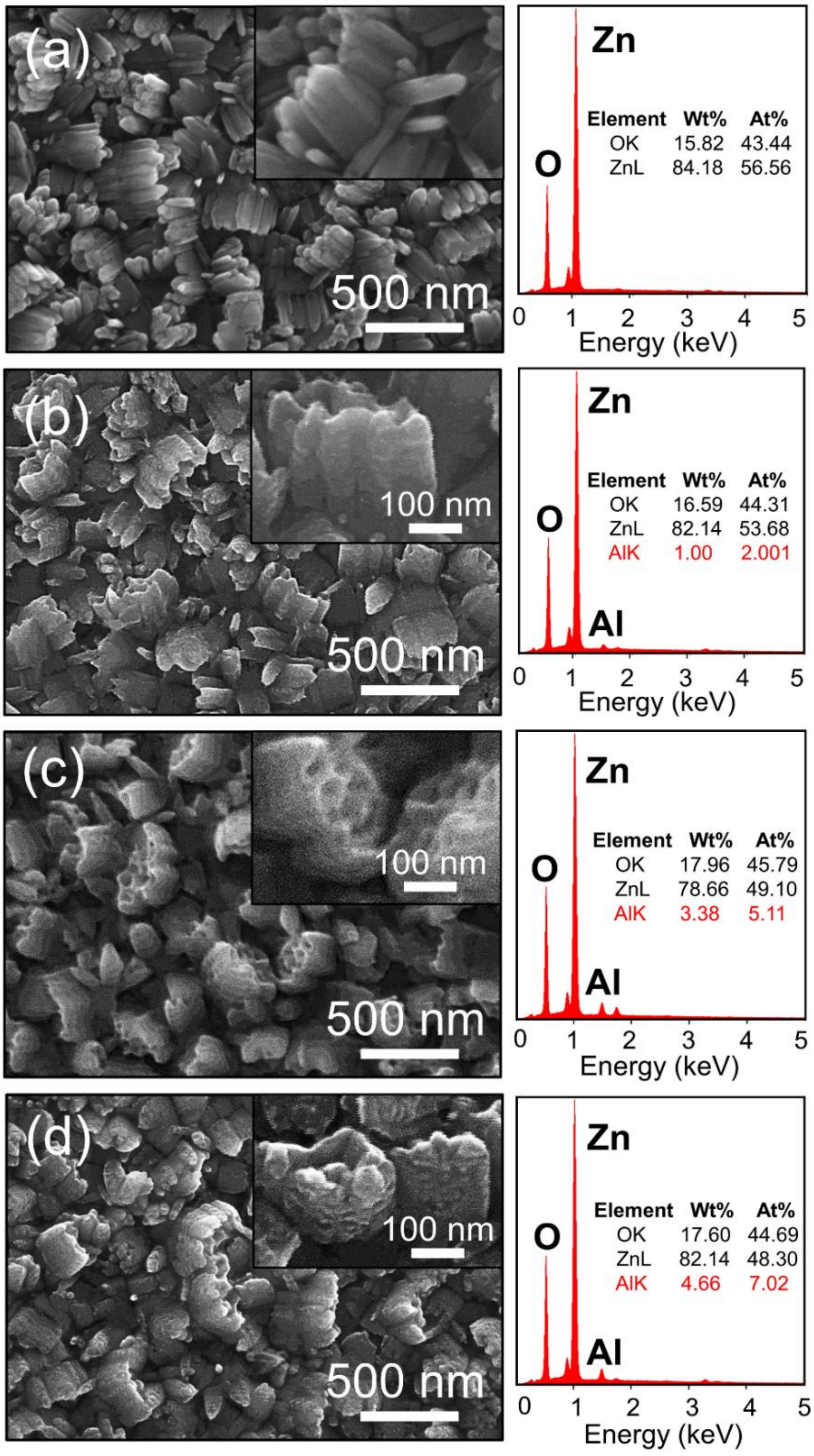

(a)

Element	Wt%	At%
OK	15.82	43.44
ZnL	84.18	56.56

(b)

Element	Wt%	At%
OK	16.59	44.31
ZnL	82.14	53.68
AlK	1.00	2.001

(c)

Element	Wt%	At%
OK	17.96	45.79
ZnL	78.66	49.10
AlK	3.38	5.11

(d)

Element	Wt%	At%
OK	17.60	44.69
ZnL	82.14	48.30
AlK	4.66	7.02

Figure 4.2 SEM images of (a) ZnO NRs formed after H_2O oxidation at 90 ℃ for 8 h and AZO NTs formed after (b) 1, (c) 2, and (d) 3 $AlCl_3$ coatings.

Finally, complete dissolution of the walls separating each NR occurred and the honeycomb-like structures collapsed into larger NTs after three coatings, as shown in Figure 4.2(d). The outer surfaces of the bigger NTs are now visibly rougher with an average inner diameter of ~ 200 nm. Interestingly, the NTs formed were successfully doped with Al based on their EDX measurements. The EDX results revealed that the coated samples were composed of Zn, O and Al, and the concentrations of Al are about 2.00, 5.11 and 7.02 at% for AZO-1, AZO-2 and AZO-3 samples, respectively.

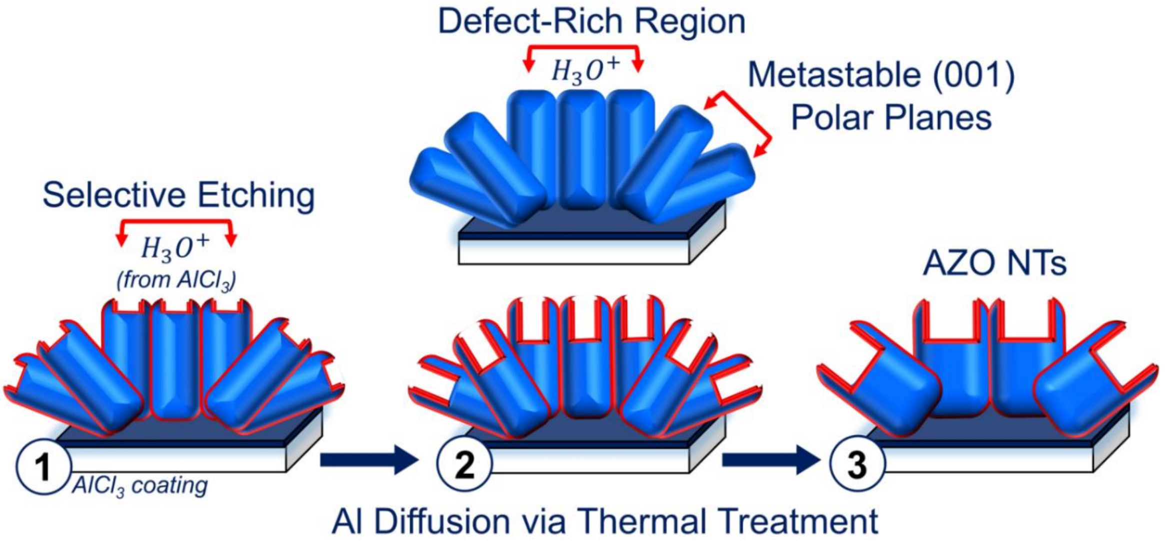

Figure 4.3 Proposed growth mechanism of AZO NTs via simultaneous etching and doping of ZnO NRs.

The growth mechanism of this development of AZO NTs from ZnO NRs can be partially described through the well-known selective etching process, as shown in Figure 4.3. As the $AlCl_3 \cdot 6H_2O$ is dissolved in methanol, H_3O^+ ions are released in the solution as shown in equation 1:

$$[Al(H_2O)_6]^{3+}{}_{(aq)} + H_2O_{(l)} \rightarrow [Al(H_2O)_5OH]^{2+}{}_{(aq)} + H_3O^+{}_{(aq)} \qquad (1)$$

Then, the top polar planes of ZnO NRs react with these H_3O^+ ions resulting in the selective dissolution along their c-axis as in equation 2:

$$ZnO + H_3O^+{}_{(aq)} \rightarrow Zn^{2+}{}_{(aq)} + OH^-{}_{(aq)} + H_2O_{(l)} \qquad (2)$$

Accordingly, the thermal annealing employed after the spin-coating process triggered the diffusion of Al dopant within the film and finally generated the AZO NTs. The selective etching mechanism that has taken place here is also consistent with the discussions reported on the growth of other hollow structures[14]. Since no catalysts or other secondary reagents were combined with the $AlCl_3$ solution, the selective etching could be associated with the preliminary crystal structure of ZnO NRs. It is well-established that the wurtzite ZnO crystal has high surface energy and metastable polar planes such as its top (001) plane. On the other hand, its nonpolar lateral planes are the most stable having lower surface energies, while the central inner part of ZnO NRs is known to be a defect-rich region[15]. Thus, etching is thermodynamically favored to start on the top central (001) plane and would continue along the defect-rich *c*-axis region of ZnO NRs. Also, the presence of minor wall corrugation on the NTs proves that the etching rate on the nonpolar lateral planes is slower than the top polar planes.

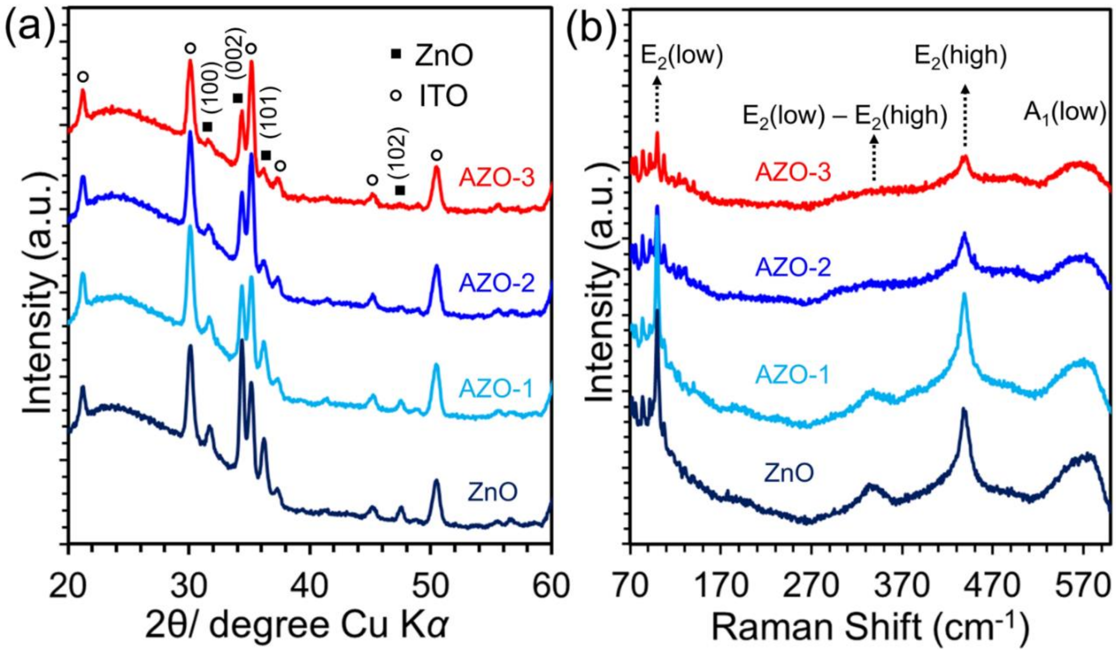

Figure 4.4 (a) XRD patterns and (b) Raman spectra of ZnO NRs and AZO NTs.

Figure 4.4(a) shows the XRD patterns of ZnO NR and AZO NT samples. All XRD profiles with sharp diffraction peaks which correspond to hexagonal wurtzite crystal structure clearly demonstrate that all the samples possess good crystallinity. A significantly higher intensity is observed for the (002) diffraction peak, which indicates that the nanostructures are oriented with their c-axis being relatively perpendicular to the ITO/glass substrates. No diffraction peaks of Al_2O_3 or any additional impurities were detected in the Al doping concentration range considered in this work, except for the underlying ITO substrate. Overall, it can be seen that the intensity of ZnO peaks gradually decreases, which is more noticeable for the (002) peak due to the formation of NTs during the doping process.

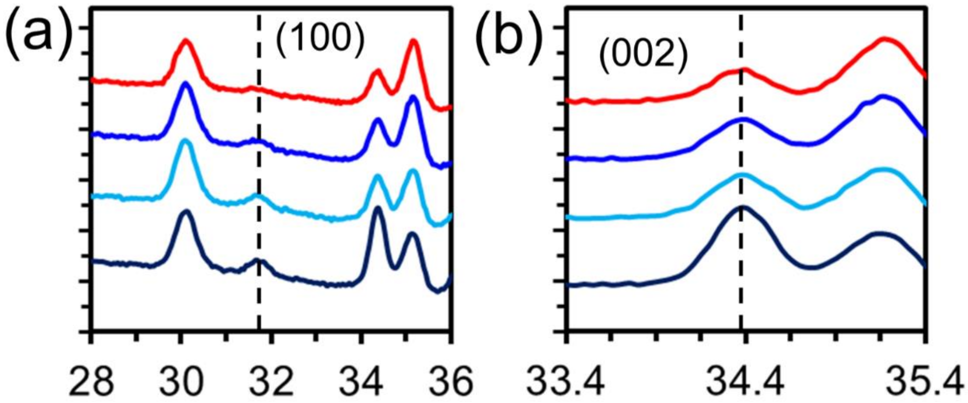

Figure 4.5 XRD patterns of ZnO NRs and AZO NTs magnified at (100) and (002) diffraction peaks.

Additionally, the (100) peak shifted to lower θ values signifying an increase in the lattice constant "a" and the (002) peak slightly shifted to higher θ values indicating a decrease in the lattice constant "c". As Al doping and etching of ZnO NRs commence, the wurtzite crystal structure becomes shorter and wider at the base and the overall cell volume ($\propto a^2c$) slightly increases (Figure 4.5). These changes in lattice parameters suggest the successful introduction of smaller Al dopants into the Zn^{2+} sites.

Moreover, the HRTEM image taken near the tip of the NT shows that the AZO-3 sample is highly crystalline with a lattice spacing of about 0.263 nm, corresponding to the distance between the (002) planes in the ZnO crystal lattice. This also shows that the NTs retain the growth orientation of the initial ZnO NRs after the simultaneous etching and doping process. Notably, no part of the NT with interplanar spacings close to those of Al_2O_3 was found, further validating the incorporation of Al into the ZnO matrix without the formation of Al_2O_3. The sharp and clear diffraction spots from the SAED pattern of the AZO-3 NT (Figure 5(c)) also prove that it is single crystalline in nature. The EELS elemental mapping images of the Al, Zn, and O elements based on the TEM image of the AZO-3 NT, are shown in Figure 5(d)-(f), respectively. The mapping analysis confirmed the presence and homogenous distribution of the Al dopant as well as the Zn and O elements over the entire surface area of the NT.

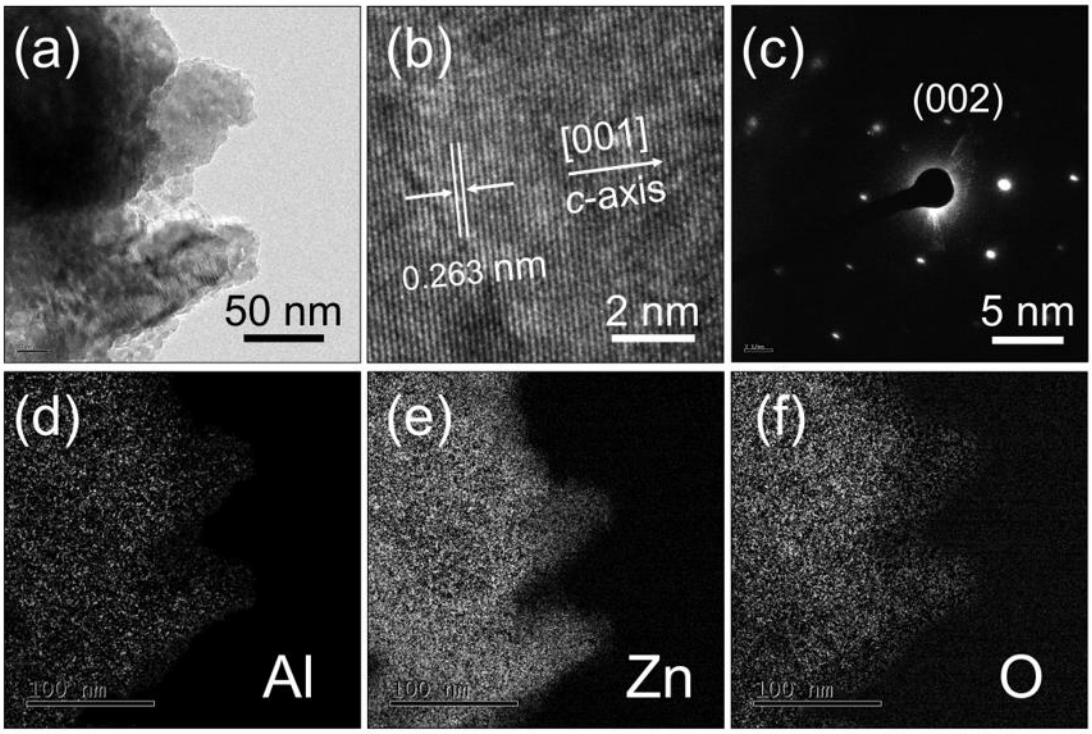

Figure 4.6 (a) TEM, (b) HRTEM images and (c) SAED pattern of an individual AZO-3 NT. Images (d)-(f) are its corresponding EELS elemental mapping.

It is also known that the vibrational properties of solids are linked to the long and short-range orders in the crystal lattice[16]. Raman spectroscopy is implemented to investigate the effect of simultaneous etching and doping process on the vibrational properties of the AZO NTs. Figure 4.4(b) shows the room temperature Raman spectra of the all the samples under excitation of a 532 nm laser line. One of the most intense modes in the Raman spectra is a very narrow E_2^{low} peak at ~ 100 cm^{-1}, which is associated to the vibrations of Zn sublattice of ZnO. Another intense Raman peak is E_2^{high} at ~ 439 cm^{-1}, which is dominantly assigned to the oxygen vibrations[17]. These two sharp E_2 peaks further verified the highly crystalline nature of all the samples. The peak at 331 cm^{-1}, which can be seen for ZnO NRs and AZO-1 samples only, is a second-order Raman mode ascribed to the difference between the E_2^{high} and E_2^{low} modes. The broad peak around 575 cm^{-1} can be assigned to the E_1(LO, longitudinal optical) mode, which is caused by defects such as oxygen vacancies (V_O) and zinc interstitials (Zn_i) [18]. Furthermore, the Raman peaks were noticeably reduced and became broader as Al dopant is increased. This could be related to the dopant inclusion in the ZnO lattice which leads to stress formation and eventually deterioration of the ZnO crystal.

4.3.2 Chemical State on the Surface

XPS measurements were done to track the changes in the elemental composition and chemical binding environment of the surface atoms of ZnO NRs and AZO NTs, as shown in Figure 4.7. The photoelectron peaks corresponding to the Zn, O and C elements can be clearly seen on the XPS survey spectra, as illustrated in Figure 4.7(a). A small peak designated to Al dopant is also visible from the survey spectra of AZO NTs. The C element peak located at ~ 284.6 eV may be caused by adsorbed CO_2 from air. The high-resolution Zn-2p XPS spectra (Figure 4.7(b)) of the samples present two major peaks centered at 1021.6 and 1044.6 eV corresponding to the $\mathrm{Zn}2p_{3/2}$ and $\mathrm{Zn}2p_{1/2}$ states, respectively. In addition to the absence of the metallic Zn, a spin-orbital splitting of 23.0 eV establishes that most of the Zn elements exhibit positive divalent oxidation state (Zn^{2+}) [19]. The Zn-2p peaks of AZO NTs slightly shifted to higher binding energies due to chemical shift and possibly band bending. However, Viter et al. reported the band bending in ZnO at the interface between ZnO and Al_2O_3 is significantly small[20], thus, band bending effect could be eliminated.

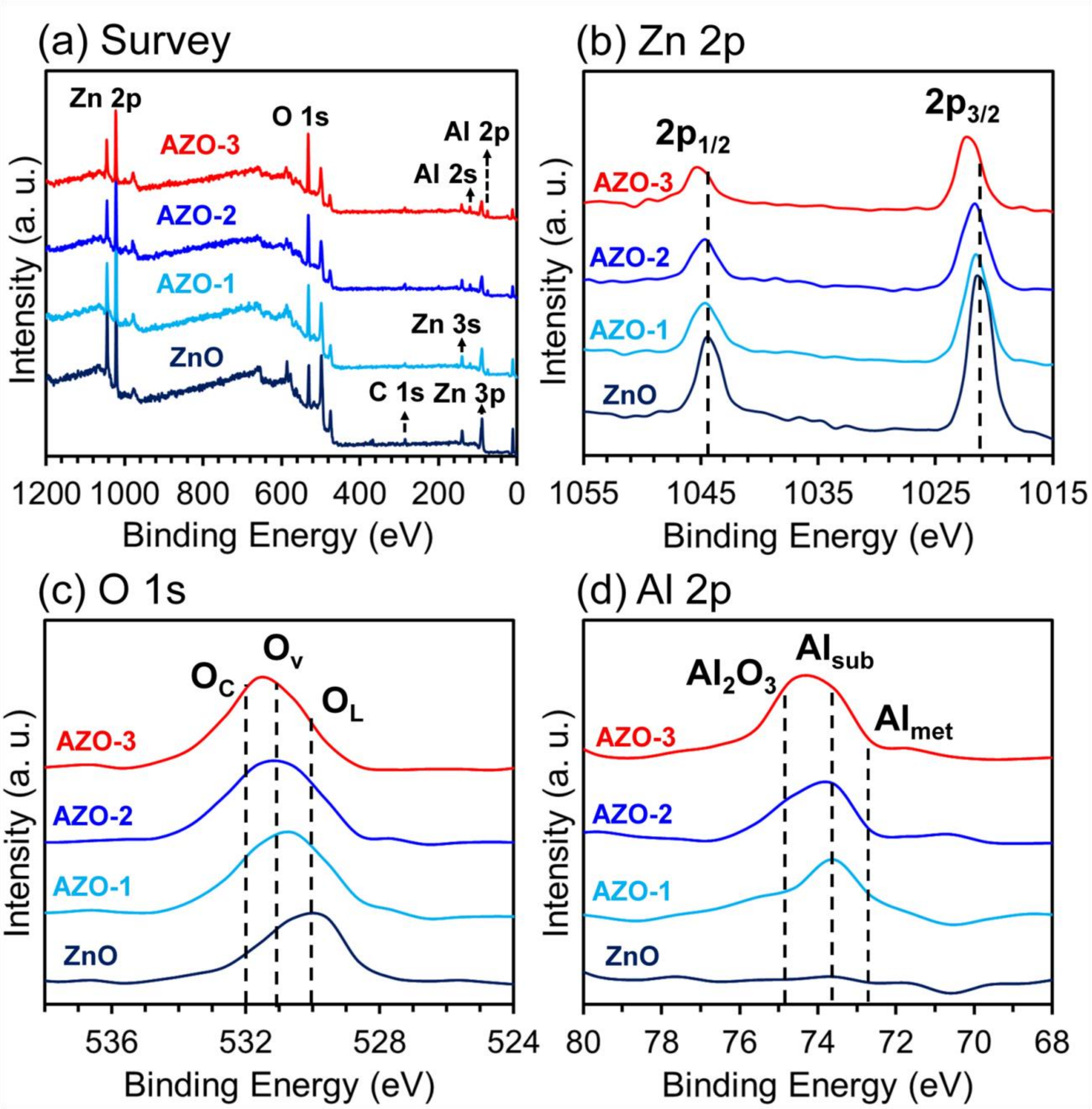

Figure 4.7 (a) XPS survey spectra and high-resolution XPS spectra of (b) Zn 2p, (c) O 1s and (d) Al 2p of ZnO NRs and AZO NTs.

The reduced intensity peaks for doped samples are in agreement with the selective etching process that led to a decrease in ZnO concentration and generation of NTs. Since the O1s core level spectra are remarkably sensitive to the Zn-O chemical bonds, the XPS O1s spectra shown in Figure 4.7(c) are used for analyzing the compositions of the ZnO NRs and

AZO NTs. The high-resolution O1s spectra of the samples are shown to have three different components centered at 530.3 eV, 531.0 eV and 531.9 eV, respectively, as indicated in Figure 4.7(c). The higher binding energy component (O_C) located at 531.9 eV is generally ascribed to chemisorbed oxygen species adsorbed on the chemically active surface and grain boundaries of the nanostructured films[21]. The medium binding energy O_V peak, centered at 531.0 eV, is associated with O^{2-} in oxygen-deficient sites within the ZnO matrix and/or ZnO surface imperfections[22]. The low binding energy O_L peak located at 530.3 eV is attributed to O^{2-} ions in the wurtzite ZnO, which are surrounded by Zn or substitutional Al atoms[23]. Notice that the O1s spectra of AZO NTs are centered on the O_V peak demonstrating that doped samples have significant amount of oxygen vacancies. The production of oxygen vacancies can be linked to the free competitive growth between the Zn-O and new Al-O bonds on the surface, as the Al dopant is replacing the Zn site in the ZnO lattice[24]. In addition, the thermal treatment of the samples in an oxygen-deficient (N_2) atmosphere and the transformation of NRs to NTs with larger surface area promote the creation of additional oxygen vacancies.

From the typical Al 2p spectra shown in Figure 4.7(d), the appearance of Al 2p peak centered at 73.7 eV in AZO NTs further demonstrate that the Al doping have successfully taken place into the original ZnO lattice through substitution of Zn^{2+} sites. Specifically, this binding energy is almost identical with the reported values (Al 2p: 73.9 eV) [25] with oxidation state close to +3 as well as higher than metallic Al (Al 2p: 72.8 eV) and lower than the Al_2O_3 (Al 2p: 74.8 eV) [26]. Moreover, a further shift to higher binding energies close to that of Al_2O_3 can be seen on the Al 2p spectrum of AZO-3 NTs. This shift can be attributed to Al segregation at the grain boundaries forming Al_2O_3, possibly as a result of Al exceeding its solubility limit in the AZO film[27]. As stated earlier, this Al_2O_3 was not detected in XRD; hence, it is most likely amorphous and low in concentration. Furthermore, this generation of

Al_2O_3 increases the size of the grain boundary barriers that might affect the resulting electrical properties of AZO-3 sample.

4.3.3 Optical and Defect Properties

The transparency is an important factor for both TCO and electron-transporting material application; thus, the optical transmission was measured by a UV-vis spectrometer for ZnO NRs and AZO NTs with various Al concentrations as shown in Figure 4.8(a). All the samples are found to be highly transparent (~ 80%) in the range of 500-900 nm. This result demonstrates the excellent optical compatibility of AZO NTs as an electron-transporting and transparent electrode material for applications in solar cells and other optoelectronic devices. Notice that the transmittance of the samples improved by $AlCl_3$ coatings are increased. This could be ascribed to the reduced ZnO concentration after the etching process. At the same time, when the Al content was increased from 0 to 7.02 at%, the absorption edge of the AZO NTs shifted to shorter wavelengths indicating band gap (E_g) broadening.

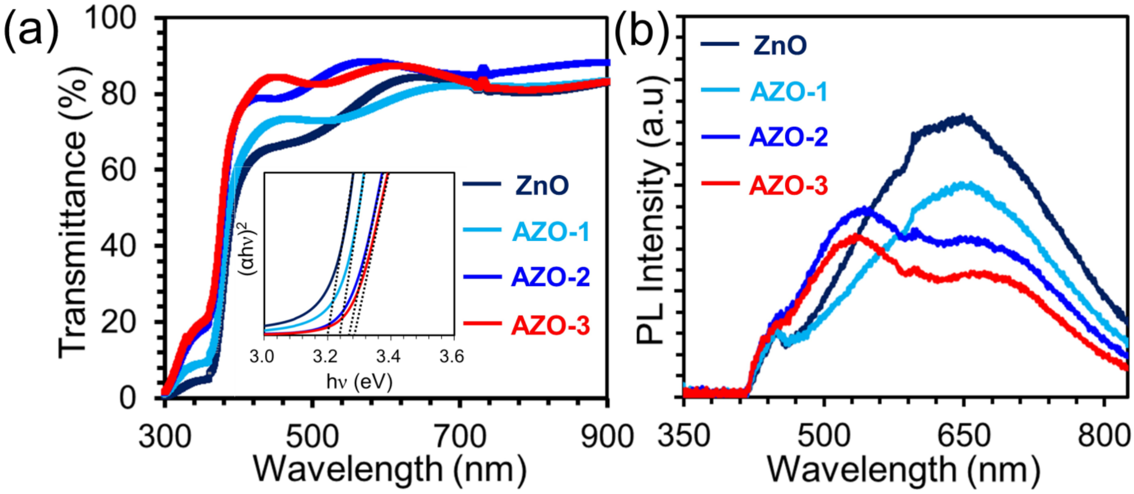

Figure 4.8 (a) Optical transmission and (b) room temperature photoluminescence spectra of ZnO NRs and AZO NTs.

The optical band gap derived from Tauc plot $[(\alpha h\nu)^{\frac{1}{2}}\ vs.\ eV)]$ are shown in the inset of Figure 4.8(a). It was found that the band gap of ZnO NRs changed from 3.20 to 3.24, 3.26 and 3.28 eV for AZO-1, AZO-2 and AZO-3 samples, respectively. The band gap of Al_2O_3 is 8.7 eV, thus, the increase in E_g of AZO samples is to be expected with increasing Al dopant. Moreover, this blue shift in the band gap energy arises due to an increase in charge carrier density in AZO NTs provided from donor sites related with oxygen vacancies or excess metal ions (Moss- Burstein effect)[28]. Based on Moss-Burstein theory, the donor electrons in doped ZnO films occupy states at the bottom of conduction band. Since Pauli's principle forbids a doubly occupied state, the valence electrons now need an additional energy to be excited to higher energy states in the conduction band[29]. Therefore, the optical band gap of AZO NTs is broader than that of undoped ZnO NRs.

Figure 4.8(b) shows the room temperature photoluminescence spectra of ZnO NRs and AZO NTs under an excitation wavelength of 365 nm. As reported in our previous work, H_2O-oxidized ZnO NRs have shown visible emissions including a blue PL centered at 450 nm (2.75 eV) and an orange-red emission located at 650 nm (1.90 eV). The blue emission is commonly reported to originate from the radiative transition of electrons from local interstitial Zn level to the valence band and the transition from the conduction band to the misplaced oxygen defects (O_{Zn}) [30]. On the other hand, the orange-red emission is triggered by deep level oxygen interstitials (O_i) [31]. It is evident that the intensity of orange-red emission is reduced while the blue-emission is retained for AZO-1 sample. The reduction in orange-red emission is due to the presence of Al ions in ZnO matrix which can consume residual oxygen ions and subsequently decreased the concentration of O_i[32]. Additionally, the orange-red emission is quenched further and a green emission centered at 530 nm (2.30 eV) emerged in the PL spectrum of AZO-2 and AZO-3 samples. As described in previous reports, this green emission is due to the radial recombination of photo-generated holes with electrons of singly ionized charged particles in V_O[33]. This result is also in agreement with their high-resolution O1s XPS spectra being centered on the O_V peak signifying the presence of substantial amount of V_O.

4.3.3 Electronic and Charge-Transporting Properties for Solar Cell Devices

In order to determine the influence of Al doping on the conductivity of ZnO films, the devices composed of ITO/ZnO NRs/Au and ITO/AZO NTs/Au are fabricated, and the current-voltage curves are shown in Figure 4.9(a); then the conductivity is calculated by the equation[34]:

$$I = \sigma_0 A T^{-1} V$$

(3)

where A is the area (0.09 cm^2) and T is the average thickness of ZnO NRs or AZO NTs; the calculated conductivities are tabulated in Table 1. It is found that the conductivity is enhanced with increasing Al concentration, specifically, the device based on AZO-2 NTs exhibited the highest conductivity (2.0 × 10^{-2} mS cm^{-1}), which is about a four-fold improvement to that of undoped ZnO NRs (5.32 × 10^{-2} mS cm^{-1}). However, a slight decline in conductivity is observed for AZO-3 NTs having an Al dopant concentration of 7.02 at%.

In addition, the charge-transporting functionality of the AZO NTs were investigated by fabricating devices with a configuration of ITO/ZnO NRs or AZO NTs/PCBM/Ag and the electron mobility is calculated from the space charge limited current (SCLC) method, as described by the Mott-Gurney equation[34]:

$$J = \frac{9}{8}\epsilon_r\epsilon_0\mu_e(\frac{V^2}{L^3}) \quad (4)$$

where J is the current density, ϵ_r is the dielectric permittivity of ZnO (ϵ_r = 3), ϵ_0 is the permittivity of free-space, μ_e is the effective electron mobility, V is the applied voltage of the device, and L is the average thickness of ZnO NRs or AZO NTs.

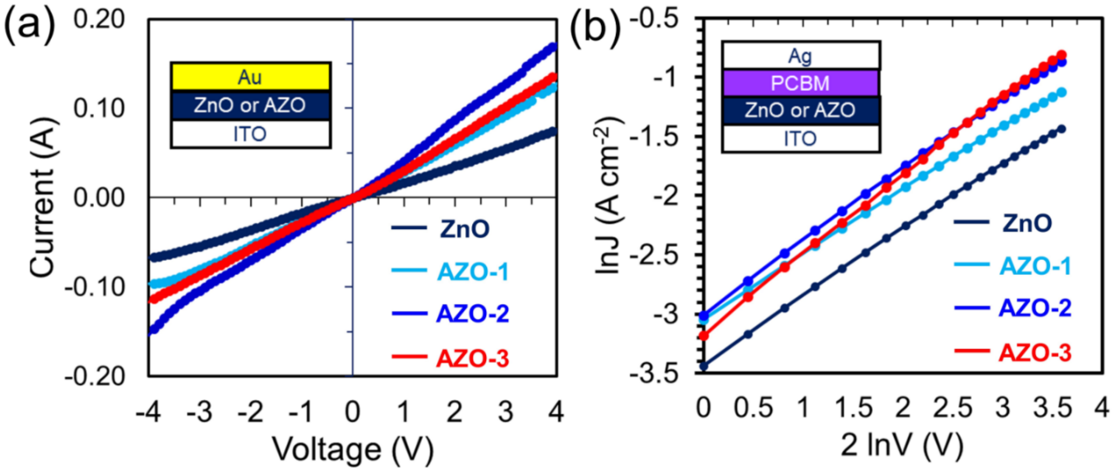

Figure 4.9 (a) *I-V* characteristics and (b) linear fits for the plots of ln *J* vs 2 ln *V* characteristics of the electron-only devices based on ZnO NRs and AZO NTs.

The $\ln J\ vs. 2\ln V$ curves are presented in Figure 4.9(b) and the electron mobilities of the samples are also shown in Table 4.1. The calculated electron mobility for the ZnO NRs is 5.95×10^{-4} cm^{-2} V^{-1} s^{-1}, while 8.78×10^{-4} cm^{-2} V^{-1} s^{-1}, 9.63×10^{-4} cm^{-2} V^{-1} s^{-1} and 7.66×10^{-4} cm^{-2} V^{-1} s^{-1} were calculated for AZO-1, AZO-2 and AZO-3 samples.

Table 4.1 Summary of electrical conductivity and electron mobility values of the electron-only devices based on ZnO NRs and AZO NTs.

Sample	σ_0/mS cm^{-1}	μ_e (cm^2 V^{-1} s^{-1})
ZnO	5.32×10^{-3}	5.95×10^{-4}
AZO-1	8.88×10^{-3}	8.78×10^{-4}
AZO-2	2.08×10^{-2}	9.63×10^{-4}
AZO-3	9.58×10^{-3}	7.66×10^{-4}

Our results for carrier mobilities are consistent with the reported values in the literature[35]. Apparently, the same trend with the electrical conductivity can be deduced for electron mobility, wherein the doped films displayed higher electron mobilities compared with the undoped ZnO NRs. This enhancement in electronic properties of AZO NTs further proves the substitutional replacement of Zn^{2+} ions by Al^{3+} ions which produces charge carriers, as illustrated in this equation[36]:

$$Al_2O_3 \xrightarrow{ZnO} 2Al_{Zn}^{\bullet} + 2O_O^x + \frac{1}{2}O_{2(g)} + 2e^- \tag{5}$$

In this case, Al donates its 3p electron to the conduction band of ZnO resulting in the shift of its Fermi level above the conduction band minimum as a function of dopant concentration. Conversely, when the solubility limit is exceeded, the emergence of Al interstitials eventually occurs despite its higher formation energy, as shown in the following equation[36]:

$$Al_2O_3 \xrightarrow{ZnO} 2Al_i^{\bullet\bullet\bullet} + \frac{3}{2}O_{2(g)} + 6e^- \tag{6}$$

This reaction results in the Al segregation at the grain boundaries and the scattering processes at these defects can lead to an overall degradation of electronic properties, as observed in AZO-3 sample.

In order to assess the overall applicability of AZO NTs in case of practical devices, we examined their electron-transporting capability in perovskite solar cells via steady-state PL analysis. Generally, perovskite films display strong PL quenching in contact with charge-transport layers, as proof of efficient charge transfer from the active layer to the transport layer[37]. Figure 4.10(a) shows the steady-state PL of $CH_3NH_3PbI_3$ films on the following substrates: glass/ITO, glass/ITO/ZnO NRs and glass/ITO/AZO NTs. Clearly, the spectral peaks at around 770 nm related to the intrinsic fluorescence emission of $CH_3NH_3PbI_3$ are quenched by contact with ZnO NRs and AZO NTs, signifying the electron transfer from the perovskite films to the electron-transporting layers.

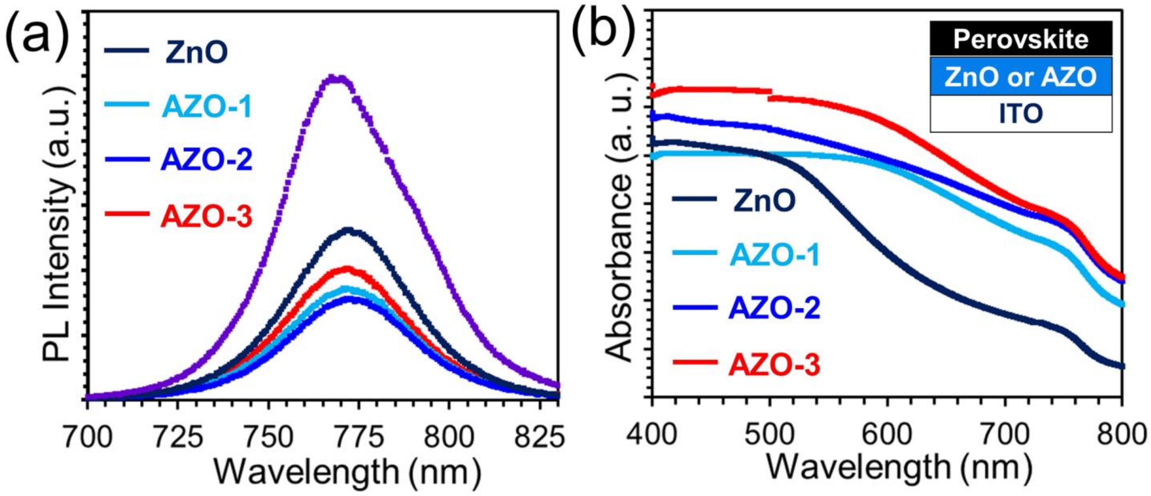

Figure 4.10 (a) Steady-state photoluminescence and (b) absorption spectra of perovskite films on top of ZnO NRs and AZO NTs.

In particular, the AZO-2/perovskite bilayer showed the strongest quenching effect among the samples which implies that the AZO-2 sample is the most efficient in promoting electron transportation/extraction. These results are also in conformity with the electron mobility values. That is, the higher the electron mobility, the higher the electron extraction efficiency. Furthermore, charge recombination is further suppressed using NTs due to their higher surface roughness, which introduced additional electronic contact between them and the perovskite layer. Figure 4.10(b) shows the absorption spectrum of perovskite films on top of ZnO NRs and AZO NTs. The electron-transporting/perovskite bilayers revealed a panchromatic absorption of light. Obviously, the AZO NTs/perovskite samples absorbed more light than the ZnO NRs/perovskite sample due to the larger surface area of the NTs.

4.4 Summary

In summary, we developed a novel way of transforming H_2O-oxidized ZnO NRs into AZO NTs via simultaneous doping and etching process. By simply depositing $AlCl_3$ solution, the NRs can be converted gradually to NTs with higher surface area. The acidic nature of $AlCl_3$ solution caused the selective etching along the *c*-axis of the NRs resulting in the formation of NTs. XRD, Raman, XPS, and EELS elemental mapping analyses confirmed the successful substitution of Zn^{2+} ions by Al^{3+} ions in the ZnO lattice. Moreover, AZO NTs have high-quality single crystalline structure based on HRTEM image and SAED pattern. Improved transmittance and a shift in absorption edge towards lower wavelengths can also be seen in doped films which implies broadened band gap. In addition, room temperature PL exhibited that all the samples exhibited blue and orange emissions; however, the intensity of the latter emission was reduced and a green emission appeared with the increase in Al concentration. The AZO-2 sample displayed the highest electrical conductivity and electron mobility values which could be associated with the increase in charge carriers after the doping process. The steady-state PL intensity of AZO NTs/perovskite films also experienced stronger quenching effect compared with ZnO NR suggesting faster electron extraction. These results illustrate that the synergistic effect of etching and Al doping could create additional surface area and significantly enhance the charge-transport properties of H_2O-oxidized ZnO NRs, which can be applied not only in photovoltaics but also in other optoelectronic devices.

References

(1) H. Wei, H. Gong, Y. Wang, X. Hu, L. Chen, H. Xu, P. Liu and B. Cao, *CrystEngComm,* 2011, **13**, 6065-6070.

(2) K. R. Nandanapalli and D. Mudusu, *ACS Appl. Nano Mater.,* 2018, **1 (8)**, 4083–4091.

(3) M. A. Mahmud, N. K. Elumalai, M. B. Upama, D. Wang, A. M. Soufiani, M. Wright, C. Xu, F. Haque and A. Uddin, *ACS Appl. Mater. Interfaces,* 2017, **9**, 33841−33854.

(4) Y. Geng, L. Guo, S.-S. Xu, Q.-Q. Sun, S.-J. Ding, H.-L. Lu and D. W. Zhang, *J. Phys. Chem. C,* 2011, **115**, 12317−12321.

(5) R. T. Ginting, C. C. Yap, M. Yahaya and M. Mat Salleh, *ACS Appl. Mater. Interfaces,* 2014, **6**, 5308−5318.

(6) A. Puetz, T. Stubhan, M. Reinhard, O. Loesch, E. Hammarberg, S. Wolf, C. Feldmann, H. Kalt, A. Colsmann and U. Lemmer, *Sol. Energy Mater. Sol. Cells,* 2011, **95**, 579− 585.

(7) H. Souissi, S. Jabri, A. Souissi, A. Lusson, P. Galtier, A. Meftah, V. Sallet and M. Queslati, *Mater. Res. Express*, 2018, **5**, 015003.

(8) S. Kohiki, M. Nishitani and T. Wada, *J. Appl. Phys.,* 1994, **75**, 2069−2072.

(9) W. Yang, Z. Liu, D-L. Peng, F. Zhang, H. Huang, Y. Xie and Z. Wu, *Appl. Surf. Sci.,* 2009, **255**, 5669−5673.

(10) Y. Kim and S. H. Kang, *Mater. Lett.,* 2009, **63**, 1065−1067.

(11) C. M. Pelicano and H. Yanagi, *J. Mater. Chem. C,* 2019, **7**, 4653-4661.

(12) C. M. Pelicano and H. Yanagi, *J. Mater. Chem. C,* 2017, **5**, 8059-8070

(13) C. M. Pelicano and H. Yanagi, *Appl. Surf. Sci.*, 2019, **467-468**, 932−939.

(14) L. Vayssieres, K. Keis, A. Hagfeldt and S.-E. Lindquist, *Chem. Mater.,* 2001, **13 (12)**, 4395 −4398.

(15) G. W. She, X. H. Zhang, W. S. Shi, X. Fan, J. C. Chang, C. S. Lee, S. T. Lee and C. H. Liu, *Appl. Phys. Lett.,* 2008, **92**, 053111.

(16) I. Musa, N. Qamhieh and S. Mahmoud, *Results Phys.,* 2017, **7**, 3552-3556.

(17) X. L. Xu, S. P. Lau, J. S. Chen, G. Y. Chen and B. K. Tay, *J. Cryst. Growth,* 2001, **223**, 201−205.

(18) L. Shen, N. Bao, K. Yanagisawa, K. Domen, A. Gupta and C. A. Grimes, *Nanotechnology,* 2006, **17**, 5117– 5123**.**

(19) B. Panigrahy, M. Aslam and D. Bahadur, *J. Phys. Chem. C,* 2010, 114, 11758−11763.

(20) B. J. Lee, H. J. Song and J. Jeong, *Adv. Mater. Sci. Eng.,* 2015, 2015, 1– 5

(21) J. C. C. Fan and J. B Goodenough, *J. Appl. Phys.,* 1977, **48**, 3524.

(22) R. N. Aljawfi and S. Mollah, *J. Magn. Magn. Mater.,* 2011, **323**, 3126−3132.

(23) M. Chen, X. Wang, Y. H. Yu, Z. L. Pei, X. D. Bai, C. Sun, R. F. Huang and L. S. Wen, *Appl. Surf. Sci.,* 2000, **158**, 134−140.

(24) Y. Li, R. Yao, H. Wang, X. Wu, J. Wu, X. Wu and W. Qin, *ACS Appl. Mater. Interfaces,* 2017, **9**, 11711−11720.

(25) S. L. Bai, T. Guo, Y. B. Zhao, R. X. Luo, D. Q. Li, A. F. Chen, C. C. Liu, *J. Mater. Chem. A,* 2013, **1**, 11335.

(26) S. Dhara, K. Imakita, P. K. Giri, M. Mizuhata and M. Fujii, *J. Appl. Phys.,* 2013, **114**, 134307.

(27) D. Potter, I. Parkin and C. Carmalt, *RSC Adv.,* 2018, **8**, 33164-33173.

(28) Y. Imai and A. Watanabe, *J. Mater. Sci.: Mater. Electron.,* 2004, **15**, 743– 749.

(29) A. Bauer, T. Wahl, J. Hanisch and E. Ahlswede, *Appl. Phys. Lett.*, 2012, **100**, 073307.

(30) H. B. Zeng, Z. Li, W. P. Cai, B. Cao, P. Liu and S. Yang, *J. Phys. Chem. B,* 2007**,** **111**, 14311-14317.

(31) D. Liu, Y. Lv, M. Zhang, Y. Liu, Y. Zhu, R. Zong and Y. Zhu, ***J. Mater. Chem. A,*** 2014, **2**, 15377-15388

(32) C. Li, J. Lv, B. Zhou and Z. Liang, *Phys. Status Solidi,* 2012, **209**, 1538.

(33) Y. Jiao, H. J. Zhu, M. J. Zhou, X. F. Wang and Q. Li, *J. Phys. Chem. C*, 2010, **114**, 208–211.

(34) G. Yin, J. Ma, H. Jiang, J. Li, D. Yang, F. Gao, J. Zeng, Z. Liu and S. F. Liu, *ACS Appl. Mater. Interfaces*, 2017, **9**, 10752−10758.

(35) J. Song, E. Zheng, L. Liu, X.-F. Wang, G. Chen, W. Tian and T. Miyasaka, *ChemSusChem*, 2016, **9**, 2640– 2647.

(36) S. Hartner, M. Ali, C. Schulz, M. Winterer and H. Wiggers, *Nanotechnology*, 2009, **20**, 445701.

(37) J. You, L. Meng, T. B. Song, T. F. Guo, Y. Yang, W. H. Chang, Z. Hong, H. Chen, H. Zhou, Q. Chen, Y. Liu, N. De Marco and Y. Yang, *Nat. Nanotechnol.*, 2016, **11**, 75–81.

Chapter 5

Accelerated Growth of Nanostructured ZnO Films via Low Temperature Microwave-assisted H_2O Oxidation for Perovskite Solar Cells

5.1 Introduction

The formation of ZnO by H_2O oxidation involves immersion of Zn thin films in H_2O for several hours using a hot-plate[1]. In our system, H_2O is heated through heat conduction along the walls of the beaker then heat diffuses within the overall solution. This ineffective heating causes an immense loss of energy and non-uniform heating of the system[2, 3]. Subsequently, additional time is usually necessary to achieve the desirable product[4, 5]. Hence, the next logical aim is to improve heating uniformity and at the same time speed up the growth of materials.

Herein, I propose the integration of microwave technology with H_2O oxidation. Microwave heating is a promising synthesis process for nanostructured materials due to its advantages including homogeneous volumetric heating, high reaction rate, and energy savings[6-10]. The heating mechanism comprises two major processes, namely dipolar polarization and ionic conduction, as illustrated in Figure 5.1[11]. Microwave irradiation of a sample leads to the continuous realignment of the dipoles (Figure 5.1(a)) or ions (Figure 5.2(b)) in the oscillating electric field. Then different amounts of heat are created through molecular friction and dielectric loss which depend on the time scales of the orientation and disorientation occurrence relative to the frequency of the irradiation.

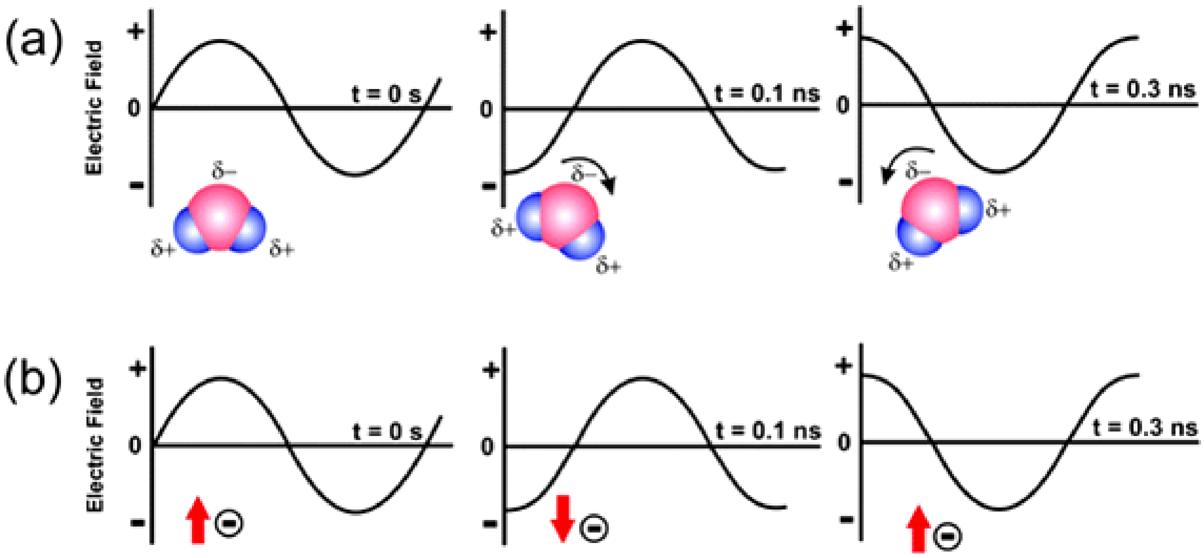

Figure 5.1 Two main heating mechanisms under microwave irradiation: (a) dipolar polarization; (b) ionic conduction mechanism. Reproduced with permission[11]. Copyright 2009, Wiley-VCH.

Several studies have already reported microwave-assisted growth of ZnO NSs[12-21]. Cho et al. described a chemical method to synthesize ZnO having basic to complex structures using a fast, simple and low-temperature microwave-assisted hydrothermal method. They used different types of Zn ($Zn(NO_3)_2{\cdot}6H_2O$, $Zn(CH_3COO)_2{\cdot}2H_2O$) and OH^- (hexamethylenetetramine (HMT), NH_3) precursors as well as several capping agents (Ethylenediamine (EDA), triethyl citrate) in order to generate various structures[22]. Krishnapriya et al. reported a one-pot rapid microwave assisted solvothermal method to fabricate ZnO for dye-sensitized solar cells. Diverse ZnO morphologies such as calendula flower like and rice-grain-shape like nanoparticles (NPs) were obtained from the decomposition of $Zn(OH)_4^{2-}$/$Zn(NH_3)_4^{2+}$ precursors in different solvents such as H_2O, ethylene gycol (EG) and ethanol (EtOH)[23]. However, these microwave-assisted synthesis techniques still require chemical solvents and capping agents which serve as impurities and increase production cost. Therefore, the combination of microwave technology with H_2O oxidation would lead to a facile, low cost, environmental-friendly and ultrafast formation of nanostructured ZnO. By employing H_2O as a dipolar solvent, heat can be generated via rotation, friction, and collision of H_2O molecules with each other under the influence of a rapidly changing alternating electric field. Simultaneously, the dissolved (Zn^{2+} and OH^-) ions in the system diffuse and collide continuously triggering a sudden rise in the local temperature due to Joule heating[24]. Then, as the temperature rises, the energy transfer will be more efficient and Zn oxidation can be facilitated. In particular, this study is the first to report a microwave-assisted synthesis of metal oxide nanostructures (NSs) using only pure H_2O and a metal film. This novel and sustainable method could revolutionize materials synthesis field for technological applications such as solar cells.

5.2 Experimental

5.2.1 Formation of Nanostructured ZnO Films by Microwave-Assisted H_2O Oxidation

Firstly, indium tin oxide (ITO)-coated glass substrates (Luminescence Tech. Corp.) substrates were cleaned separately with detergent, ultrapure H_2O, acetone and methanol for 15 min. Subsequently, the substrates underwent UV/O_3 treatment for 10 min to eliminate organic impurities. Prior to the deposition of Zn thin films, a 0.50 M zinc acetate ($Zn(CH_3COO)_2$, Wako) in methanol:water (10:1) solution was spin-coated onto the substrates at 5000 rpm for 30s. The films were dried first at 100 °C for 15 min and then annealed at 200 °C for 30 min to form a compact ZnO layer, which served as a seed layer. This was followed by thermal evaporation (JEOL JEE-400) of Zn thin films on top of the ZnO seed layer at a base pressure of 4 x 10^{-4} Pa. The Zn thin films were consequently immersed inside a beaker filled with ultrapure H_2O (400 ml) and placed inside a commercial microwave oven (2.45 GHz, Iris Oyhama), as shown in Figure 5.2. It should be noted that the substrates were fixed with double-sided tape at the bottom of the beaker for stabilizing the growth of the nanostructures. To determine the influence of irradiation time, the samples were irradiated at 500 W for 0.5-2 h. After microwave processing, the system was cooled down to room temperature to prevent thermal shock. Then the samples were washed with ultrapure H_2O and dried at 100 °C on a hotplate.

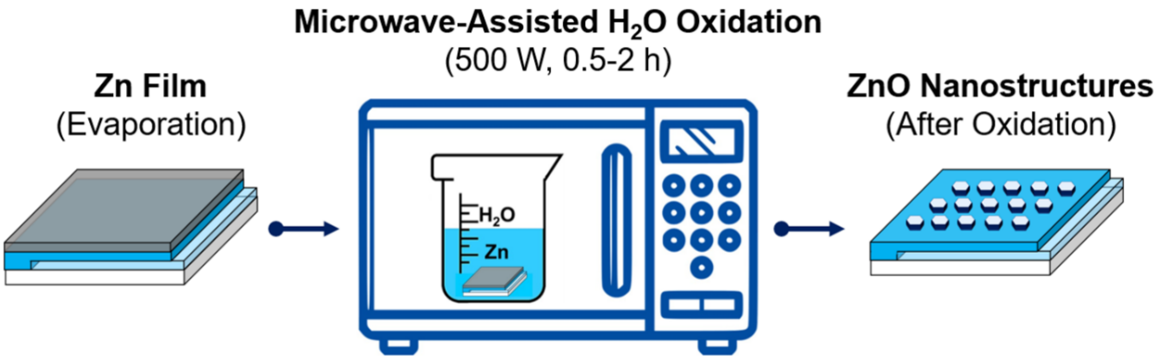

Figure 5.2 Schematic of microwave-assisted H_2O oxidation of Zn thin films to form nanostructured ZnO films.

5.2.2 Materials Characterization

The surface and cross-sectional morphologies of the samples were taken using a low vacuum scanning electron microscope (SEM, Hitachi SU6600). The roughness of the nanostructured ZnO films was analyzed by an atomic force microscope (AFM, Seiko SPA-400 using Olympus SI-DF20 Probe) in tapping mode. AFM images were taken in air by scanning an area of 5x5 µm with a scan rate of 0.60 Hz. High-resolution transmission electron microscopy (TEM) images, nano-beam diffraction (NBD) pattern, and electron energy loss spectroscopy (EELS) elemental mappings were obtained from a JEOL JEM-3100FEF with operating voltage of 300 kV. The sample for TEM measurement was prepared by dry adhesion of the nanostructured ZnO films on a Cu grid. The crystallinity and phase composition of the samples were studied using a Rigaku X-ray diffractometer (RINT-TTR III) with CuK_α radiation (λ= 1.5418 Å). Raman scattering measurement was performed at room temperature using a Raman Spectrometer (JASCO NRS-4100). X-ray photoelectron spectroscopy (XPS, PHI5000 VersaProbeII, ULVAC-PHI) analyses were carried out at room temperature with Al-Kα radiation (1486.6 eV). The binding energy values were adjusted for charging effects by assigning a position of 284.6 eV to the C 1s signal arising from adventitious contamination.

5.3 Results and Discussion

5.3.1 Morphological and Structural Properties

The influence of irradiation time on the resulting nanostructured ZnO films after microwave-assisted H_2O oxidation is shown in SEM and AFM images in Figure 5.3. Their corresponding cross-sectional images are shown as inset. First, a compact layer made of ZnO NPs was spin-coated on glass/ITO substrates. This layer functions as a nucleation point for the Zn thin film. Subsequently, the oxidation of Zn thin films was done through rapid heating under microwave irradiation. The increase in the temperature is specifically brought by the dipole polarization of H_2O molecules and the ionic conduction of dissolved ions (Zn^{2+},OH^{-}) in the system. Figure 5.3(a) shows that the Zn nanoplatelets evolved uniformly into ZnO nanorods (NRs) after 0.5 h of microwave-assisted H_2O oxidation. The ZnO NRs have diameters ranging from 40-100 nm and can be seen to be aggregated creating wider NRs. Moreover, the 0.5 h-ZnO sample has an average thickness of ~ 350 nm and a surface roughness of 7.16 nm. It should be noted that H_2O oxidation process can easily form rod-like structures without the presence of any catalysts, surfactant or ligands[1]. This could be associated to the well-established reconstruction of metastable and high surface energy-polar (001) plane of ZnO crystal[25]. The negatively charged O^{2-}-terminated $(00\bar{1})$ plane is anticipated to adsorb onto the Zn^{2+} terminated (001) plane of the existing ZnO layer, steering the development of 1D ZnO NRs. This finding also verifies that the microwave irradiation can significantly accelerate the crystal growth of ZnO nanostructures compared with the conventional H_2O oxidation which needed 8 h to generate NRs.

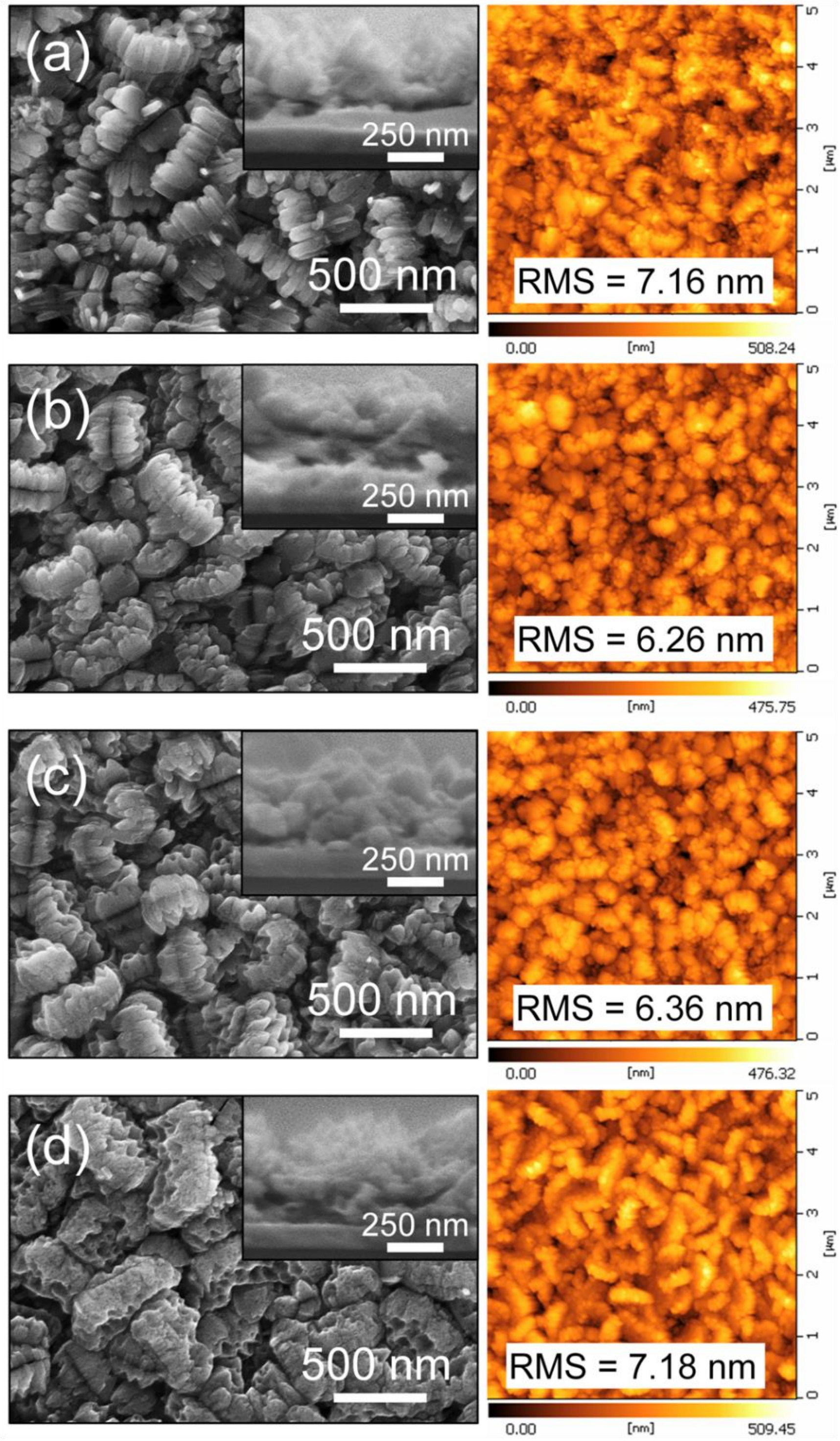

Figure 5.3 SEM and AFM images of nanostructured ZnO films formed after microwave-assisted H_2O oxidation for (a) 0.5, (b) 1, (c) 1.5 and (d) 2 h. Inset: Corresponding cross-sectional SEM images.

Shibata et al. found out experimentally that the activation energy of a reaction is reduced by microwave irradiation. They assumed that an increase in probability of collisions between molecules by rapid rotation of dipoles or ions would lead to enhanced reaction velocity and reduction of activation energy[26]. In the present case, the presence of microwave and violent boiling of H_2O possibly led to the lower activation energy for ZnO nucleation. In turn, faster nucleation and crystal growth proceeded within the system. Additionally, increasing the irradiation time to 1 h initiated the conversion of flat-topped NRs to pointed NRs, as shown in Figure 5.3(b). The thickness of the 1 h-ZnO sample slightly increased to ~ 380 nm with a reduced surface roughness of 6.26 nm. When the irradiation time was increased to 1.5 h, pointed NRs are still visible but a number of them have already transformed to nanotubes (NTs) (Figure 5.3(c)), which is possibly due to the inherent selective etching process taking place along the (001) plane of each ZnO crystal as oxidation proceeds[27]. The 1.5 h-ZnO sample has almost similar RMS and thickness as with 1 h-ZnO sample due to their identical morphology. Figure 5.3(d) shows that all the pointed ZnO NRs are fully converted into NTs with rougher outer wall surface by extending the irradiation time to 2 h. This rough surface could be attributed to the violent collisions of ZnO molecules within the system as oxidation process is prolonged. The 2 h-ZnO sample has a reduced thickness of 350 nm with higher surface roughness of 7.18 nm.

The proposed growth mechanism of the microwave-assisted H_2O-oxidized ZnO nanostructures from Zn thin film is schematically depicted in Figure 5.4 based on the morphological observations. Zn^{2+}ions are produced from the oxidation reaction at oxygen-poor areas of Zn nanoplatelets as in eqn (1):

$$Zn_{(S)} \rightarrow Zn^{2+}_{(aq)} + 2e^{-} \qquad (1)$$

At the same time, dissolved oxygen and H_2O consume electrons from Eqn (1) to discharge OH^- ions through the following reduction reactions (eqn (2) and (3)):

$$2H_2O_{(l)} + 2e^- \rightarrow H_2 + 2OH^- \qquad (2)$$

$$O_{2(g)} + 2H_2O_{(l)} + 4e^- \rightarrow 4OH^- \qquad (3)$$

These OH^- ions would now react with Zn^{2+} ions to precipitate ZnO crystals in the presence of microwave irradiation as shown in eqn (4):

$$Zn^{2+}_{(aq)} + 2OH^-_{(aq)} \xrightarrow{MW} ZnO + H_2O \qquad (4)$$

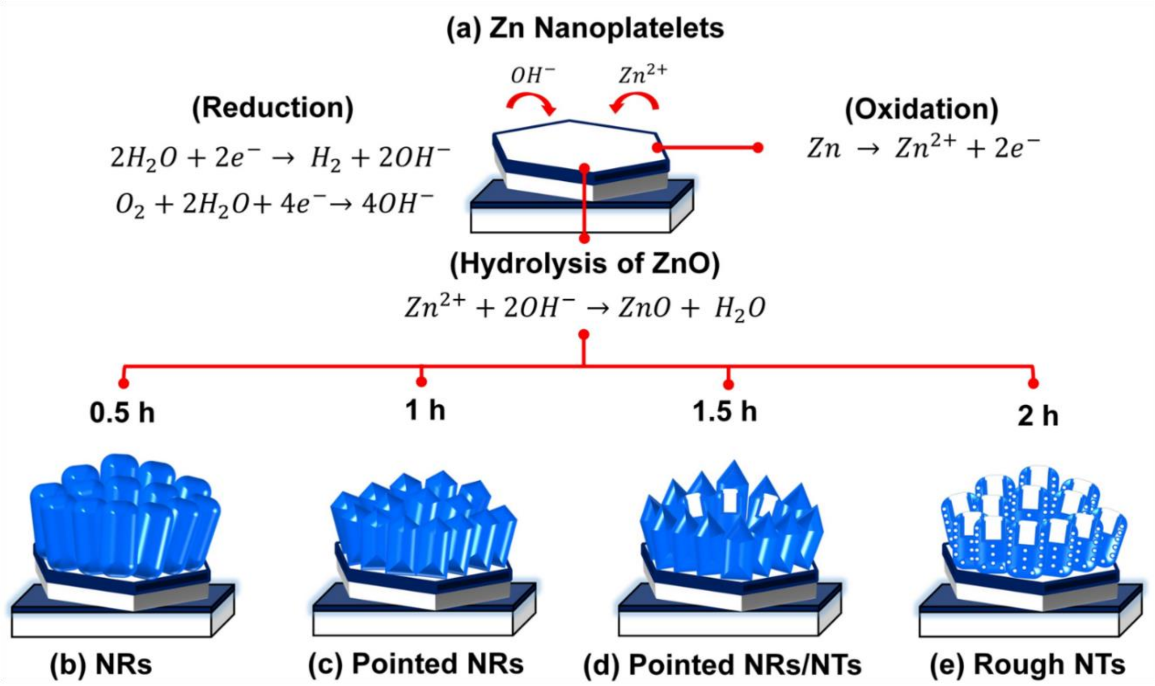

Figure 5.4 Growth mechanisms of ZnO NSs via microwave-assisted H_2O oxidation.

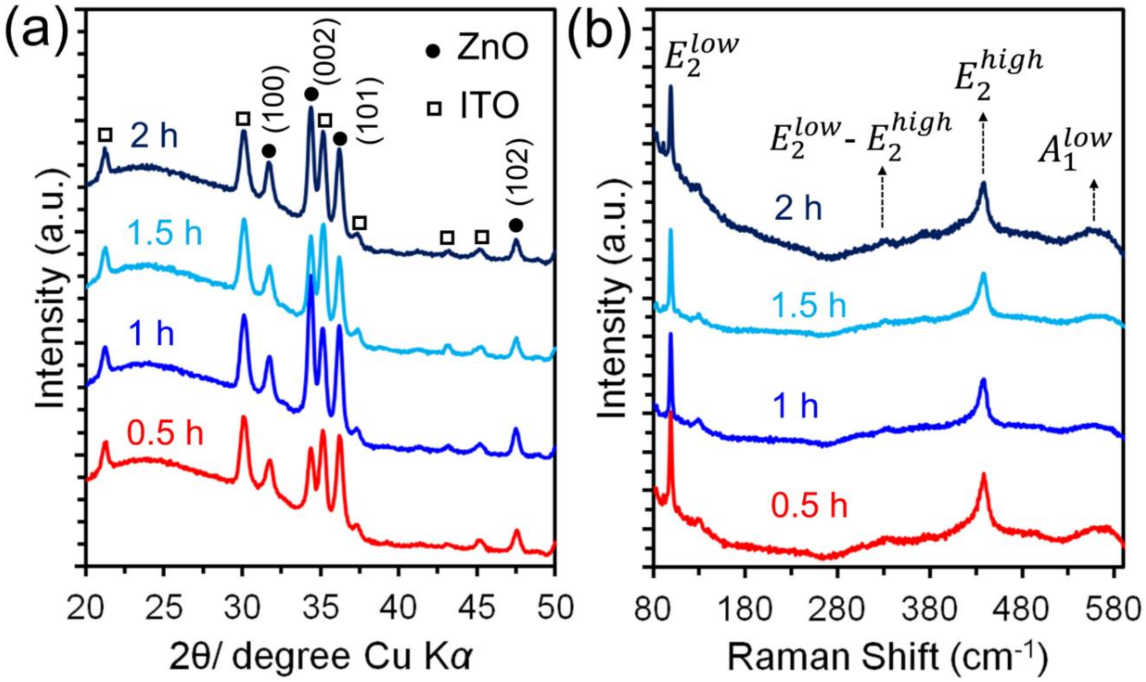

Figure 5.5 (a) XRD patterns and (b) Raman spectra of nanostructured ZnO films.

The crystal structure and phase composition of the synthesized nanostructured ZnO films were studied by XRD analyses. Figure 5.5(a) shows the XRD patterns of the samples after oxidation under different irradiation time. All the nanostructured ZnO films exhibited diffraction peaks at 2θ = 31.8°, 34.4°, 36.2°, and 47.5° which can be indexed to the (100), (002), (101) and (102) planes of hexagonal wurtzite ($P6_3mc$) crystal structure of ZnO, respectively[28]. The appearance of strong and sharp ZnO peaks suggests the highly crystalline nature of the as-prepared samples. No characteristic peaks related to Zn metal or other impurities were detected except from the ITO substrate, indicating the full conversion of Zn to ZnO and the high purity of the nanostructured ZnO films. The strong (002) plane reflection representing c-axis orientation is easily observed in all the films, along with weak reflections corresponding to (100) and (101) planes. It means that the NSs have more stacks of (002) crystal planes detected in comparison to that of (100) and (101) planes which are parallel to the *c*-axis, thus, the intensity from (002) planes was stronger than that of (100) and (101) planes. It is also relevant to note that all the ZnO NRs developed from the original H_2O oxidation process were relatively oriented perpendicular to the substrate. But here, interestingly, the 0.5 h-ZnO sample exhibits a higher (101) peak, which is in agreement with its morphology wherein the ZnO NRs are almost lying parallel to the substrate exposing their non-polar planes. Again, the presence of an electric field possibly has orientation effects on ZnO dipolar molecules[29]. In the preasent system, the initial ZnO nuclei acted as dipoles and grew parallel to the substrate as NRs under microwave irradiation. Then as the oxidation is progressed, the non-polar planes of these ZnO NRs are subsequently dissolved forming pointed NRs.

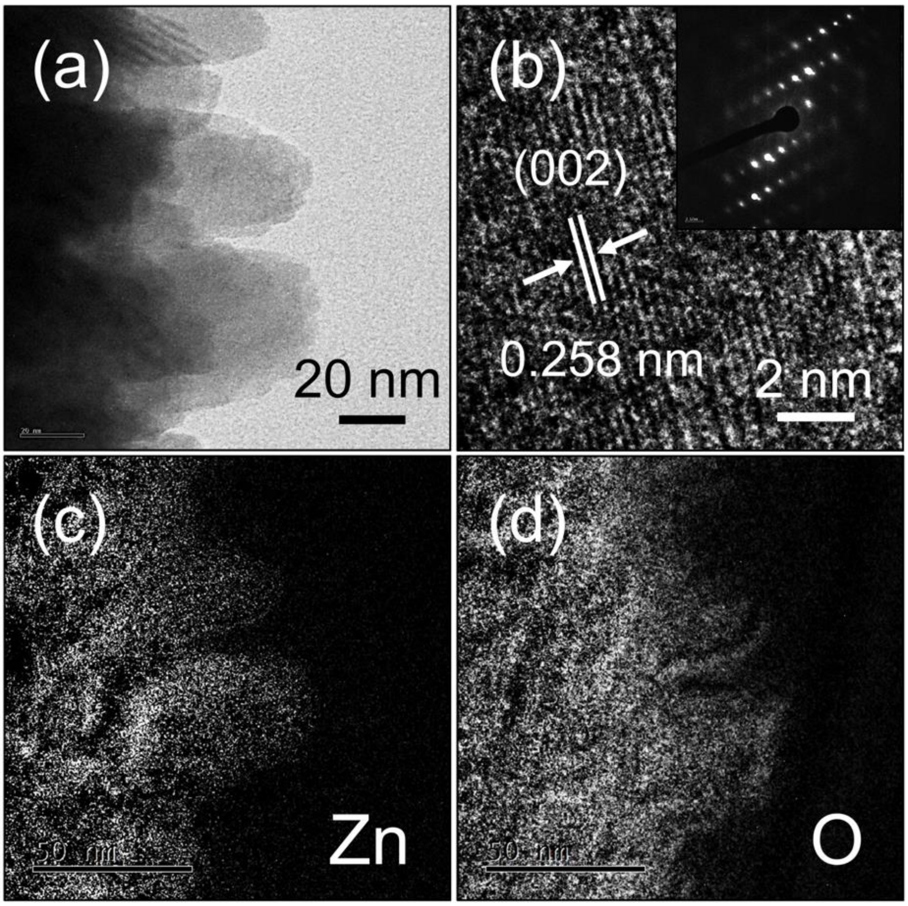

Figure 5.6 (a) TEM and (b) HRTEM images of 0.5 h-ZnO sample. Inset: NBD pattern. Images (c)-(d) are its corresponding EELS elemental mapping.

Figure 5.6(a) shows a typical TEM image of ZnO NRs formed after 30 min of microwave-assisted H_2O oxidation. The ZnO NRs have diameters of 40-50 nm and gradually narrowing near the top, which is consistent with their SEM image. The corresponding high-resolution TEM (HRTEM) image of an area near the tip of an individual ZnO NR is shown in Figure 5.6(b). The (002) lattice plane of hexagonal ZnO, with lattice spacing of ~ 0.26 nm, can be clearly measured in the lattice-resolved HRTEM image[30]. This denotes that the ZnO NRs preferentially grow along the [001] direction. Furthermore, these ZnO NRs possess high-quality single crystalline structure based on the nanobeam electron diffraction (NBD) pattern (inset) showing clear and sharp diffraction spots. The EELS elemental mapping images of Zn and O elements based on Figure 5.5(a), are shown in Figure 5.6(c) and 5.6(d), respectively. The mapping analysis validated the uniform distribution of Zn and O elements over the surface area of the NR.

Raman spectroscopy was also carried out to analyze the effect of irradiation time on the vibrational properties of the nanostructured ZnO films. Figure 5.5(b) shows the room temperature Raman spectra of all the samples under excitation of a 532 nm laser line. Dominant peaks at 99 cm^{-1} and 438 cm^{-1}, which are commonly detected in the wurtzite structure ZnO, are attributed to the E_2^{low} and E_2^{high} mode of non-polar optical phonons. It is well-known that the E_2^{low} mode in ZnO is related with the vibration of the heavy Zn sub-lattice and the E_2^{high} mode involves only the oxygen atoms[31]. Their strong intensities again signify the high-crystalline quality of the nanostructured ZnO films. The small peak at 331 cm^{-1} is designated to $E_2^{high} - E_2^{low}$ (multiphonon process) and is identified to be a second order vibration mode arising from zone-boundary phonons[32]. On the other hand, according to the group theory, the broad peak around 575 cm^{-1} can be assigned to the A_1^{low}, which originates from intrinsic defects including oxygen vacancies (V_O) and zinc interstitials (Zn_i)[33].

5.3.2 Surface Chemical State and Charge-Transporting Property for Solar Cells

The elemental composition and chemical state on the surface of the microwave-asssited H_2O-oxidized ZnO films were examined by XPS analyses, as illustrated in Figure 5.7. A low-resolution scan taken over a wide energy range is shown in Figure 5.6(a). Strong signals of Zn, O and a small peak of C were detected in all the survey spectra. The C 1s peak comes mostly from atmospheric contamination due to air exposure of the samples. The binding energies (BE) in all the spectra were calibrated by means of that C 1s (286.4 eV). Figure 5.7(b) shows the high resolution Zn 2p spectra. Doublet pair peaks of the Zn 2p core levels are observed at 1022 and 1044.2 eV and are typically assigned to the BE of Zn$2p_{3/2}$and Zn$2p_{1/2}$, respectively.

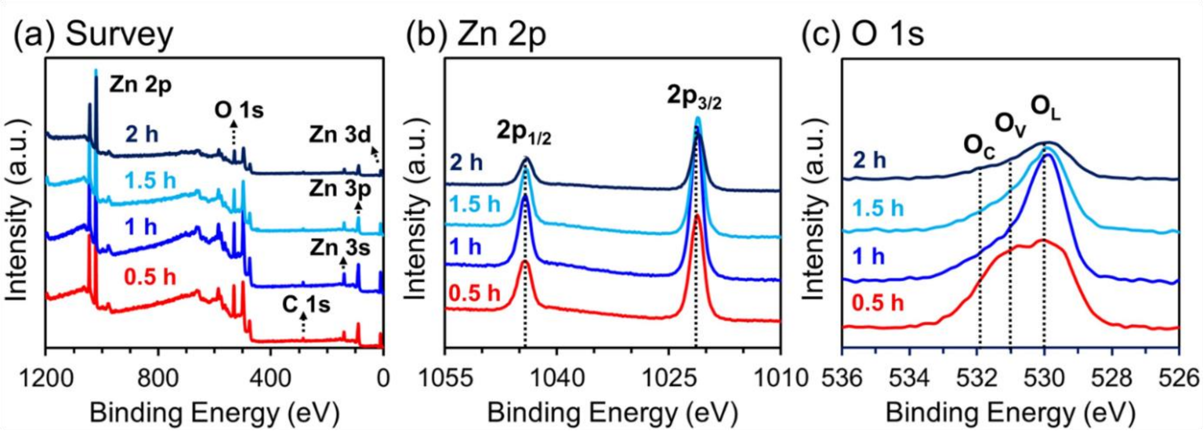

Figure 5.7 (a) XPS survey spectra and high-resolution XPS spectra of (b) Zn 2p and (c) O 1s of nanostructured ZnO films.

Their calculated BE difference or spin-orbital splitting is 23 eV, which proves the existence of Zn in oxidized states only (Zn^{2+}) [34]. Most importantly, the absence of metallic Zn peak at 1021.50 eV further confirms that the Zn thin films are completely oxidized even at a short time of 30 min of microwave irradiation. In addition, Figure 5.7(c) presents the high-resolution O1s spectra of the samples. It can be assumed that each O1s peak is composed by three components positioned at 530.3 eV, 531.0 eV and 531.9 eV, respectively. The O_L peak centered at low BE side (~530.3 eV) corresponds to O^{2-} ions on wurtzite ZnO crystal[35]. The medium BE O_V peak centered at 531.0 eV is normally assigned to O^{2-} in oxygen-deficient sites within the ZnO matrix, which could be related to the concentration of oxygen vacancies of nanostructured ZnO films[36]. The high BE O_H peak located at 531.9 eV can be ascribed to the presence of loosely bound oxygen on the surface of ZnO in the form of OH^{-}groups[37]. It is noticeable that the O_H and O_V peaks are stronger for the 0.5 h-ZnO sample suggesting that it has a higher amount of OH^{-} group and oxygen vacancies. Both peaks become negligible as irradiation time is increased indicating that 1-2 h-ZnO samples could work better as ETL for perovskite solar cells since perovskite films readily decompose in contact with hydroxyl group[38].

Finally, the electron extraction property of the nanostructured ZnO films was investigated using steady-state PL to evaluate their applicability in solar cell devices. Figure 5.8(a) shows the steady-state PL of $CH_3NH_3PbI_3$ films on top of glass/ITO and glass/ITO/nanostructured ZnO films. Evidently, the intrinsic fluorescence emission of $CH_3NH_3PbI_3$ at around 770 nm is quenched through contact with all the samples, demonstrating that electrons are successfully transported from the perovskite film. More importantly, the 0.5 h-ZnO/perovskite bilayer showed the weakest quenching possibly due to its significant amount of OH^{-} group, which was in agreement with the XPS analysis. Cheng et al. established that OH^{-} group intensified the decomposition of perovskite[38]. Here, the surface OH^- group of 0.5 h-ZnO sample possibly broke the ionic interaction between $\mathrm{CH_3NH_3^+}$ and $\mathrm{PbI_3^-}$ and subsequently destroyed the crystal structure of $\mathrm{CH_3NH_3PbI_3}$, as illustrated in the following reactions[38]:

$$\mathrm{OH^- + CH_3NH_3I \rightarrow CH_3NH_3OH + I^-} \quad (5)$$

$$\mathrm{CH_3NH_3OH \overset{\Delta}{\rightarrow} CH_3NH_2 \uparrow + H_2O \uparrow} \, (6)$$

$$\mathrm{CH_3NH_3I + PbI_2 \leftrightarrow CH_3NH_3PbI_3} \, (7)$$

Specifically, the breakdown of hydroxide to $\mathrm{CH_3NH_2}$ and $\mathrm{H_2O}$ during annealing (eqn. 2) further pushed the reaction (5) and at the same time favored the reverse reaction of eqn. (7), which is the decomposition of $CH_3NH_3PbI_3$. Moreover, the absorption spectrum of perovskite films on top of the nanostructured ZnO films is shown in Figure 5.8(b). As expected, the 2 h-ZnO/perovskite bilayer presented the highest light absorption due to higher surface area and surface roughness of the honeycomb structure.

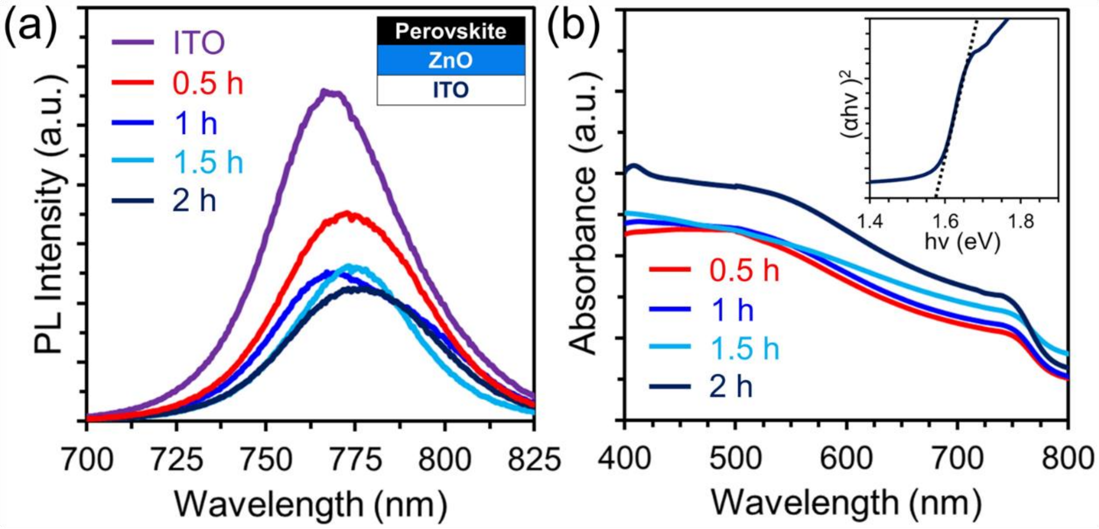

Figure 5.8 (a) Steady-state photoluminescence and (b) absorption spectra of perovskite films on top of nanostructured ZnO films.

5.4 Summary

This chapter introduced the growth of nanostructured ZnO from Zn thin films using only H_2O under microwave irradiation. This simple hybrid technique dramatically accelerated the formation of nanostructured ZnO films needing only 30 min of microwave-assisted H_2O oxidation compared with 8 h of conventional H_2O oxidation. Diverse morphologies including flat-topped NRs, pointed NRs and honeycomb-like structures composed of NTs were generated through increasing microwave irradiation time. The nanostructured ZnO films had wurtzite crystal structure with highly crystalline nature based on XRD, Raman, HRTEM, NBD analyses. The samples formed at longer irradiation times revealed negligible oxygen vacancies and OH^- group. The steady-state PL intensity of 2 h-ZnO/perovskite bilayer exhibited the strongest quenching effect demonstrating its capability for electron transport. On the other hand, the presence of significant amount of OH^- group proved to be detrimental for 0.5 h-ZnO since it showed the weakest quenching of perovskite PL emission. These initial results highlight the potential of microwave-assisted H_2O oxidation to fabricate high-quality nanostructured ZnO films for photovoltaic applications.

References

(1) C. M. Pelicano and H. Yanagi, *J. Mater. Chem. C*, 2017, **5**, 8059-8070

(2) T. Krishnakumar, R. Jayaprakash, N. Pinna, V. N. Singh, B. R. Mehta and A. R. Phani, *Mater. Lett.*, 2009, **63**, 242–245.

(3) J. S. Schanche, *Mol. Divers.*, 2003, **7**, 291–298.

(4) Q. C. Li, V. Kumar, Y. Li, H. T. Zhang, T. J. Marks and R. P. H. Chang, *Chem. Mater.*, 2005, **17**, 1001.

(5) Y. Shi, C. Zhu, L. Wang, C. Zhao, W. Li, K. K Fung, T. Ma, A. Hagfeldt and N. Wang, *Chem. Mater.*, 2013, **25**, 1000-1012.

(6) S. Balanand, M. J. Maria, T. P. D. Rajan, A. P Mohamed and S. Ananthakumar, *Chem. Eng. J.*, 2016, **284**, 657–667.

(7) K. Kombaiah, J. J. Vijaya, L. J. Kennedy and M. Bououdina, *Ceram. Int.*, 2016, **42**, 2741-2749.

(8) J. Tang, J. Chai, J. Huang, L. Deng, X. S. Nguyen, L. Sun, T. Venkatesan, Z. Shen, C. B. Tay and S. J. Chua, *ACS Appl. Mater. Interfaces*, 2015, **7**, 4737.

(9) R. Soleimanzadeh, M. S. S. Mousavi, A. Mehrfar, Z. K. Esfahani, M. Kolahdouz and K . Zhang, *J. Cryst. Growth*, 2015, **426**, 228-33.

(10) Y. Zhu and F. Chen, Chem. Rev., 2014, **114**, 6462–6555

(11) C. O. Kappe, D. Dallinger and S. S. Murphree, *Practical Microwave Synthesis for Organic Chemists*, Wiley-VCH: Weinheim, 2009.

(12) A. Pimentel, S. H. Ferreira, D. Nunes, T. Calmeiro, R. Martins, and E. Fortunato, *Materials*, 2016, **9**, 299.

(13) H. E. Unalan, P. Hiralal, N. Rupesinghe, S. Dalal, W. I. Milne, and G. A. Amaratunga, *Nanotechnology*, 2008, **19**, 255608.

(14) J. Hassan, M. Mahdi, C. Chin, H. Abu-Hassan, and Z. Hassan, *J. Alloys Compd.*, 2013, **546**, 107–111.

(15) P. Rai, S. G. Kim, and Y. T. Yu, *J. Mater. Sci.: Mater. Electron.*, 2012, **23**, 344–348.

(16) S. Boudjadar, S. Achour, N. Boukhenoufa, and L. Guerbous, *Int. J. Nanosci.*, 2010, **9**, 585–590.

(17) L. T. Guo, J. Wu, L. Z. Guo, Y. B. Zhu, C. Xu, and Y. H. Qiang, *J. Shanghai Jiaotong University (Sci.)*, 2012, **17**, 734–737.

(18) L. C. Nehru, V. Swaminathan, and C. Sanjeeviraja, *Powder Technol.*, 2012, **226**, 29–33.

(19) N. Assi, A. Mohammadi, Q. Sadr Manuchehri, and R. B. Walker, *Desalination Water Treat.*, 2015, **54**, 1939–1948.

(20) T. Krishnakumar, R. Jayaprakash, D. Sathya Raj, N. Pinna, V. N. Singh, A. R. Phani, and G. Neri, *J. Nanoparticle Res.*, 2011, **13**, 3327–3334.

(21) A. A. Chaaya, R. Viter, I. Baleviciute, M. Bechelany, A. Ramanavicius, Z. Gertnere, D. Erts, V. Smyntyna and P. Miele, *J. Phys. Chem. C*, 2014, 118, 3811–3819

(22) S. Cho, S.-H. Jung, K.-H. Lee, *J. Phys. Chem. C*, 2008, **112**, 12769–12776.

(23) R. Krishnapriya, S. Praneetha and A. V. Murugan, *CrystEngComm*, 2015, **17**, 8353-8367.

(24) Z. Xin, L. Li, X. Zhang and W. Zhang, *RSC Adv.*, 2018, **8**, 6027–6038.

(25) J. Lauritsen, S. Porsgaard, M. Rasmussen, M. Jensen, R. Bechstein, K. Meinander, B. Clausen, S. Helveg, R. Wahl, G. Kresse and F. Besenbacher, *ACS Nano*, 2011, **5**, 5987-5994.

(26) C. Shibata, T. Kashina and K. Ohuchi, *Jpn. J. App. Phys.*, 1996, **35**, 316.

(27) S. Bai, L. Wang, Z. Li and Y. Xiong, *Advanced Science*, 2017, **4**, 1600216.

(28) Sunaina, M. Sreekanth, S. Ghosh, S. K. Mehta, A. K. Ganguli and Menaka Jha, *CrystEngComm*, 2017, **19**, 2264-2270.

(29) S. Nomanbhay and M.Y. Ong, *Bioengineering*, 4 (2017), 57-78.

(30) J. Yu, X. Chen, Y. Wang, H. Zhou, M. Xue, Y. Xu, Z. Li, C. Ye, J. Zhang, P.A. Van Aken, P.D. Lund and H. Wang, *J. Mater. Chem. C*, 2016, **4**, 7302-7308.

(31) X. L. Xu, S. P. Lau, J. S. Chen, G. Y. Chen and B. K. Tay, *J. Cryst. Growth,* 2001, **223**, 201−205.

(32) S. Khachadorian, R. Gillen, S. Choi, C. Ton-That, A. Kliem, J. Maultzsch, M.R. Phillips and A. Hoffmann, *Phys. Status Solidi (b)*, 2015, **252**, 2620-2625.

(33) L. Shen, N. Bao, K. Yanagisawa, K. Domen, A. Gupta and C. A. Grimes, *Nanotechnology,* 2006, **17**, 5117– 5123**.**

(34) B. Panigrahy, M. Aslam and D. Bahadur, *J. Phys. Chem. C*, 2010, 114, 11758−11763.

(35) M. Chen, X. Wang, Y. H. Yu, Z. L. Pei, X. D. Bai, C. Sun, R. F. Huang and L. S. Wen, *Appl. Surf. Sci.*, 2000, **158**, 134−140.

(36) R. N. Aljawfi and S. Mollah, *J. Magn. Magn. Mater.*, 2011, **323**, 3126−3132.

(37) J. C. C. Fan and J. B Goodenough, *J. Appl. Phys.*, 1977, **48**, 3524.

(38) Y. Cheng, Q.-D. Yang, J. Xiao, Q. Xue, H.-W. Li, Z. Guan, H.-L. Yip and S.-W. Tsang, *ACS Appl. Mater. Interfaces*, 2015, **7**, 19986.

Chapter 6

Conclusions

6.1 Conclusions

This dissertation focused on providing viable alternative ETL materials for PSCs. The synthesized NSs were comprehensively characterized to correlate their resulting properties and their capability as ETL. The main results of this research are herein summarized.

Chapter 2 presented the synthesis of ZnO NRs via electrochemical deposition in a chloride medium. Longer NRs can be formed at extended deposition time. These NRs have shown excellent structural and optical properties, which are beneficial for solar cells. Furthermore, the effect of rubrene layer on the performance of PSCS was investigated. The rubrene interlayer served as a passivation layer and infiltrated the grain boundaries of the perovskite layer. A device based on 10 min-ZnO sample and rubrene:P3HT achieved a PCE_{max} of 3.9% and PCE_{ave} of 3.6%. These values increased further (PCE_{max} of 4.9% and PCE_{ave} of 3.8%) by utilizing longer NRs formed after 20 min of deposition. By employing longer ZnO NRs as ETL, better electronic contact and reduced charge carrier path length could be realized. Likewise, the devices with rubrene interlayer presented weaker hysteresis behavior in comparison to the device with P3HT as the only HTL.

In Chapter 3, a novel route of synthesizing ZnO NSs from Zn thin films by just using pure H_2O is described. This technique eliminated the need for any growth directing agents and complex fabrication processes. Diverse surface architectures were produced by controlling the oxidation time and temperature. The highest *PCE* of 5.96% and average *PCE* of 5.46% was observed for a device based on pointed ZnO NRs, which were generated at 90 °C for 8 h of H_2O oxidation. As discussed in the previous chapter, the formation of rod-like structures led to superior interfacial area between the ETL and the active layer. Subsequently, suppressed charge recombination and improved photovoltaic performance could be expected. Furthermore, the pH-controlled H_2O oxidation was demonstrated to develop nanostructured ZnO films as ETLs for Bi-based Pb-free PSCs. This is the first study to use nanostructured ZnO as ETL for Pb-free PSCs. Different pH conditions initiated the growth of unique morphologies including particles, rods and tubes. It was also found out that the perovskite film formation depended on the morphology of the underlying ZnO films. A competitive PCE_{max} of 0.083% was achieved using ZnO NPs obtained in an acidic H_2O. Most importantly, the best performing device has shown good stability in ambient conditions for 4 weeks, which is difficult to accomplish for Pb-based PSCs.

In chapter 4, a one-step $AlCl_3$ treatment of H_2O-oxidzed ZnO NRs converted them into Al-doped ZnO NTs with superior charge-transport properties. Such process is the first to simultaneously etch and dope NSs. The (001) polar planes of ZnO NRs reacted with the acidic $AlCl_3$ resulting in the formation of NTs. The successful substitution of Zn^{2+} ions by Al^{3+} ions in the ZnO lattice was established by XRD, Raman, XPS, and EELS elemental mapping analyses. The doped films exhibited higher band gap values, which could be explained by Moss- Burstein effect). The AZO samples revealed higher electrical conductivity and electron mobility values due to the substantial increase in the concentration of charge carriers after the doping process. Consequently, the doped samples quenched the perovskite emission stronger than the original ZnO NRs signifying faster electron extraction.

Chapter 5 introduced the accelerated growth of H_2O-oxidized ZnO films under microwave irradiation. The formation of nanostructured ZnO films was expedited due to the increase in probability of collisions between molecules which subsequently reduced the activation energy to form ZnO nuclei. ZnO NRs could be formed after 30 min of microwave-assisted H_2O oxidation compared with 8 h of conventional H_2O oxidation. The duration of irradiation time dictated the amount of OH^- group on the surface of the ZnO films. Insignificant amount of oxygen vacancies and OH^- group were found for the films obtained at longer irradiation time. Thus, the 2 h-ZnO sample showed the most promising electron-transporting capability based on steady-state PL analysis.

Finally, H_2O-oxidized ZnO-based PSCs showed higher device performance compared with their electrodeposited-based counterparts having the same ZnO thickness and device configuration. The optimized conditions for H_2O oxidation was found to be at a temperature of 90 °C and oxidation time of 8 h to produce pointed ZnO NRs with larger surface area and ideal thickness for PSCs (PCE_{max} = 6%). I believe that through interfacial engineering, improvement of fabrication conditions, optimization of H_2O oxidation parameters, as well as the use of better HTL and electrodes, much higher efficiencies can be achieved. These preliminary results on the applicability of our nanostructured ZnO films reveal that their potential as ETL is not limited to PSCs alone but can be extended to other photovoltaic and optoelectronic devices as well.

6.2 Suggestions for Future Work

6.2.1 One-step Formation of H_2O-Oxidized Doped-ZnO Films

As reported in Chapter 3, the doping of H_2O-oxidized ZnO NRs involved two steps: (1) the formation of the NRs; and (2) $AlCl_3$ treatment. It would be more beneficial and efficient if doping and NS structure formation are performed simultaneously in a one-step process. For example, the dopant metal can be deposited on top of Zn thin film before H_2O oxidation. However, the dopant metal should be easily oxidized by H_2O such as Al, Mg, Mn and Ca. The deposition of dopant metal could also affect the resulting morphologies after oxidation.

6.2.2 Effect of Different Growth Directing Reagents

Most of the experiments done for this research only involved H_2O as the main solvent. Since the surface architecture of ZnO crystal is very sensitive to other species in the solution, it is interesting to see what will be the effect of the addition of different growth directing agents such as Zn salts, dissolved O_2, other bases and NaCl on the resulting properties of ZnO films.

Appendix

Table 1. Calculated X-ray diffraction parameters of ZnO from International Crystal Structure Database (ICSD, 01-079-0208).

2θ	**d-spacing (Å)**	**I**	**(hkl)**
31.62	2.827	57.6	(100)
34.34	2.61	41.5	(002)
36.1	2.486	100	(101)
47.37	1.918	20.4	(102)
56.31	1.632	27.9	(110)
62.65	1.482	22.9	(103)
66.03	1.414	3.5	(200)
67.64	1.384	19	(112)
68.74	1.365	9.3	(201)
72.36	1.305	1.4	(004)
76.59	1.243	2.8	(202)
81.11	1.185	1.3	(104)
89.19	1.097	5	(203)

2θ (°)	d-spacing (Å)	I	(hkl)
13.95	6.342	60	(002)
14.22	6.222	100	(11)
19.97	4.441	7	(112)
20.16	4.400	11	(200)
23.65	3.759	27	(211)
24.60	3.615	17	(202)
28.11	3.171	45	(004)
28.67	3.111	66	(220)
31.02	2.881	14	(213)
31.64	2.826	33	(114)
32.01	2.793	21	(222)
32.14	2.783	49	(310)
34.84	2.573	5	(204)
35.19	2.548	12	(312)
37.49	2.397	4	(321)
40.59	2.221	50	(224)
40.99	2.200	18	(400)
42.35	2.132	6	(215)
42.73	2.114	4	(006)
42.93	2.105	15	(411)
43.21	2.092	45	(314)
43.50	2.079	5	(402)
46.09	1.968	8	(420)
47.69	1.808	11	(413)
50.44	1.759	19	(4 0 4)
52.27	1.743	6	(2 2 6)
52.44	1.736	4	(4 3 1)
52.69	1.726	3	(3 3 4)
53.02	1.683	6	(5 1 0)
54.46	1.672	3	(3 1 6)

54.86	1.646	10	(4 2 4)
56.28	1.624	7	(4 1 5)
56.60	1.585	3	(4 3 3)
58.13	1.555	5	(0 0 8)
59.36	1.536	4	(4 4 0)

Table 2. Calculated X-ray diffraction parameters of tetragonal $CH_3NH_3PbI_3$.*

*Reference: Takeo Oku (October 22nd 2015). Crystal Structures of $CH_3NH_3PbI_3$ and Related Perovskite Compounds Used for Solar Cells, Solar Cells - New Approaches and Reviews, Leonid A. Kosyachenko, IntechOpen, DOI: 10.5772/59284.

Research Achievements

List of Publications

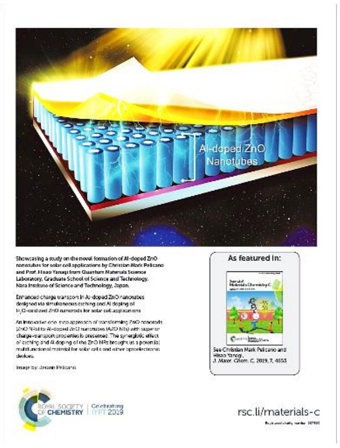

1. **<u>C. M. Pelicano</u>**, H. Yanagi,

Enhanced charge transport in Al-doped ZnO nanotubes designed via simultaneous etching and Al doping of H_2O-oxidized ZnO nanorods for solar cell applications, ***J. Mater. Chem. C***, 2019, 7, 4653-4661. **(Inside Back Cover)**

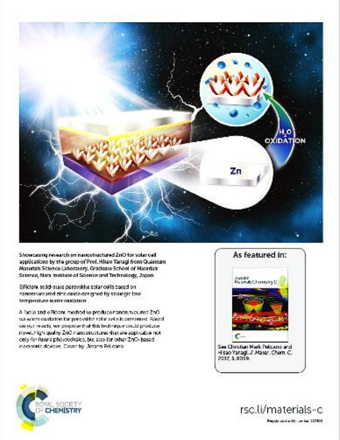

2. **<u>C. M. Pelicano</u>**, H. Yanagi,

Efficient solid-state perovskite solar cells based on nanostructured zinc oxide designed by strategic low temperature water oxidation,

J. Mater. Chem. C, 2017, 5, 8059-8070. **(Back Cover)**

3. **<u>C. M. Pelicano</u>**, H. Yanagi, Effect of rubrene: P3HT bilayer on perovskite solar cells with electrodeposited ZnO nanorods, ***J. Energy Chem***., 2018, 27, 455-462.

4. **<u>C. M. Pelicano</u>**, H. Yanagi, pH-controlled surface engineering of nanostructured ZnO films generated via a sustainable low-temperature H_2O oxidation process, ***Appl. Surf. Sci.***, 2019, 467–468, 932-939.

5. **<u>C. M. Pelicano</u>**, H. Yanagi, Accelerated Growth of Nanostructured ZnO Films via Low Temperature Microwave-assisted H_2O Oxidation for Solar Cell Applications, ***(submitted)***

Related Publications

1. V. J. Garcia, **C. M. Pelicano**, H. Yanagi, Low temperature-processed ZnO nanorods-TiO_2 nanoparticles composite as electron transporting layer for perovskite solar cells, ***Thin Solid Films***, 2018, 662, 70-75.

2. M.D. Balela, **C.M. Pelicano**, J.D. Ty, H. Yanagi, Formation of zinc oxide nanostructures by wet oxidation of vacuum deposited Zn thin film, ***Opt. Quant. Electron***, 2017, 49, 3.

3. **C. M. Pelicano**, P. R. Regonia, R. Tani, A. Ishizumi, K. Ikeda, and H. Yanagi, Predicting optical band gap of ZnO quantum dots using supervised machine learning, (submitted)

4. **C. M. Pelicano**, I. Raifuku, Y. Ishikawa, Y. Uraoka and H. Yanagi, Interfacial modification of H_2O-oxidized ZnO nanorods by Mg-doped ZnO nanoparticles for solar cell applications", (manuscript in preparation)

Research Grants and Awards

1. Nara Institute of Science and Technology Foundation Research Grant (1 Million ¥), "Fabrication of Nanostructured ZnO for Perovskite Solar Cells and Light Emitting Diodes", April 1, 2018-March 30, 2019.

2. Marubun Research Promotion Foundation (100K ¥), International Exchange Grant, 3rd Advanced Energy Materials Conference, University of Surrey, England, UK, September 2017.

3. Invitation to the Research Proposal for Grant-in-Aid for PhD Students in Nara Institute of Science and Technology (175K ¥), "Fabrication of Nanostructured ZnO for Perovskite Solar Cells and Light Emitting Diodes".

4. Best Oral Presentation Award, 1st International Conference on Materials Science and Engineering in the Philippines, Tagaytay, Philippines, October 2018.

International Conferences

1. **C. M. Pelicano**, H. Yanagi, Nanostructured Zinc Oxide Films Grown via Microwave-Assisted H2O Oxidation for Perovskite Solar Cells, International Conference on Materials Engineering and Nano Sciences, Hiroshima, Japan, March 2019. (Oral Presentation)

2. **C. M. Pelicano**, H. Yanagi, Enhanced Charge Transport of Al-doped ZnO Nanotubes Generated via $AlCl_3$ Etching and Synchronous Doping of H_2O-oxidized ZnO Nanorods for Perovskite Solar Cell Application, 1st International Conference on Materials Science and Engineering in the Philippines, Tagaytay, Philippines, October 2018. (Oral Presentation)

3. **C. M. Pelicano**, H. Yanagi, Surface Engineering of Nanostructured ZnO Films via pH-Controlled Low Temperature Water Oxidation, 10th International Conference on Nanomaterials (NANOCON), Brno, Czech Republic, September 2018. (Oral Presentation)

4. **C. M. Pelicano**, H. Yanagi, Al-doped ZnO Nanotubes Designed via Simultaneous Doping and Etching of H_2O-oxidized ZnO Nanorods for Perovskite Solar Cells, First International Conference on 4D Materials and Systems, Yonezawa, Japan, August 2018. (Oral Presentation)

5. **C. M. Pelicano**, H. Yanagi, Nanostructured Zinc Oxide Formed by Low Temperature H_2O Oxidation for Efficient Perovskite Solar Cells, 2017 GIST-NAIST-NCTU Joint Symposium on Advanced Materials, South Korea, November 2017. (Oral Presentation)

6. **C. M. Pelicano**, H. Yanagi, Interfacial Modification of ZnO Nanorods by Mg-doped ZnO Nanoparticles for Efficient Perovskite Solar Cells, 2nd Advanced Energy Materials Conference, University of Surrey, England, United Kingdom, September 2017. (Oral Presentation)

7. **C. M. Pelicano**, H. Yanagi, ZnO Nanorods-Based Perovskite Solar Cells with Rubrene:P3HT as Hole Transporting Layers, 9th International Conference on Molecular Electronics and Bioelectronics, Kanazawa, Japan, July 2017. (Poster Presentation)

8. **C. M. Pelicano**, J. Damasco Ty, H. Yanagi, Low Temperature Growth of Nanostructured ZnO in Water for Perovskite Solar Cells, 12th International Conference on Nano-Molecular Electronics, Kobe, Japan, December 2016. (Poster Presentation)

Domestic Conferences

1. **C. M. Pelicano**, H. Yanagi, Accelerated Growth of Nanostructured Zinc Oxide Films via Microwave-Assisted H_2O Oxidation for Solar Cell Applications, The 80th JSAP Autumn Meeting 2019, Hokkaido University, Japan, September, 2019. (Poster Presentation)

2. **C. M. Pelicano**, H. Yanagi, Microwave-Assisted H_2O Oxidation-Derived Nanostructured Zinc Oxide Films as Electron-Transporting Layer for Solar Cells, The 66th JSAP Spring Meeting 2019, Tokyo Institute of Science and Technology, Japan, March 2019. (Poster Presentaion)

3. **C. M. Pelicano**, H. Yanagi, Formation of Al-Doped ZnO Nanotubes via Simultaneous Etching and Doping of H2O-oxidized ZnO Nanorods for Perovskite Solar Cells, The 79th JSAP Autumn Meeting 2018, Nagoya, Japan, September 2018. (Oral Presentation)

4. **C. M. Pelicano**, H. Yanagi, Effect of Mg-doped ZnO nanoparticles on H2O-oxidized ZnO nanorods-based perovskite solar cells, The 78th JSAP Autumn Meeting 2017, Fukuoka, Japan, September 2017. (Oral Presentation)

5. C. M. Pelicano, H. Yanagi, Low temperature processed ZnO nanorods for perovskite solar cells, The 64th JSAP Spring Meeting 2017, Yokohama, Japan, March 2017. (Oral Presentation)

Related Presentations

1. V. Garcia, **C. M. Pelicano**, H. Yanagi, Low Temperature-Processed ZnO Nanorods-TiO_2 Nanoparticles Composite as Electron Transporting Layer for Perovskite Solar Cells, International Symposium of the Vacuum Society of the Philippines, University of the Philippines Diliman, January 2018. (Oral Presentation)

2. P. R. Regonia, **C. M. Pelicano**, R. Tani, A. Ishizumi, K. Ikeda, and H. Yanagi, Predicting Optical Band Gap of ZnO Quantum Dots using Supervised Machine Learning, The 7th International Symposium on Organic and Inorganic Electronic Materials and Related Nanotechnologies, Nagano, Japan, June 2019. (Oral Presentation)

Acknowledgements

I would like to express my deepest gratitude to the individuals who helped me in this endeavor:

To the Lord Almighty, for providing me this break, and granting me the wisdom, patience and understanding I needed the most to proceed successfully. I praise the Lord for giving me strength at times when I am facing a lot of hardships throughout this doctoral course.

To Prof. Hisao Yanagi, my main supervisor, for allowing me to work on this interesting topic. I am very thankful for all the time, guidance, patience and unending support you have given me. Again, I would like to express my deepest gratitude for this life-changing opportunity.

To the members of my advisory panel, Prof. Takayuki Yanagida, Assoc. Prof. Ken Hattori, and Assoc. Prof. Hiroyuki Katsuki, for their valuable suggestions and discussions that significantly improved my thesis.

To the technical staff of Materials Science Division, Mr. Kazuhiro Miyake, Mr. Masahiro Fujihara, Mr. Shohei Katao, Ms. Tomoko Ohno and Mr. Yasuo Okajima for the technical assistance and advices.

To all the professors and members of Quantum Materials Science Laboratory for all the memories, discussions and experiments. Thank you very much for always helping and taking care of me. You definitely made my stay in the lab worthwhile.

To Prof. Andrei Vescan and Dr. Holger Kalisch of Compound Semiconductor Technology, RWTH Aachen University, for giving me the opportunity to work on their laboratory for my internship. Thank you for the helpful discussions about Pb-free perovskite solar cells.

To my fellow Filipinos here at NAIST for all the fun memories, adventures, and celebrations that we shared. Thank you very much for the support and encouragement.

And finally, to my parents, siblings, and to Jenichi, for the love, understanding, trust and unending support. You have been my inspiration in overcoming every struggle that had come my way.